Master's thesis

NTNU
Norwegian University of Science and Technology
Faculty of Information Technology and Electrical Engineering
Department of Engineering Cybernetics

Sif Högnadóttir

Inner-Loop Adaptive Control of Fixed-Wing Unmanned Aerial Vehicles in Icing Conditions

Master's thesis in Cybernetics and Robotics
Supervisor: Kristoffer Gryte
Co-supervisor: Tor Arne Johansen, Richard Hann
June 2022

NTNU
Norwegian University of Science and Technology

Sif Högnadóttir

Inner-Loop Adaptive Control of Fixed-Wing Unmanned Aerial Vehicles in Icing Conditions

Master's thesis in Cybernetics and Robotics
Supervisor: Kristoffer Gryte
Co-supervisor: Tor Arne Johansen, Richard Hann
June 2022

Norwegian University of Science and Technology
Faculty of Information Technology and Electrical Engineering
Department of Engineering Cybernetics

NTNU
Norwegian University of
Science and Technology

Abstract

Motivated by the ever-increasing use of small unmanned aerial vehicles (UAVs), this thesis compares a model reference adaptive controller (MRAC) with PID controllers. Both are developed for the Skywalker X8 fixed-wing UAV operating in icing conditions, encompassing asymmetric icing on the wings and reduced control effectiveness. The MRAC scheme is given by a linear model with a bias term to capture unmodeled effects and modified with the projection operator to increase robustness.

The controllers' performance is tested under several conditions and the results show that the MRAC control scheme handles a reduction in airspeed better, whereas the PID controller proved less affected by wind gust disturbances. Overall, both controllers exhibit the most difficulty when the icing level is severely asymmetric. This is also the case when given a path following case, executed with an icing sequence with asymmetry and a steady wind component with wind gust disturbances. The findings in this thesis show that the MRAC control scheme and the PID controller demonstrate similar qualities with respect to tracking performance.

Computational fluid dynamics analysis allowed for a simulation exploring the reduced control surface effectiveness due to icing. The results show that the MRAC controller is less affected by the reduction in control surface efficiency than the PID control scheme with a square reference angle in roll, while the opposite is true with a square reference angle in pitch.

Examining the bias and integral terms of the adaptive controller and PID controller, respectively, shows that the bias terms and to some degree the roll integral term can detect icing. The MRAC control scheme is of greater complexity, however it provides the future exploration of system identification with the potential of icing level estimation.

Sammendrag

Norwegian translation of the abstract
Motivert av økende bruk av små ubemannede luftfartøy utforsker denne oppgaven bruken av MRAC (*model reference adaptive control*), en type adaptiv regulator, og sammenligner det mot konvensjonelle PID-regulatorer. Begge regulatorene ble utviklet for bruk av det ubemannede luftfartøyet Skywalker X8 under værforhold med isning, det inkluderer asymmetrisk ising på vingene og redusert effektivitet i styreflatene som følge av ising. MRAC-regulatoren er gitt ved en lineær modell med biasledd for å fange opp effekten av umodellert dynamikk, og adapsjonsloven benytter projeksjon for økt robusthet.

Ytelsen til regulatorene er testet under ulike forhold, og resultatene viser at MRAC-regulatoren håndterer en reduksjon i lufthastighet bedre, mens PID-regulatoren er mindre påvirket av vindforstyrrelser. Begge regulatorene har dårligst ytelse når isningsnivået er svært asymmetrisk. Dette er også tilfellet under baneføling med asymmetrisk ising og vindforhold hvor vinden består av et konstant vindbidrag med stokastiske vindkast. I resultatene demonstrerer MRAC-regulatoren og PID-regulatoren lignende egenskaper til å følge tidsvarierende referanser.

Numerisk fluiddynamikk muliggjorde simuleringer som utforsket hvordan styreflatenes effektivitet påvirkes av nivået av isning. Resultatene viser at MRAC-regulatoren er mindre påvirket av redusert effektivitet i styreflatene for rull-referanser enn PID-regulatoren, mens det motsatte er tilfellet for stamp-referanser.

Ved å undersøke biasleddene for MRAC-regulatoren finner resultatene at disse reflekterer isningsnivået på luftfartøyet dersom adapsjonsraten for disse settes lavt nok. Integral-leddet i PID-regulatoren for rull klarer til en viss grad å fange opp den samme effekten. MRAC-regulatoren er mer kompleks enn PID-regulatoren, men gir muligheten for videre forskning med systemidentifikasjon og potensialet for isningsdeteksjon.

Preface

This thesis completes my degree in Cybernetics and Robotics at the Norwegian University of Science and Technology (NTNU). The work done in this thesis is a continuation of the work in my pre-project, which is reflected in the introduction of this thesis as the motivation and background for both reports are the same.

The work presented in this thesis was carried out at the Department of Engineering Cybernetics at NTNU. I would like to thank my supervisor Kristoffer Gryte for his support and guidance over the past year. Thank you for challenging me to submit a paper of my findings to the AIAA SciTech Forum. The paper is found in appendix C of the thesis. I would also like to thank my co-supervisor, Tor Arne Johansen, for his valuable insights into adaptive control theory which helped ensure progress in my work. A special thank goes to Richard Hann for performing computational fluid dynamics analysis to find an estimate of the control surface effectiveness in icing conditions to aid and support the work in this thesis.

My years in Trondheim would not be the same without my dearest friends. Thank you for all the fun adventures. Anne Joo and Kristine especially, thank you for all the fun times - those being at the helicopter lab, out to dinner, or simply making some waffles and knitting.

Finally, I would like to express my deepest gratitude to Daniel for his unconditional support and for always believing in me. I am truly lucky to have you in my life.

Contents

Part I

Introduction and Background Material

Chapter 1

Introduction

The areas of application for unmanned aerial vehicles (UAVs) continue to increase as supporting technology develops and costs are reduced. A selection of applications includes aerial surveying and mapping, search-and-rescue operations, package and food delivery, as well as research and education. In general, many of the vehicles' tasks relieve the human of performing dull tasks or going to dangerous and hard-to-reach places.

To broaden the scope of admissible operations for the UAV, research is going into how the UAVs can handle different meteorological conditions. One of these conditions is flight in atmospheric icing conditions which is the topic for this thesis.

Icing is a debilitating factor for a UAV as it increases drag, reduces lift, and increases the risk of stalling [1]. These factors elicit the need for increased control efforts to maintain flight. Additionally, ice accretion or run-back icing on the wing surface ahead of control surfaces results in reduced control surface effectiveness [2]. Smaller aircraft in particular, such as UAVs, are more sensitive to icing conditions compared to larger manned aircraft [3]. One way to handle icing conditions is by using ice protection systems [4], consisting of *anti-icing* to prevent ice accretion, or *de-icing* to remove already formed ice. These systems necessitate an increase in power consumption and preferably knowledge of the icing level to optimize the ice removal and its energy consumption. The problem of automatic icing detection is still a research question. This is of more concern for UAVs than larger manned aircraft as UAVs must rely entirely on onboard sensors and instruments to detect icing, whereas larger manned aircraft have a pilot onboard that can identify icing conditions [5].

One approach is to combine the use of de-icing systems and controllers that can cope with the adverse effects of icing, thereby increasing the de-icing intervals

and potentially reducing the associated energy consumption. Previous work has been done by Kleiven [6] with the development of robust controllers in icing conditions for the fixed-wing Skywalker X8 UAV. In this thesis, an adaptive control approach is explored for the Skywalker X8.

Adaptive control is a control scheme where the control law changes as an adaptive law attempts to estimate the parameters that characterize the system [7]. In this thesis, an inner loop model reference adaptive control (MRAC) scheme is developed. Model reference adaptive control is based on finding a feedback controller, such that the system output tracks a commanded reference, in the presence of unknown plant parameters [8, 9]. The concept of model reference adaptive control was first presented by Whitaker in 1958 [10]. A few years later, the stability proof using Lyapunov theory was given in 1965 and 1966 by Butchart and Shackloth [11], and by Parks [12], respectively. Similar research to the MRAC scheme in this thesis has been performed to test MRAC schemes on UAVs in [9, 13]. In [13] Chowdhary *et al.* present an MRAC scheme for a fixed-wing UAV that has been subject to asymmetric structural damage. This motivates the development of an MRAC controller for operation in asymmetric icing conditions.

The controllers in this thesis are tested in a simulation model in MATLAB/Simulink, where the model is based on the model data from the work of Winter [14], with the extension to an asymmetric model from Kleiven [6]. The aerodynamic coefficient data from [14] are given for iced and clean (no icing) airfoils. The icing data in [14] are found for the mixed icing case, being the most severe icing type of the three types – glaze, rime, and mixed – in terms of aerodynamic performance. Since the aerodynamic coefficients are based on symmetric icing levels, there are some uncertainties in the model when extending it to an asymmetric icing model. However, it is assumed to provide an adequate reflection of the behavior of the UAV with respect to the control aspect and the dynamics of ice accretion and shedding [6]. As such, the model is assumed to be valid for this thesis. Ice accretion on the propellers can have significant consequences on thrust generation [15]. However, ice accretion on the propellers is not considered in this thesis.

This thesis aims to answer the question of whether an adaptive solution is better suited to tackle the problem of controlling UAVs in icing conditions than a more conventional PID controller. Additionally, the thesis aims to explore whether one could infer any valuable knowledge about the icing conditions.

1.1 Organization

The thesis is divided into three parts;

- The first part gives an introduction to the subject and presents the necessary background material, including the UAV model, the aerodynamics, inner and outer loop controllers, and environmental factors, in chapters 1 and 2.
- The second part describes the final controllers, the simulator with its limitations, the simulation cases, and performance metric in chapters 3, 4, and 5.
- The third part presents and discusses the results in chapters 6 and 7, with concluding remarks given in chapter 8.

Chapter 2

Background Theory

In this chapter, the necessary background theory for the work in this thesis is presented. This includes the modelling of the UAV, model reference adaptive control (MRAC), PID control of a UAV, guidance laws and the environmental factors wind and icing. It is assumed that the reader has some prior knowledge of control theory.

2.1 UAV model

A traditional manned aircraft is equipped with structures that generate aerodynamic lift, control effectors and some form of internal space for carrying payloads [16]. Additionally, most aircraft are also equipped with propulsion systems. Unmanned aerial vehicles (UAVs) consist of the same components - typically in a smaller capacity.

In this section, the kinematics and dynamics, control surfaces, and the forces and moments that make up the mathematical model of an aircraft are presented. The following is based on the explanations of Beard & McLain [17] and Stengel [16].

2.1.1 Kinematics and Dynamics

The kinematics of a rigid body defines the relations between positions and velocities, whereas the dynamics define the relations between forces and moments and the momentum [17]. From Beard & McLain [17], the translational

kinematics of an aircraft are given as

$$\begin{bmatrix} \dot{p}_n \\ \dot{p}_e \\ \dot{p}_d \end{bmatrix} = \begin{bmatrix} \mathrm{c}_\theta \mathrm{c}_\psi & \mathrm{s}_\phi \mathrm{s}_\theta \mathrm{s}_\psi - \mathrm{c}_\phi \mathrm{s}_\psi & \mathrm{c}_\phi \mathrm{s}_\theta \mathrm{c}_\psi + \mathrm{s}_\phi \mathrm{s}_\psi \\ \mathrm{c}_\theta \mathrm{s}_\psi & \mathrm{s}_\phi \mathrm{s}_\theta \mathrm{s}_\psi + \mathrm{c}_\phi \mathrm{c}_\psi & \mathrm{c}_\phi \mathrm{s}_\theta \mathrm{s}_\psi - \mathrm{s}_\phi \mathrm{c}_\psi \\ -\mathrm{s}_\theta & \mathrm{s}_\phi \mathrm{c}_\theta & \mathrm{c}_\phi \mathrm{c}_\theta \end{bmatrix} \begin{bmatrix} u \\ v \\ w \end{bmatrix}, \tag{2.1}$$

where $\mathrm{c}_* = \cos * $ and $\mathrm{s}_* = \sin *$, the angles ϕ, θ and ψ are the roll, pitch and yaw angle, respectively, and u, v and w are the velocities along the x, y and z body axes, respectively.

The rotational kinematics are given as

$$\begin{bmatrix} \dot{\phi} \\ \dot{\theta} \\ \dot{\psi} \end{bmatrix} = \begin{bmatrix} 1 & \sin\phi \tan\theta & \cos\phi \tan\theta \\ 0 & \cos\phi & -\sin\phi \\ 0 & \sin\phi \ \sec\theta & \cos\phi \ \sec\theta \end{bmatrix} \begin{bmatrix} p \\ q \\ r \end{bmatrix}, \tag{2.2}$$

where p, q and r are the roll, pitch, and yaw angular rates, respectively.

The translational and rotational dynamics of the UAV are governed by Newton's second law of motion applied to the translational and rotational motion of the aircraft in equations (2.1) and (2.2) [17].

The translational dynamics are given as

$$\begin{bmatrix} \dot{u} \\ \dot{v} \\ \dot{w} \end{bmatrix} = \begin{bmatrix} rv - qw \\ pw - ru \\ qu - pv \end{bmatrix} + \frac{1}{\mathrm{m}} \begin{bmatrix} f_x \\ f_y \\ f_z \end{bmatrix}, \tag{2.3}$$

where m is the mass of the aircraft, and f_x, f_y and f_z are the external forces acting on the UAV in the body frame, b.

The rotational dynamics are given as

$$\begin{bmatrix} \dot{p} \\ \dot{q} \\ \dot{r} \end{bmatrix} = \begin{bmatrix} \Gamma_1 pq - \Gamma_2 qr \\ \Gamma_5 pr - \Gamma_6 (p^2 - r^2) \\ \Gamma_7 pq - \Gamma_1 qr \end{bmatrix} + \begin{bmatrix} \Gamma_3 l + \Gamma_5 n \\ \frac{1}{I_y} m \\ \Gamma_4 l + \Gamma_8 n \end{bmatrix}, \tag{2.4}$$

where Γ_i for $i \in (1, 8)$ are given in [17], l, m and n are the roll, pitch and yaw moment, respectively, and I_y is the moment of inertia about the body y-axis.

2.1.2 Control surfaces

Fixed wing aerial vehicles commonly have three types of control surfaces, rudder, elevators and ailerons. The control surfaces are deflected to alter the aerodynamic forces and moments of the aerial vehicle. By altering these forces and moments, the attitude of the aircraft can be controlled. The rudder deflection,

δ_r, mainly controls the yaw angle, ψ, the elevator deflection, δ_e, mainly controls the pitch angle, θ, and the aileron deflection mainly controls the roll angle, ϕ. However, there is also a coupling between the states. For instance, applying a rudder deflection may also induce a roll angle deflection, in addition to the yaw angle.

Elevons

An alternative configuration to the control surface configuration described in subsection 2.1.2 is to have a pair of elevons in place of a separate pair of elevators and ailerons. The left and right elevons, δ_{el} and δ_{er}, driven differentially produce a torque about the body x-axis, $\boldsymbol{x}^b$, acting as a pair of ailerons. While driving the elevon pair together produces a torque about the body y-axis, $\boldsymbol{y}^b$, acting as an elevator. The mathematical relation from elevator and ailerons to elevons is given as

$$\begin{bmatrix} \delta_{er} \\ \delta_{el} \end{bmatrix} = \begin{bmatrix} 1 & -1 \\ 1 & 1 \end{bmatrix} \begin{bmatrix} \delta_e \\ \delta_a \end{bmatrix}. \tag{2.5}$$

This relation allows the calculation of forces and moments for an aircraft equipped with a pair of elevons to use the mathematical models for an aircraft with ailerons and elevator.

2.2 Forces and moments

The forces and moments acting on an aircraft are aerodynamic, gravitational and often propulsion forces and moments. The forces acting on the aircraft are given as $\boldsymbol{F} = \boldsymbol{F}_a + \boldsymbol{F}_g + \boldsymbol{F}_p$, respectively, and similarly the sum of the moments is given as $\boldsymbol{m} = \boldsymbol{m}_a + \boldsymbol{m}_p$. In this section these forces and moments will be explained.

2.2.1 Aerodynamic forces and moments

The aerodynamic forces and moments arise from the aircraft moving through air. These forces and moments are described by aerodynamic coefficients that describe the properties of a given aircraft. These coefficients are difficult to find and are therefore estimated through wind tunnel experiments or computational fluid dynamics (CFD) simulations and analysis.

The aerodynamic forces are the drag, side and lift force. The lift force, as the name implies, describes the amount of lift the aircraft generates. The drag force

describes the force the aircraft has to resist to get through the air. Therefore, for an aircraft to stay aloft it needs to generate more lift than the drag experienced by the aircraft. The lift force is approximately linear in the aircraft's angle of attack, up until a point referred to as the stall limit or the critical angle of attack. When this limit is reached, a sudden reduce in lift occurs, and the aircraft is said to be stalling. The side force of the aircraft is the force perpendicular to the lift and drag force. According to Stengel [16], for most aircraft and intended flight conditions the side force coefficients are small.

The aerodynamic forces can be expressed as

$$\boldsymbol{F}_a = \begin{bmatrix} F_{\text{drag}} \\ F_{\text{side}} \\ F_{\text{lift}} \end{bmatrix} = \bar{q}S \begin{bmatrix} C_D(\alpha, q, \delta_e) \\ C_S(\beta, p, r, \delta_a, \delta_r) \\ C_L(\alpha, q, \delta_e) \end{bmatrix}, \tag{2.6}$$

where $\bar{q} = \frac{\rho V_a^2}{2}$ is the dynamic pressure and S is the wing area of the aircraft. These quantities are called dimensionalizing quantities following from the aerodynamic coefficients being nondimensional. Dimensionless aerodynamic coefficients allow wind tunnel experiments to be conducted on a smaller scale of the aircraft, and be applied to the actual, larger, aircraft [16].

Similarly, the aerodynamic moments can be expressed as

$$\boldsymbol{m}_a = \begin{bmatrix} l \\ m \\ n \end{bmatrix} = \bar{q}S \begin{bmatrix} bC_l(\beta, p, r, \delta_a, \delta_r) \\ cSC_m(\alpha, q, \delta_e) \\ bSC_n(\beta, p, r, \delta_a, \delta_r) \end{bmatrix}, \tag{2.7}$$

where b is the wingspan and c is the mean chord. The moments are known as the roll moment, pitch moment, and yaw moment, respectively.

The force and moment equations are nonlinear, and, as indicated in equations (2.6) and (2.7), the aerodynamic coefficients depend on several variables. The forces and moments can be simplified by a quasi-linear approximation of the coefficients, given by

$$\begin{bmatrix} F_{\text{drag}} \\ F_{\text{side}} \\ F_{\text{lift}} \end{bmatrix} = \bar{q}S \begin{bmatrix} C_D(\alpha) + C_{D_q}(\alpha)\frac{c}{2V_a}q + C_{D_{\delta_e}}\delta_e \\ C_S(\beta) + C_{S_p}(\beta)\frac{b}{2V_a}p + C_{S_r}(\beta)\frac{b}{2V_a}r + C_{S_{\delta_a}}\delta_a + C_{S_{\delta_r}}\delta_r \\ C_L(\alpha) + C_{L_q}(\alpha)\frac{c}{2V_a}q + C_{L_{\delta_e}}\delta_e \end{bmatrix}, \tag{2.8}$$

$$\begin{bmatrix} l \\ m \\ n \end{bmatrix} = \bar{q}S \begin{bmatrix} b\big(C_l(\beta) + C_{l_p}(\beta)\frac{b}{2V_a}p + C_{l_r}(\beta)\frac{b}{2V_a}r + C_{l_{\delta_a}}\delta_a + C_{l_{\delta_r}}\delta_r\big) \\ c\big(C_m(\alpha) + C_{m_q}(\alpha)\frac{c}{2V_a}q + C_{L_{\delta_e}}\delta_e\big) \\ b\big(C_n(\beta) + C_{n_p}(\beta)\frac{b}{2V_a}p + C_{n_r}(\beta)\frac{b}{2V_a}r + C_{n_{\delta_a}}\delta_a + C_{n_{\delta_r}}\delta_r\big) \end{bmatrix}, \tag{2.9}$$

where $\frac{c}{2V_a}$ and $\frac{b}{2V_a}$ are factors to nondimensionalize the coefficients. The aerodynamic coefficients include the nonlinear effects as a function of angle of attack and sideslip.

The forces and moments can also be grouped into longitudinal and lateral components. The longitudinal forces and moments are the drag force, F_{drag}, the lift force, F_{lift}, and the pitch moment, m, while the lateral components are the side force, F_{side}, the roll moment, l, and the yaw moment, n.

Extension to an asymmetric model

In his thesis [6], Kleiven extended the symmetric model of the aircraft to an asymmetric model to simulate asymmetric icing on the wings. Based on the explanation of Kleiven [6], this extension was described in the author's project thesis [18], where the relevant section is repeated below.

The asymmetric model divides the aircraft into two parts, a left side and a right side. The asymmetry is applied to the aerodynamic forces and moments. The total force acting through the center of mass of the aircraft is given by

$$\boldsymbol{F}_k = \boldsymbol{F}_{k,r} + \boldsymbol{F}_{k,l},$$

where k is D, L or S, denoting the drag force, lift force and side force, respectively. The subscripts r and l denote the right and left sides of the aircraft, respectively.

The asymmetric aerodynamic moment is given by

$$\boldsymbol{m}_{a,\text{asym}} = \boldsymbol{m}_{a,0} + \sum_k (\boldsymbol{r}_k \times \boldsymbol{F}_{k,r} + \boldsymbol{l}_k \times \boldsymbol{F}_{l,r}) \quad \text{for } \boldsymbol{F}_{k,r},\, \boldsymbol{F}_{k,l} \notin \boldsymbol{m}_{a,0} \tag{2.10}$$

where $\boldsymbol{m}_{a,0}$ is a vector containing the symmetric moments l, m and n from equation (2.9). The second term in equation (2.10) is due to asymmetry in the corresponding aerodynamic forces on the left and right wing. The asymmetric forces are depicted in figure 2.1 by Kleiven [6]. The following assumptions are made considering the point of attack of the aerodynamic forces [6]

- All points of attack are assumed to lie on the $\pm y$-axis.
- The icing level does not affect the points of attacks' y-coordinate.

Wind to body transformation

Whereas the aerodynamic moments are most easily described in the body-fixed axes, the forces are wind-axis quantities [16]. The transformation from wind to body of the forces consists of a right-handed rotation of the angle of sideslip, β, about the wind z-axis, $\boldsymbol{z}^w$, followed by a left-handed rotation by the angle

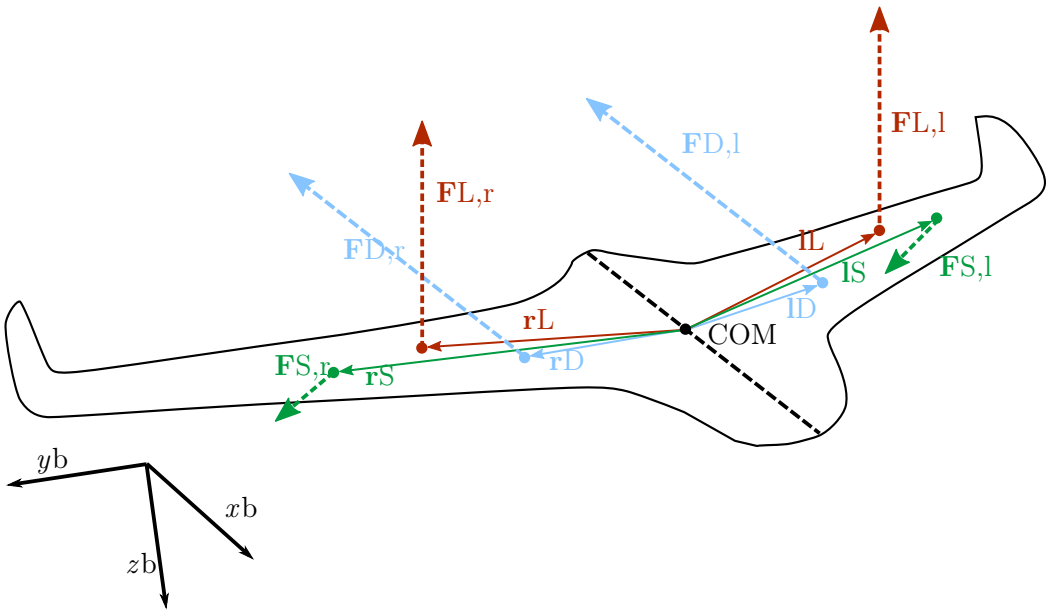

Figure 2.1: The forces of the asymmetric icing model. Courtesy of Kleiven [6].

of attack, α, about the wind y-axis, $\boldsymbol{y}^w$ [19]. The transformation from wind to body is thus given as

$$\boldsymbol{F}_a^b = \begin{bmatrix} \cos -\alpha & 0 & \sin -\alpha \\ 0 & 1 & 0 \\ -\sin -\alpha & 0 & \cos -\alpha \end{bmatrix} \begin{bmatrix} \cos\beta & -\sin\beta & 0 \\ \sin\beta & \cos\beta & 0 \\ 0 & 0 & 1 \end{bmatrix} \boldsymbol{F}_a^w,$$

$$\boldsymbol{F}_a^b = \begin{bmatrix} \cos\beta\cos\alpha & -\sin\beta\cos\alpha & -\sin\alpha \\ \sin\beta & \cos\beta & 0 \\ \cos\beta\sin\alpha & -\sin\beta\sin\alpha & \cos\alpha \end{bmatrix} \boldsymbol{F}_a^w,$$

where $\boldsymbol{F}_a^w = [-F_{\text{drag}},\ F_{\text{side}},\ -F_{\text{lift}}]^\top$. The drag force acts along the negative x-axis, the side force along the positive y-axis and the lift force along the negative z-axis of the wind frame.

2.2.2 Propulsion forces and moments

For an aircraft with a propeller installed, the configuration is usually such that the propulsion force from the propeller is generated in the body x-axis, $\boldsymbol{x}^b$. This force is given by

$$\boldsymbol{F}_{\text{prop}}^b = \begin{bmatrix} \frac{1}{2}\rho S_{\text{prop}} C_{\text{prop}} V_d (V_d - V_a) \\ 0 \\ 0 \end{bmatrix},$$

where S_{prop} is the area of the propeller, C_{prop} is the aerodynamic coefficient for the propeller and $V_d = V_a + \delta_t(k_{\text{motor}} - V_a)$ is the discharge velocity from the propeller, where δ_t is the throttle, k_{motor} is the motor constant and V_a is the airspeed [20].

The propulsion moment is given by

$$\boldsymbol{m}^b_{\text{prop}} = \begin{bmatrix} -k_{T_p}(k_\Omega \delta_t^2) \\ 0 \\ 0 \end{bmatrix},$$

where $k_\Omega \delta_t$ is the propeller speed and k_{T_p} is a constant determined by experiment [17].

2.2.3 Gravitational forces

The gravitational force acts on the aircraft in the inertial z-axis, $\boldsymbol{z}^i$, direction and is given by the product of the mass of the aircraft and the gravitational constant, g. With a rotation from the inertial frame, i, to the body frame, b, the force is given by

$$\boldsymbol{F}^b_g = \boldsymbol{R}^b_i \begin{bmatrix} 0 \\ 0 \\ \mathrm{m}g \end{bmatrix},$$

where $\boldsymbol{R}^b_i$ is the rotation matrix from the inertial frame, i, to the body frame, b.

2.3 Inner loop controllers

In this section, inner loop controllers are described. Inner loop control consists of the control of the angular velocities and Euler angles, in contrast to outer loop control, which generates the reference signal for the inner loop. An adaptive control scheme and a PID controller are described.

2.3.1 Model Reference Adaptive Control (MRAC)

An adaptive controller is said by Åstrøm and Wittenmark [8] to be "a controller with adjustable parameters and a mechanism for adjusting the parameters". The adaptive controller will modify and adapt its behavior as the plant dynamics change or a disturbance is introduced to the system. This adaptation

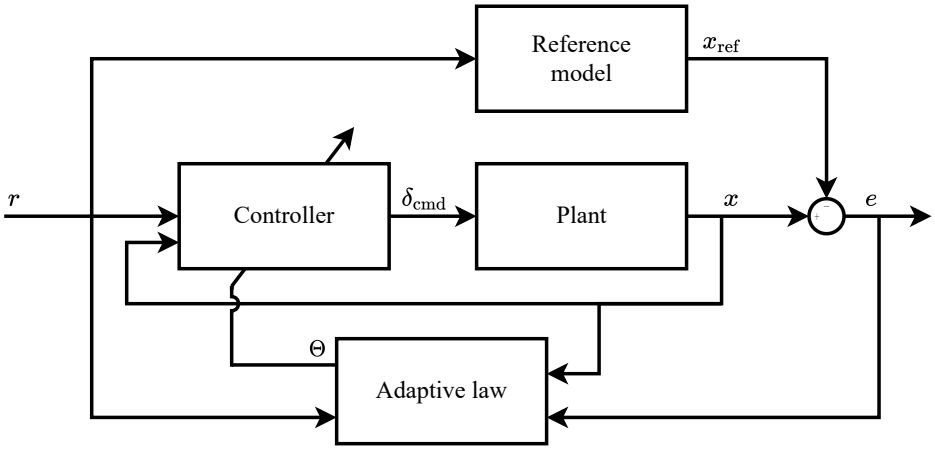

Figure 2.2: Block diagram of the MRAC scheme.

of the parameters of the controller is one of two loops of the adaptive control scheme, wherein the second loop is for feedback control of the system.

A model reference adaptive controller (MRAC) is an adaptive control scheme where the aim is to have the system track a reference model that describes the desired behavior of the closed-loop system. The control scheme can be categorized into two groups: direct and indirect adaptive controllers. With a direct adaptive controller, the controller gains are adjusted directly based on the tracking error. With an indirect adaptive control scheme, the controller gains are adjusted indirectly based on estimates of the plant parameters [7]. The controller structure of the MRAC scheme is shown in figure 2.2.

In this section, the model reference adaptive control scheme is presented, based on the explanations by Lavretsky and Wise [9].

Consider the nonlinear system

$$\dot{\boldsymbol{x}} = \boldsymbol{A}\boldsymbol{x} + \boldsymbol{B}\boldsymbol{\Lambda}(\boldsymbol{u} + f(\boldsymbol{x})), \tag{2.11}$$

where $\boldsymbol{x} \in \mathbb{R}^n$ is the state vector, $\boldsymbol{u} \in \mathbb{R}^m$ is the control input, $\boldsymbol{B} \in \mathbb{R}^{n\times m}$ is the known control matrix, $\boldsymbol{\Lambda} \in \mathbb{R}^{m\times m}$ is the unknown control effectiveness matrix and $\boldsymbol{A} \in \mathbb{R}^{n\times n}$ is the unknown system matrix. It is assumed that $f(\boldsymbol{x})$ can be written as

$$f(\boldsymbol{x}) = \boldsymbol{\Theta}^\top \Phi(\boldsymbol{x}), \tag{2.12}$$

where $\boldsymbol{\Theta} \in \mathbb{R}^{N\times m}$ is constant and unknown, and $\boldsymbol{\Phi}(\boldsymbol{x}) \in \mathbb{R}^N$ is the known regressor vector. The matrices $\boldsymbol{A}$ and $\boldsymbol{\Lambda}$ are assumed constant, and $\boldsymbol{\Lambda}$ is assumed to be diagonal with its elements $\lambda_i > 0$. Additionally, it is assumed that the pair $(\boldsymbol{A}, \boldsymbol{B\Lambda})$ is controllable. That is, the matrix $[\boldsymbol{B\Lambda} \;\; \boldsymbol{AB\Lambda} \;\; \dots \;\; \boldsymbol{A}^{n-1}\boldsymbol{B\Lambda}]$ is assumed to have full row rank.

The control objective of the model reference adaptive controller is to have the system state in equation (2.11) track the reference model

$$\dot{\boldsymbol{x}}_{\text{ref}} = \boldsymbol{A}_{\text{ref}}\boldsymbol{x}_{\text{ref}} + \boldsymbol{B}_{\text{ref}}\boldsymbol{r}(t), \tag{2.13}$$

driven by the commanded reference, $\boldsymbol{r}(t)$. The matrix is $\boldsymbol{A}_{\text{ref}} \in \mathbb{R}^{n\times n}$ is Hurwitz[1] and $\boldsymbol{B}_{\text{ref}} \in \mathbb{R}^{n\times m}$ is the input matrix. Thus, the reference model describes the desired behavior of the system. The ideal control law, if the matrices $\boldsymbol{A}$ and $\boldsymbol{\Lambda}$ are known, is given by

$$\boldsymbol{u} = \boldsymbol{K_x}^\top \boldsymbol{x} + \boldsymbol{K_r}^\top \boldsymbol{r} - \boldsymbol{\Theta}^\top \boldsymbol{\Phi}(\boldsymbol{x}). \tag{2.14}$$

Equating the dynamics of the system in equation (2.11) and the reference model in equation (2.13)

$$\begin{aligned} \dot{\boldsymbol{x}} &= \dot{\boldsymbol{x}}_{\text{ref}}, \\ \boldsymbol{A}\boldsymbol{x} + \boldsymbol{B}\boldsymbol{\Lambda}(\boldsymbol{u} + \boldsymbol{\Theta}^\top \Phi(\boldsymbol{x})) &= \boldsymbol{A}_{\text{ref}}\boldsymbol{x}_{\text{ref}} + \boldsymbol{B}_{\text{ref}}\boldsymbol{r}(t), \end{aligned}$$

and inserting the ideal control law in equation (2.14) such that

$$\begin{aligned} \boldsymbol{A}\boldsymbol{x} + \boldsymbol{B}\boldsymbol{\Lambda}\Big(\big(\boldsymbol{K_x}^\top \boldsymbol{x} + \boldsymbol{K_r}^\top \boldsymbol{r} - \boldsymbol{\Theta}^\top \boldsymbol{\Phi}(\boldsymbol{x})\big) + \boldsymbol{\Theta}^\top \boldsymbol{\Phi}(\boldsymbol{x})\Big) &= \boldsymbol{A}_{\text{ref}}\boldsymbol{x}_{\text{ref}} + \boldsymbol{B}_{\text{ref}}\boldsymbol{r}, \\ (\boldsymbol{A} + \boldsymbol{B}\boldsymbol{\Lambda}\boldsymbol{K}_x^\top)\boldsymbol{x} + \boldsymbol{B}\boldsymbol{\Lambda}\boldsymbol{K}_r^\top \boldsymbol{r} &= \boldsymbol{A}_{\text{ref}}\boldsymbol{x}_{\text{ref}} + \boldsymbol{B}_{\text{ref}}\boldsymbol{r}, \end{aligned}$$

gives the matching conditions

$$\begin{aligned} \boldsymbol{A} + \boldsymbol{B}\boldsymbol{\Lambda}\boldsymbol{K}_x^\top &= \boldsymbol{A}_{\text{ref}}, \\ \boldsymbol{B}\boldsymbol{\Lambda}\boldsymbol{K}_r^\top &= \boldsymbol{B}_{\text{ref}}. \end{aligned} \tag{2.15}$$

From Lavretsky and Wise [9], the matching conditions imply that if the uncertainties of the system were known, a controller could cancel them out and match the plant dynamics to the reference model dynamics.

Tracking of the reference model is achieved with the control law

$$\boldsymbol{u} = \hat{\boldsymbol{K}}_x^\top \boldsymbol{x} + \hat{\boldsymbol{K}}_r^\top \boldsymbol{r} - \hat{\boldsymbol{\Theta}}^\top \boldsymbol{\Phi}(\boldsymbol{x}), \tag{2.16}$$

where $\hat{\boldsymbol{K}}_x \in \mathbb{R}^{n\times m}$, $\hat{\boldsymbol{K}}_r \in \mathbb{R}^{m\times m}$ and $\hat{\boldsymbol{\Theta}} \in \mathbb{R}^{N\times m}$ are estimates of the gain matrices of the ideal controller gains that will ensure tracking of the reference model dynamics. The adaptive law for the gains are found through Lyapunov analysis.

Consider the state tracking error given by $\boldsymbol{e}(t) = \boldsymbol{x}(t) - \boldsymbol{x}_{\text{ref}}(t)$, the error dynamics are given as

$$\dot{\boldsymbol{e}} = \dot{\boldsymbol{x}} - \dot{\boldsymbol{x}}_{\text{ref}} \tag{2.17}$$

$$\dot{\boldsymbol{e}} = (\boldsymbol{A} + \boldsymbol{B}\boldsymbol{\Lambda}\hat{\boldsymbol{K}}_x^\top)\boldsymbol{x} + \boldsymbol{B}\boldsymbol{\Lambda}\big(\hat{\boldsymbol{K}}_r^\top \boldsymbol{r} - (\hat{\boldsymbol{\Theta}} - \boldsymbol{\Theta})^\top \boldsymbol{\Phi}(\boldsymbol{x})\big) - \boldsymbol{A}_{\text{ref}}\boldsymbol{x}_{\text{ref}} + \boldsymbol{B}_{\text{ref}}\boldsymbol{r} \tag{2.18}$$

[1] A matrix is Hurwitz if every eigenvalue of the matrix has negative real parts.

where $\dot{\boldsymbol{x}}$ is the closed loop dynamics of equation (2.11) with the control law given in equation (2.16), and $\dot{\boldsymbol{x}}_{\text{ref}}$ is given by the reference model dynamics in equation (2.13).

Introducing $\Delta \boldsymbol{K}_x = \hat{\boldsymbol{K}}_x - \boldsymbol{K}_x$, $\Delta \boldsymbol{K}_r = \hat{\boldsymbol{K}}_r - \boldsymbol{K}_r$ and $\Delta \boldsymbol{\Theta} = \hat{\boldsymbol{\Theta}} - \boldsymbol{\Theta}$ as parameter estimation errors, the error dynamics in equation (2.17) can be written as

$$\begin{aligned}\dot{\boldsymbol{e}} &= \big(\boldsymbol{A} + \boldsymbol{B}\boldsymbol{\Lambda}(\boldsymbol{K}_x + \Delta\boldsymbol{K}_x)^\top\big)\boldsymbol{x} + \boldsymbol{B}\boldsymbol{\Lambda}\big((\boldsymbol{K}_r + \Delta\boldsymbol{K}_r)^\top \boldsymbol{r} - \Delta\boldsymbol{\Theta}^\top \boldsymbol{\Phi}(\boldsymbol{x})\big) \\ &\quad - \boldsymbol{A}_{\text{ref}}\boldsymbol{x}_{\text{ref}} - \boldsymbol{B}_{\text{ref}}\boldsymbol{r}, \\ &= (\boldsymbol{A} + \boldsymbol{B}\boldsymbol{\Lambda}\boldsymbol{K}_x^\top)\boldsymbol{x} + \boldsymbol{B}\boldsymbol{\Lambda}\Delta\boldsymbol{K}_x^\top\boldsymbol{x} + \boldsymbol{B}\boldsymbol{\Lambda}\boldsymbol{K}_r^\top\boldsymbol{r} + \boldsymbol{B}\boldsymbol{\Lambda}\Delta\boldsymbol{K}_r^\top\boldsymbol{r} - \boldsymbol{B}\boldsymbol{\Lambda}\Delta\boldsymbol{\Theta}^\top\boldsymbol{\Phi}(\boldsymbol{x}) \\ &\quad - \boldsymbol{A}_{\text{ref}}\boldsymbol{x}_{\text{ref}} - \boldsymbol{B}_{\text{ref}}\boldsymbol{r}.\end{aligned} \tag{2.19}$$

Inserting the matching conditions from equation (2.15) into equation (2.19), gives the error dynamics

$$\dot{\boldsymbol{e}} = \boldsymbol{A}_{\text{ref}}\boldsymbol{e} + \boldsymbol{B}\boldsymbol{\Lambda}\big(\Delta\boldsymbol{K}_x^\top\boldsymbol{x} + \Delta\boldsymbol{K}_r^\top\boldsymbol{r} - \Delta\boldsymbol{\Theta}^\top\boldsymbol{\Phi}(\boldsymbol{x})\big). \tag{2.20}$$

Given the following Lyapunov function candidate

$$\begin{aligned}V(\boldsymbol{e}, \Delta\boldsymbol{K}_x, \Delta\boldsymbol{K}_r, \Delta\boldsymbol{\Theta}) = \boldsymbol{e}^\top\boldsymbol{P}\boldsymbol{e} + \text{tr}\Big(\big[&\Delta\boldsymbol{K}_x^\top\boldsymbol{\Gamma}_x^{-1}\Delta\boldsymbol{K}_x + \Delta\boldsymbol{K}_r^\top\boldsymbol{\Gamma}_r^{-1}\Delta\boldsymbol{K}_r \\ &+ \Delta\boldsymbol{\Theta}^\top\boldsymbol{\Gamma}^{-1}\Delta\boldsymbol{\Theta}\big]\boldsymbol{\Lambda}\Big),\end{aligned} \tag{2.21}$$

selecting the adaptive laws for the controller gains in equation (2.16) as

$$\begin{aligned}\dot{\hat{\boldsymbol{K}}}_x &= -\boldsymbol{\Gamma}_x\boldsymbol{x}\boldsymbol{e}^\top\boldsymbol{P}\boldsymbol{B} \\ \dot{\hat{\boldsymbol{K}}}_r &= -\boldsymbol{\Gamma}_r\boldsymbol{r}\boldsymbol{e}^\top\boldsymbol{P}\boldsymbol{B} \\ \dot{\hat{\boldsymbol{\Theta}}} &= \boldsymbol{\Gamma}_\Theta\boldsymbol{\Phi}(\boldsymbol{x})\boldsymbol{e}^\top\boldsymbol{P}\boldsymbol{B},\end{aligned} \tag{2.22}$$

will render the closed-loop error dynamics uniformly stable, where $\boldsymbol{\Gamma}_x = \boldsymbol{\Gamma}_x^\top > 0$, $\boldsymbol{\Gamma}_r = \boldsymbol{\Gamma}_r^\top > 0$ and $\boldsymbol{\Gamma}_\Theta = \boldsymbol{\Gamma}_\Theta^\top > 0$ are the adaptation rates. In equation (2.21) tr is the trace of a matrix, and $\boldsymbol{P} = \boldsymbol{P}^\top > 0$ satisfies the algebraic Lyapunov equation

$$\boldsymbol{P}\boldsymbol{A}_{\text{ref}} + \boldsymbol{A}_{\text{ref}}^\top\boldsymbol{P} = -\boldsymbol{Q}, \tag{2.23}$$

for $\boldsymbol{Q} = \boldsymbol{Q}^\top > 0$. The calculation of the derivative of the Lyapunov function candidate in equation (2.21) leading to the adaptive law in equation (2.22) can be found in Lavretsky and Wise [9].

Stability properties and parameter convergence

From the stability proof in Lavretsky and Wise [9], the MRAC system described in section 2.3.1 enforces global uniform asymptotic tracking performance of

the reference model dynamics, driven by a bounded time-varying commanded reference, $\boldsymbol{r}(t)$. That is, the tracking error $\boldsymbol{e} = \boldsymbol{x} - \boldsymbol{x}_{\text{ref}}$ converges to zero asymptotically. Further, the stability proof shows that all signals in the closed-loop system remain uniformly bounded in time.

In general, parameter convergence of the adaptive controller gains to their ideal values given by the matching conditions is not guaranteed by the MRAC control scheme. The stability proofs only guarantee uniform boundedness of the parameters. The sufficient conditions for obtaining parameter convergence are persistency of excitation (PE) of the reference input. For linear systems a sum of sinusoidal signals with different frequencies as the reference input ensures sufficient excitation of the system and fulfills the PE condition for parameter convergence. However, for more complicated, non-linear systems, the PE conditions are hard to verify numerically [9].

2.3.2 Projection

In the presence of unmatched disturbances or non-parametric disturbances, such as unmodelled dynamics and process noise, the adaptive parameters may experience drifting and are no longer guaranteed to be bounded. To this end, the MRAC laws may be modified to enforce robustness. Lavretsky and Wise [9] present several robustness techniques, among them the dead-zone modification, the e-modification and the projection operator. In this thesis, the projection operator from [9] is presented.

The projection operator enables the adaptive laws of the MRAC scheme to achieve robustness with respect to both parametric and non-parametric uncertainties. The operator ensures uniform boundedness of the adaptive parameters. Keeping the adaptive parameters constrained also prevents the integrators of the adaptive laws in equation (2.22) from winding up. That is, the projection operator functions as an anti-windup technique for the adaptive control scheme.

The projection operator is given as

$$\text{Proj}(\theta, y) = \begin{cases} y - \frac{\Gamma \nabla f(\theta)(\nabla f(\theta))^\top}{\|\nabla f(\theta)\|_\Gamma^2} y f(\theta) & , \text{ if } [f(\theta) > 0 \wedge y^\top f(\theta) > 0] \\ y & , \text{ if not,} \end{cases} \tag{2.24}$$

where θ is the estimated parameter vector, driven by $y = y(t)$, $\Gamma \in \mathbb{R}^{n \times n}$ is any constant symmetric positive definites matrix and $\|\nabla f\|_\Gamma^2 = (\nabla f)^\top \Gamma \nabla f$ is the weighed Euclidean squared norm of ∇f. The function $f : \mathbb{R}^n \to \mathbb{R}$ is a

differentiable convex function, chosen by Lavretsky and Wise [9] as

$$f(\hat{\boldsymbol{\Theta}}) = \frac{\left(1+\varepsilon^{\Theta}\right)\|\hat{\boldsymbol{\Theta}}\|^2 - \left(\Theta^{\max}\right)^2}{\varepsilon^{\Theta}\left(\Theta^{\max}\right)^2},$$

for the projection-based MRAC design, with its gradient given by

$$\nabla f = \frac{2\left(1+\varepsilon^{\Theta}\right)}{\varepsilon^{\Theta}\Theta^{\max}}\hat{\boldsymbol{\Theta}},$$

where $\varepsilon^{\Theta} > 0$ is noted as the projection tolerance and $\Theta^{\max}$ is the desired upper bound of the adaptive parameter vector $\|\hat{\boldsymbol{\Theta}}\| \leq \Theta^{\max}$.

The adaptive law for $\hat{\boldsymbol{\Theta}}$ then becomes $\dot{\hat{\boldsymbol{\Theta}}} = \mathrm{Proj}(\hat{\boldsymbol{\Theta}}, \boldsymbol{\Gamma}_{\Theta}(\boldsymbol{\Phi}\boldsymbol{e}^{\top}\boldsymbol{P}\boldsymbol{B})$, that is,

$$\dot{\hat{\boldsymbol{\Theta}}} = \boldsymbol{\Gamma}_{\boldsymbol{\Theta}} \begin{cases} \boldsymbol{\Phi}\boldsymbol{e}^{\top}\boldsymbol{P}\boldsymbol{B} - \frac{\boldsymbol{\Gamma}\nabla f \nabla f^{\top}}{\|\nabla f\|_{\Gamma}^2}(\boldsymbol{\Phi}\boldsymbol{e}^{\top}\boldsymbol{P}\boldsymbol{B})f, & \text{if } [f > 0 \wedge \boldsymbol{\Gamma}_{\boldsymbol{\Theta}}(\boldsymbol{\Phi}\boldsymbol{e}^{\top}\boldsymbol{P}\boldsymbol{B})^{\top}\nabla f > 0] \\ \boldsymbol{\Phi}\boldsymbol{e}^{\top}\boldsymbol{P}\boldsymbol{B}, & \text{if not.} \end{cases} \tag{2.25}$$

2.3.3 PID controllers

The proportional-integral-derivative (PID) inner loop controllers for a UAV designed by Beard & McLain in [17] are described in this section. The design of the controllers is based on linear transfer function models of the aircraft.

The PID controller for roll is given by

$$\delta_a = k_{p_\phi}(\phi^c - \phi) + \frac{k_{i_\phi}}{s}(\phi^c - \phi) - k_{d_\phi}p,$$

where ϕ^c is the commanded roll angle and k_{p_ϕ}, k_{i_ϕ} and k_{d_ϕ} are the control gains.

Similarly, the PID controller for pitch is given by

$$\delta_e = k_{p_\theta}(\theta^c - \theta) - k_{d_\theta}q, \tag{2.26}$$

where θ^c is the commanded pitch angle and k_{p_θ}, k_{d_θ} are the control gains.

The PI controller for airspeed control using throttle is given by

$$\delta_t = \delta_t^* + k_{p_V}(V_a^c - V_a) + \frac{k_{i_V}}{s}(V_a^c - V_a), \tag{2.27}$$

where δ_t^* is the throttle trim value, and k_{p_V}, k_{i_V} are the control gains.

2.4 Guidance

This section presents the guidance laws for tracking straight lines in both the lateral and longitudinal direction. The objective of the guidance laws is to have the aircraft follow a predetermined path. Note that path following is independent of time and does not require the vehicle to be at a specified point at a given time, in contrast to trajectory tracking which is time dependent. The guidance laws take in a predetermined path as a set of waypoints and provide the commanded roll angle, pitch angle, and airspeed necessary to follow the path.

2.4.1 Lateral guidance law

From Fossen [21] a proportional line-of-sight (LOS) path following guidance law is given by a desired course angle, χ_d, as

$$\chi_d = \chi_p - \tan^{-1}\Big(\frac{y_e^p}{\Delta_{\text{lat}}}\Big), \tag{2.28}$$

where χ_p is the path-tangential angle, y_e is the cross-track error, and Δ_{lat} is the lookahead distance. The path-tangential angle is found by

$$\chi_p = \text{atan2}(y_{k+1} - y_k, x_{k+1} - x_k), \tag{2.29}$$

and the cross-track error is found by

$$y_e = -(x(t) - x_k)\sin\chi_p + (y(t) - y_k)\cos\chi_p, \tag{2.30}$$

where (x_k, y_k) is the position of the current waypoint, (x_{k+1}, y_{k+1}) is the position of the next waypoint and $(x(t), y(t))$ is the current position of the aircraft in the xy-plane. The lookahead distance, Δ_{lat}, is a tuning variable.

From [17], a course controller that calculates the commanded roll angle for tracking the desired course angle, χ_d, in equation (2.28) is given by

$$\phi^c = k_{p_\chi}(\chi^c - \chi) + \frac{k_{i_\chi}}{s}(\chi^c - \chi).$$

Alternatively, a coordinated turn control scheme can also be used to track the desired course angle, χ_d.

2.4.2 Longitudinal guidance law

Given some preliminaries, a longitudinal LOS guidance law developed by You [22] and the work of Nevstad [23], can be described analogously to the lateral guidance law in section 2.4.1.

The first step is to define the projection of the along-track distance to the xy-plane as

$$S_{xy} = \cos(\chi_p)(x(t) - x_k) + \sin(\chi_p)(y(t) - y_k), \tag{2.31}$$

and the length from $\boldsymbol{p}_k^i$ to $\boldsymbol{p}_{k+1}^i$ on the projection of the path onto the xy-plane as

$$L_{xy} = \sqrt{(x_{k+1} - x_k)^2 + (y_{k+1} - y_k)^2}, \tag{2.32}$$

where $\boldsymbol{p}_k^i = [x_k, y_k, z_k]^\top$ is the position of the current waypoint and $\boldsymbol{p}_{k+1}^i = [x_{k+1}, y_{k+1}, z_{k+1}]^\top$ is the position of the next waypoint. With these definitions in place, an analogous guidance law to the lateral guidance law in section 2.4.1 can be made by considering the pair $(-(z_{k+1} - z_k), L_{xy})$ to be analogous to $(y_{k+1} - y_k, x_{k+1} - x_k)$ and the pair $(S_{xy}, z(t) - z_k)$ to be analogous to $(-(x(t) - x_k), y(t) - y_k)$.

The longitudinal guidance law is then given as

$$\gamma_d = \gamma_p + \tan^{-1}\Big(\frac{k_{ph} z_e + k_{ih} \int z_e \, d\tau}{\Delta_{\text{lon}}}\Big), \tag{2.33}$$

where the longitudinal lookahead distance is given by $\Delta_{\text{lon}} = \sqrt{R_{\max}^2 - z_e^2}$ and $R_{\max}$ is the maximum allowed value for Δ_{lon}.

Similarly to equation (2.29), γ_p is defined as

$$\gamma_p = \text{atan2}(-(z_{k+1} - z_k), L_{xy}), \tag{2.34}$$

and the vertical cross-track error is defined as

$$z_e = S_{xy} \sin \gamma_p + (z(t) - z_k) \cos \gamma_p. \tag{2.35}$$

Finally, a flight path angle controller that calculates the commanded pitch angle for tracking the desired flight path angle, γ_d, in equation (2.33) is given by [24] in equation (2.36) where $c_1 > -1$:

$$\theta^d = -c_1(\gamma - \gamma_d) + \gamma_d + \alpha_{\text{trim}}. \tag{2.36}$$

See for instance Nevstad [23] or You [22] for illustrations of the angle and lengths described in this section.

2.4.3 Airspeed controller

The accompanying airspeed controller to the guidance laws is given by

$$\delta_t = \delta_t^* + k_{p_V}(V_a^c - V_a) + \frac{k_{i_V}}{s}(V_a^c - V_a) + k_{p_{z_e}} z_e(t).$$

This is the airspeed controller given in equation (2.27), modified to include a feed-forward term $k_{p_{z_e}} z_e(t)$. The feed-forward term is added to improve the vertical tracking.

2.5 Environmental factors

In this section, two of the environmental factors that affect a UAV are described, namely icing conditions and wind conditions.

2.5.1 Icing conditions

Atmospheric ice accretion on an aircraft can have a critical impact on the aerodynamics, causing a decrease in lift, increase in drag and moving the stall limit lower [1]. The stall limit is reduced as the ice formed on the airfoil causes the airflow to separate from the airfoil at a lower angle of attack. Moreover, the changes in lift and drag imply that a greater thrust force is needed to compensate for the effects of icing. Hann *et al.* [3] show that smaller UAVs, compared to larger and faster manned aircraft, are more affected by ice accretion.

Furthermore, ice accretion on the airfoils ahead of control surfaces such as ailerons, elevator and rudders also results in a reduced control surface effectiveness [2]. The severity of the loss in control effectiveness is governed by three fluid dynamic properties described in [2].

The three main types of icing conditions are glaze, rime and mixed ice, wherein mixed icing lies in between the glaze and rime categorizations. Glaze ice occurs at temperatures from 0°C and −3°C, and they tend to have a rough surface and double horns, while rime ice occurs at temperatures below −10°C and tend to have a single horn and a relatively smooth surface [2]. By the findings of Hann *et al.* in [25] mixed icing is considered the most severe type of icing conditions with respect to the degradation in aerodynamic effectiveness. [25] also shows that for mixed icing, the curve for the aerodynamic lift coefficient is shifted to the left. As a consequence of this either the velocity of the UAV or the angle of attack must be increased to maintain its position in the flight envelope [25].

There are two main methods of ice protection systems to cope with ice accretion on the leading edge of the airfoil, namely de-icing and anti-icing methods. Anti-icing consists of continuously applying heat to the airfoils to prevent any icing forming. While de-icing consists of periodically applying heat to remove already formed ice. Both require an increase in power consumption, although [4] suggests that anti-icing demands more power usage than de-icing.

2.5.2 Wind models

Wind is a stochastic atmospheric disturbance that has a more severe effect on smaller aircraft such as UAVs than on traditional larger aircraft. The wind is not as severe for the larger aircraft, since they travel at a greater speed than the smaller UAVs. For the UAVs travelling at 15-25 m/s the wind speed is often half the speed of the UAV or even greater. The wind can be assumed to consist of steady ambient wind and wind gusts [17]. The description of the gust portion of the wind was described in the author's project thesis [18] and is repeated below.

The gust portion of the wind can be modeled by the von Karmen model, where white noise is passed through a linear time-invariant filter given by the von Karmen spectrum. From Beard and McLain [17], this method does not result in a rational transfer function, and thus the alternative Dryden model is often used.

The Dryden model is an approximation of the von Karman model and consists of six filters that white noise is passed through to produce the gust components for the translational and angular wind velocities. From MATLAB's documentation [26], these filters are given, based on the military specification MIL-F-8785C [27], as

$$H_u(s) = \sigma_u\sqrt{\frac{2L_u}{\pi V_a}}\frac{1}{1+\frac{L_u}{V_a}s}, \qquad H_p(s) = \sigma_w\sqrt{\frac{0.8}{V_a}}\frac{\left(\frac{\pi}{4b}\right)^{\frac{1}{6}}}{L_w^{\frac{1}{3}}\left(1+\frac{4b}{\pi V_a}s\right)},$$

$$H_v(s) = \sigma_v\sqrt{\frac{L_v}{\pi V_a}}\frac{1+\frac{\sqrt{3}L_v}{V_a}s}{\left(1+\frac{L_v}{V_a}s\right)^2}, \qquad H_q(s) = \frac{-\frac{s}{V_a}}{1+\frac{4b}{\pi V_a}s}H_w(s),$$

$$H_w(s) = \sigma_w\sqrt{\frac{L_w}{\pi V_a}}\frac{1+\frac{\sqrt{3}L_w}{V_a}s}{\left(1+\frac{L_w}{V_a}s\right)^2}, \qquad H_r(s) = \frac{\frac{s}{V_a}}{1+\frac{3b}{\pi V_a}s}H_v(s),$$

where σ_u, σ_v and σ_w are the turbulence intensities and L_u, L_v and L_w are the turbulence scale lengths. V_a is the airspeed and b is the wingspan of the UAV. The values of the parameters describing the six filters are given by

$$\begin{aligned}
L_w &= h,\\
L_u &= L_v = \frac{h}{(0.177+0.000823h)^{1.2}},\\
\sigma_w &= 0.1W_{20},\\
\frac{\sigma_u}{\sigma_w} &= \frac{\sigma_v}{\sigma_w} = \frac{1}{(0.177+0.000823h)^{0.4}},
\end{aligned}$$

for altitudes below 1000 feet, where W_{20} is the wind speed at 6 meters [26].

The steady portion of the wind can be modelled as a wind speed vector in the xy-plane given by

$$\boldsymbol{V}_w^i = \boldsymbol{R}_z(\psi_w) \begin{bmatrix} V_w \\ 0 \\ 0 \end{bmatrix}, \tag{2.37}$$

where V_w is the wind speed, ψ_w is the wind direction and $\boldsymbol{R}_z(\psi_w)$ decomposes the wind V_w to its x and y components based on the wind direction. The steady wind is transformed to the body frame by the rotation $\boldsymbol{R}_i^b$, that is,

$$\boldsymbol{V}_w^b = \boldsymbol{R}_i^b \boldsymbol{V}_w^i. \tag{2.38}$$

Part II

Methodology

Chapter 3

Controllers

In this chapter, the specifics of the implementation of the MRAC scheme and PID controller are presented.

3.1 MRAC controllers

Summarized from section 2.3.1, the model reference adaptive control structure is given by the model equations

$$\dot{\boldsymbol{x}} = \boldsymbol{A}\boldsymbol{x} + \boldsymbol{B}\boldsymbol{\Lambda}(\boldsymbol{u} + \boldsymbol{\Theta}^\top \boldsymbol{\Phi}(\boldsymbol{x})), \tag{3.1}$$

with the control input given as

$$\boldsymbol{u} = \hat{\boldsymbol{K}}_x^\top \boldsymbol{x} + \hat{\boldsymbol{K}}_r^\top \boldsymbol{r} - \hat{\boldsymbol{\Theta}}^\top \boldsymbol{\Phi}(\boldsymbol{x}).$$

To increase the robustness of the control scheme, the adaptive parameters in this thesis are estimated by the MRAC adaptive laws with projection, described in section 2.3.2,

$$\begin{aligned} \dot{\hat{\boldsymbol{K}}}_x &= \text{Proj}(\hat{\boldsymbol{K}}_x,\ -\boldsymbol{\Gamma}_{\boldsymbol{x}} \boldsymbol{x}\boldsymbol{e}^\top \boldsymbol{P}\boldsymbol{B}), \\ \dot{\hat{\boldsymbol{K}}}_r &= \text{Proj}(\hat{\boldsymbol{K}}_r,\ -\boldsymbol{\Gamma}_{\boldsymbol{r}} \boldsymbol{r}\boldsymbol{e}^\top \boldsymbol{P}\boldsymbol{B}), \\ \dot{\hat{\boldsymbol{\Theta}}} &= \text{Proj}(\hat{\boldsymbol{\Theta}},\ \boldsymbol{\Gamma}_{\boldsymbol{\Theta}} \boldsymbol{\Phi}\boldsymbol{e}^\top \boldsymbol{P}\boldsymbol{B}). \end{aligned} \tag{3.2}$$

As mentioned in section 2.3.2, the projection operator provides anti-windup to the integrators of the adaptive laws and ensures uniform boundedness of the adaptive parameters.

3.1.1 Model equations

The model in the MRAC control scheme is chosen as a linear model with the addition of a bias term to capture nonlinear and unmodelled effects. From Beard & McLain [17], a linearization of the roll dynamics is given as

$$\begin{aligned} \dot{\phi} &= p + d_{\phi_1}, \\ \ddot{\phi} &= -a_{\phi_1}\dot{\phi} + a_{\phi_2}\delta_a + d_{\phi_2}, \end{aligned} \tag{3.3}$$

where d_{ϕ_1} and d_{ϕ_2} consists of the nonlinear terms of the dynamics and are, for the linear model, considered disturbances on the system. A model of the roll dynamics on the form in equation (3.1) using equation (3.3) is then given by

$$\begin{aligned} \dot{\boldsymbol{x}} &= \boldsymbol{A}\boldsymbol{x} + \boldsymbol{B}\boldsymbol{\Lambda}(\boldsymbol{u} + \boldsymbol{\Theta}^\top \boldsymbol{\Phi}(\boldsymbol{x})), \\ \begin{bmatrix} \dot{\phi} \\ \dot{p} \end{bmatrix} &= \begin{bmatrix} 0 & 1 \\ 0 & a_1 \end{bmatrix} \begin{bmatrix} \phi \\ p \end{bmatrix} + \begin{bmatrix} 0 \\ 1 \end{bmatrix} \lambda_1 \Big(\delta_a + \begin{bmatrix} \theta_{\text{bias, roll}} \end{bmatrix} \begin{bmatrix} 1 \end{bmatrix} \Big), \end{aligned} \tag{3.4}$$

where $a_1 = -a_{\phi_1}$, $\lambda_1 = a_{\phi_2}$ and $\theta_{\text{bias, roll}} = d_{\phi_2}$, and the pair $(\boldsymbol{A}, \boldsymbol{B}\boldsymbol{\Lambda})$ is controllable since the matrix $[\boldsymbol{B}\boldsymbol{\Lambda} \;\; \boldsymbol{A}\boldsymbol{B}\boldsymbol{\Lambda}]$ is of full rank.

Similarly, a linearization of the pitch dynamics is given by Beard & McLain [17] as

$$\dot{\theta} = q + d_{\theta_1}, \tag{3.5}$$

$$\ddot{\theta} = -a_{\theta_1}\dot{\theta} - a_{\theta_2}\theta + a_{\theta_3}\delta_e + d_{\theta_2}, \tag{3.6}$$

gives the pitch model

$$\begin{aligned} \dot{\boldsymbol{x}} &= \boldsymbol{A}\boldsymbol{x} + \boldsymbol{B}\boldsymbol{\Lambda}(\boldsymbol{u} + \boldsymbol{\Theta}^\top \boldsymbol{\Phi}(\boldsymbol{x})), \\ \begin{bmatrix} \dot{\theta} \\ \dot{q} \end{bmatrix} &= \begin{bmatrix} 0 & 1 \\ a_2 & a_3 \end{bmatrix} \begin{bmatrix} \theta \\ q \end{bmatrix} + \begin{bmatrix} 0 \\ 1 \end{bmatrix} \lambda_2 \Big(\delta_e + \begin{bmatrix} \theta_{\text{bias, pitch}} \end{bmatrix} \begin{bmatrix} 1 \end{bmatrix} \Big), \end{aligned} \tag{3.7}$$

where $a_2 = -a_{\theta_2}$, $a_3 = -a_{\theta_1}$, $\lambda_2 = a_{\theta_3}$ and $\theta_{\text{bias, pitch}} = d_{\theta_2}$, and the pair $(\boldsymbol{A}, \boldsymbol{B}\boldsymbol{\Lambda})$ is controllable since the matrix $[\boldsymbol{B}\boldsymbol{\Lambda} \;\; \boldsymbol{A}\boldsymbol{B}\boldsymbol{\Lambda}]$ is of full rank.

The regressor, $\boldsymbol{\Phi}(\boldsymbol{x})$, and the control input matrix, $\boldsymbol{B}$, enter the controller equations through the adaptive law in equation (3.2). However, the system matrix, $\boldsymbol{A}$ is not present in the implementation of the controller. Consequently, the control designer cannot provide a-priori knowledge about the linear terms of the plant model to the MRAC scheme.

The bias terms in equations (3.4) and (3.7) act as a steady state compensation, similar to an integral term in a PID controller. The effect of the addition of the bias terms, to the otherwise linear model, is shown in figure 3.1a. Similarly, the

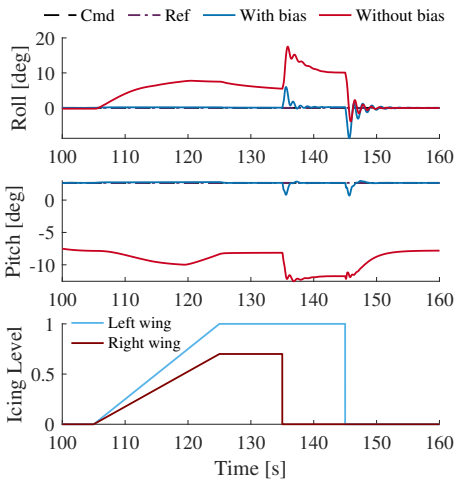

(a) The adaptive controller with and without bias term.

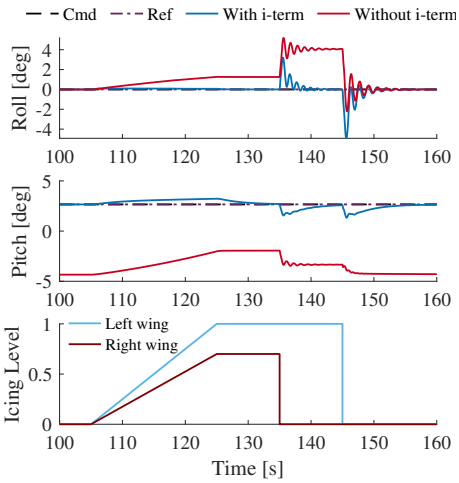

(b) The PID controller with and without integral term.

addition of an integral term to a PID controller is shown in figure 3.1b [1]. The figures 3.1a and 3.1b show that the bias and integral term in roll, respectively, play a critical, and similar, role in compensating for the changed roll dynamics caused by the icing. Additionally, they both provide a necessary steady state compensation in pitch.

3.1.2 Reference model

The reference models for the roll and pitch dynamics are chosen as second order transfer functions, given in equations (3.8) and (3.9), where $\omega_{n,i}$ is the natural frequency and ζ_i is the damping factor.

$$\frac{\phi_{\text{ref}}}{\phi_{\text{cmd}}}(s) = \frac{\omega_{n,\phi}^2}{s^2 + 2\zeta_\phi \omega_{n,\phi} s + \omega_{n,\phi}^2} \tag{3.8}$$

$$\frac{\theta_{\text{ref}}}{\theta_{\text{cmd}}}(s) = \frac{\omega_{n,\theta}^2}{s^2 + 2\zeta_\theta \omega_{n,\theta} s + \omega_{n,\theta}^2} \tag{3.9}$$

The reference models describe the desired behavior of the roll and pitch dynamics given the commanded angle, ϕ_{cmd} and θ_{cmd}.

[1] Note that the figures are meant to illustrate the effect and similarities of adding a bias and integral term, respectively. The tuning of the controllers in the case with and without bias and integral term is identical.

3.2 PID controllers

The PID controller structure is based on the control design presented by Beard & McLain in [17] and described in section 2.3.3. Both the roll and pitch loop consist of a controller with a proportional, integral and derivative term. This deviates with the pitch controller presented in [17], where the inner control loop in pitch does not include an integral term. This design choice of Beard & McLain [17] is to avoid limiting the bandwidth of the inner loop, based on the assumption that outer loop controllers will compensate for the steady state offset in pitch. In this thesis a key aspect is comparing the inner loop controllers of the MRAC and PID controllers. As such, an integral term in the pitch control loop is added to compensate for a steady state offset in pitch.

Further, for easier comparison of the MRAC and PID controller, the PID controllers are set to follow the output of the reference models described in section 3.1.2. This is in contrast to using the commanded angle as reference to the controller. This limits the speed of the PID controller to the speed of the reference model. However, the reference model facilitates for the calculation of less aggressive control inputs by the PID controller.

To prevent the integrators from winding up if the control surfaces saturate, the PID controllers are implemented with anti-windup mechanisms.

3.3 Tuning

The tuning process in this thesis is based on systematic trial-and-error. The simulation environment consists of alternating square references in roll and pitch, combined with an asymmetric icing scenario. The airspeed reference is constant at $V_a = 20\text{m/s}$. A set of tuning values for a given tuning parameter is simulated, and the response with each value is plotted. The assessment of each tuning is done by a qualitative evaluation of the plots and a quantitative comparison of the integral of the absolute error (IAE) performance metric (see chapter 5) for each set of tuning values. The qualitative evaluation is based on reducing undesired oscillations and favoring less aggressive control inputs. If there is not a significant difference in the qualitative behavior, the choice of tuning value is taken based on the value of the performance metric.

3.3.1 Tuning of MRAC scheme

Before tuning the adaptive rates for the MRAC scheme, an observation is made. The solution, $\boldsymbol{P}$, to the Lyapunov equation in equation (2.23) is included in

each of the adaptive laws in equation (3.2). Since the solution is given by

$$\boldsymbol{P} = \begin{bmatrix} \frac{q_2\omega_n^2+q_1+4q_1\zeta^2}{4\omega_n\zeta} & \frac{q_1}{2\omega_n^2} \\ \frac{q_1}{2\omega_n^2} & \frac{q_2\omega_n^2+q_1}{(q_2\omega_n^2+q_1)/(4\omega_n^3\zeta)} \end{bmatrix}, \tag{3.10}$$

where $\boldsymbol{Q}$ is chosen as

$$\boldsymbol{Q} = \begin{bmatrix} q_1 & 0 \\ 0 & q_2 \end{bmatrix},$$

and $\boldsymbol{A}_{\text{ref}}$ is given by

$$\boldsymbol{A}_{\text{ref}} = \begin{bmatrix} 0 & 1 \\ -\omega_n^2 & -2\zeta\omega_n \end{bmatrix},$$

the reference model and the choice of $\boldsymbol{Q}$ will affect all adaptations, $\hat{\boldsymbol{K}}_x$, $\hat{\boldsymbol{K}}_r$ and $\hat{\boldsymbol{\Theta}}$. Therefore, the choice of reference model and tuning $\boldsymbol{Q}$ is done before tuning the adaptive rates. The reference model parameters in equations (3.8) and (3.9) are chosen as $\omega_{n,\phi} = \omega_{n,\theta} = 4$ and $\zeta_\phi = \zeta_\theta = 1$.

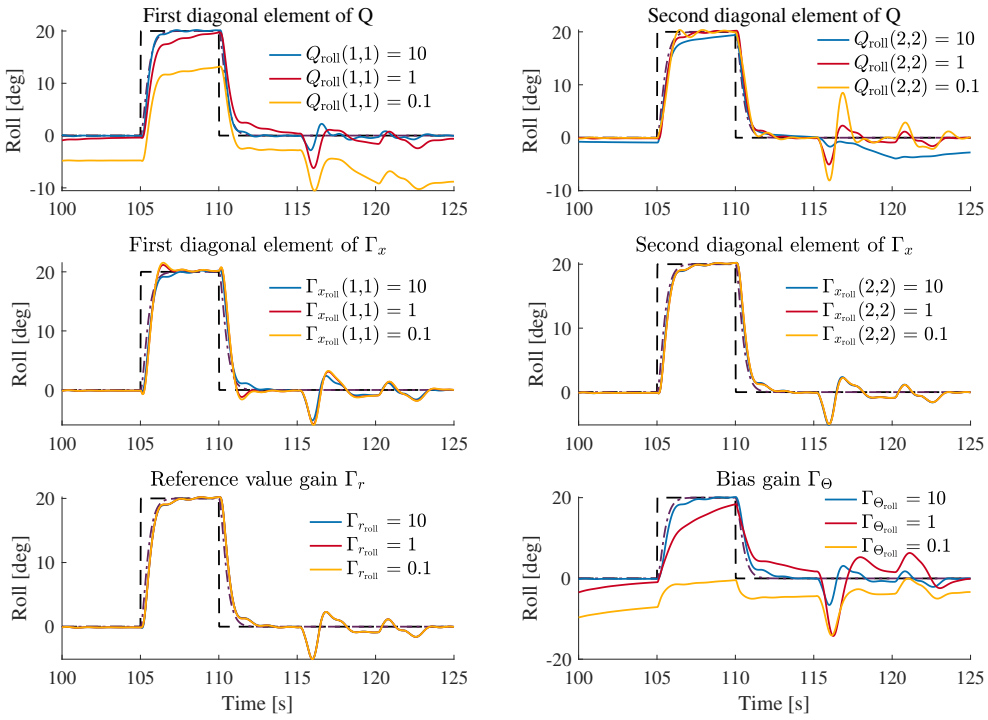

Figure 3.2: The effect of each of the adaptive rates with the roll controller. From $t = 115$s to $t = 120$s the pitch reference (not shown) is set to 20°. The icing level is set to $(\zeta_{\text{left}}, \zeta_{\text{right}}) = (0.8,\ 0.3)$.

Figures 3.2 and 3.3 show a simple test run to illustrate how each adaptive rate affects the response of the systems. In each sub-figure a simulation is run with one adaptive rate set to the values $\{10, 1, 0.1\}$, while the other rates are constant. The adaptive rate in question for each sub-figure is given by the

legend and title. The conditions of the test run is equal in every simulation in the figures 3.2 and 3.3 where the roll reference is set to 20° for $t \in (105, 110)$s, followed by a 20° pitch reference $t \in (115, 120)$s. The icing level is constant with $(\zeta_{\text{left}}, \zeta_{\text{right}}) = (0.8,\ 0.3)$.

From the figures 3.2 and 3.3, some anecdotal observations regarding the tuning variables can be made. Firstly, the value of the first diagonal element of the $\boldsymbol{Q}$-matrix, q_1, is seen to have a significant impact on the tracking performance for both the roll and pitch controllers. This is expected as q_1 is present in every element of $\boldsymbol{P}$ given in equation (3.10), wherein $\boldsymbol{P}$ is present in each of the adaptive laws in equation (3.2). Secondly, the adaptive rates $\boldsymbol{\Gamma}_x$ and $\boldsymbol{\Gamma}_r$

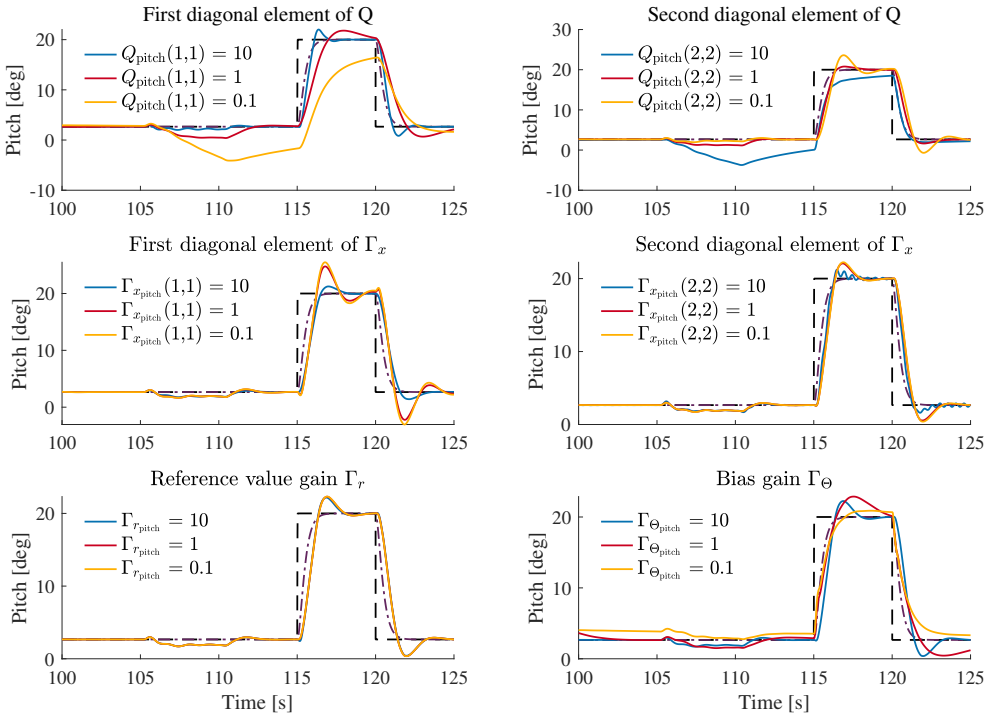

Figure 3.3: The effect of each of the adaptive rates with the pitch controller. From $t = 105$s to $t = 110$s the roll reference (not shown) is set to 20°. The icing level is set to $(\zeta_{\text{left}}, \zeta_{\text{right}}) = (0.8,\ 0.3)$.

have a much less impact on the response of both the roll and pitch controller. Figure 3.3 shows, however, that an increase in the second element of $\boldsymbol{\Gamma}_x$ of the pitch controller leads to oscillations. With more aggressive pitch references and with increased asymmetry of the icing levels, these oscillations become more pronounced. As such, this gain value was chosen to be quite low.

Finally, figure 3.2 shows that the adaptive rate of the bias term in roll has a significant impact on the tracking performance. As mentioned in section 3.1.1, the bias term likely compensates for the additional roll moment produced by

asymmetric icing levels, and thus plays a critical role in the tracking performance.

Overall, to avoid oscillations in the system states, the adaptive rates were chosen as small as possible. Sometimes this comes at the cost of reduced tracking performance. However, avoiding oscillations in untested environments, such as wind conditions, severe icing conditions and aggressive reference inputs, was prioritized. The final tuning of the adaptive rates is given in table 3.1.

Table 3.1: The adaptive rates of the MRAC scheme.

Roll adaptive rates		**Pitch adaptive rates**	
Parameter	Value	Parameter	Value
$\boldsymbol{Q}$	$\begin{bmatrix} 3 & 0 \\ 0 & 1 \end{bmatrix}$	$\boldsymbol{Q}$	$\begin{bmatrix} 4 & 0 \\ 0 & 0.4 \end{bmatrix}$
$\boldsymbol{\Gamma}_x$	$\begin{bmatrix} 12 & 0 \\ 0 & 4 \end{bmatrix}$	$\boldsymbol{\Gamma}_x$	$\begin{bmatrix} 6 & 0 \\ 0 & 0.01 \end{bmatrix}$
$\boldsymbol{\Gamma}_r$	10	$\boldsymbol{\Gamma}_r$	5
$\boldsymbol{\Gamma}_\Theta$	15	$\boldsymbol{\Gamma}_\Theta$	10

3.3.2 Tuning of PID controller

The tuning of the PID controller follows the procedure described in Beard & McLain [17]. The procedure is outlined below.

Roll loop tuning

Firstly, a second-order transfer function describing the desired response in roll is defined as

$$\frac{\phi}{\phi_{\text{cmd}}}(s) = \frac{\omega_{n_\phi}^2}{s^2 + 2\zeta_\phi \omega_{n_\phi} s + \omega_{n_\phi}^2}.$$

This gives the proportional gain of the roll loop as

$$k_{p_\phi} = \frac{\delta_a^{\max}}{e_\phi^{\max}} \text{sign}(a_{\phi_2}),$$

where $\delta_a^{\max}$ is the maximum aileron deflection, $e_\phi^{\max}$ is a design parameter such that the ailerons saturate when the roll error is $e_\phi^{\max}$. The term a_{ϕ_2} is from the linear transfer function model in roll found by [17] and is given by

$$a_{\phi_2} = \frac{1}{2}\rho V_a S b C_{p_{\delta_a}},$$

where ρ is the air density, V_a is the airspeed, S is the wing area, b is the wing span and $C_{p_{\delta_a}}$ is defined by Beard & McLain [17] as $C_{p_{\delta_a}} = \Gamma_3 C_{l_{\delta_a}} + \Gamma_4 C_{n_{\delta_a}}$, where $\Gamma_3 = I_z/(I_x I_z - I_{xz}^2)$ and $\Gamma_4 = I_{xz}/(I_x I_z - I_{xz}^2)$.

The derivative gain of the roll loop is given as

$$k_{d_\phi} = \frac{2\zeta_\phi \omega_{n_\phi} - a_{\phi_1}}{a_{\phi_2}},$$

where the damping ratio ζ_ϕ is a design parameter and ω_{n_ϕ} is the natural frequency of the roll loop given by

$$\omega_{n_\phi} = \sqrt{|a_{\phi_2}| \frac{\delta_a^{\max}}{e_\phi^{\max}}}.$$

The term a_{ϕ_1} is given by

$$a_{\phi_1} = -\frac{1}{2}\rho V_a S b C_{p_p} \frac{b}{2V_a},$$

where C_{p_p} is defined by [17] as $C_{p_p} = \Gamma_3 C_{l_p} + \Gamma_4 C_{n_p}$.

Setting $\delta_a^{\max} = 30^\circ$ and choosing $e_\phi^{\max} = 10^\circ$ and $\zeta_\phi = 1$, gives $k_{p_\phi} = 3$ and $k_{d_\phi} = 0.09$. The integral term is found through trial and error by simulating the system under the tuning environment described in section 3.3. With some adjustments, the final tuning values are given in table 3.2.

Pitch loop tuning

The desired response for the pitch loop is given by the second-order transfer function

$$\frac{\theta}{\theta_{\text{cmd}}}(s) = \frac{K_{\theta_{\text{DC}}} \omega_{n_\theta}^2}{s^2 + 2\zeta_\theta \omega_{n_\theta} s + \omega_{n_\theta}^2},$$

where $K_{\theta_{\text{DC}}}$ is the DC gain of the pitch loop. The proportional gain is given as

$$k_{p_\theta} = \frac{\delta_e^{\max}}{e_\theta^{\max}} \text{sign}(a_{\theta_3}),$$

where $\delta_e^{\max}$ is the maximum elevator deflection, $e_\theta^{\max}$ is a design parameter such that the elevators saturate when the roll error is $e_\theta^{\max}$.

The derivative gain of the pitch loop is given as

$$k_{d_\theta} = \frac{2\zeta_\theta \omega_{n_\theta} - a_{\theta_1}}{a_{\theta_3}},$$

where

$$\omega_{n_\theta} = \sqrt{a_{\theta_2} + \frac{\delta_e^{\max}}{e_\theta^{\max}}|a_{\theta_3}|}.$$

Similarly to a_{ϕ_1} and a_{ϕ_2} in the roll loop, a_{θ_1}, a_{θ_2} and a_{θ_3} are the coefficients in the linear transfer function models of the pitch dynamics found by Beard & McLain in [17]. The coefficients are defined as

$$a_{\theta_1} = -\frac{\rho V_a^2 cS}{2I_y} C_{m_q} \frac{c}{2V_a},$$
$$a_{\theta_2} = -\frac{\rho V_a^2 cS}{2I_y} C_{m_\alpha},$$
$$a_{\theta_3} = \frac{\rho V_a^2 cS}{2I_y} C_{m_{\delta_e}},$$

where c is the mean chord.

Setting $\delta_e^{\max} = 30^\circ$ and choosing $e_\theta^{\max} = 20^\circ$ and $\zeta_\theta = 1$, gives $k_{p_\theta} = -1.5$ and $k_{d_\theta} = -0.174$. The integral term is found through trial and error by simulating the system under the tuning environment described in section 3.3. The negative gain values in the pitch loop are a result of the negative sign of a_{θ_3} which follows from $C_{m_{\delta_e}}$ being negative. With some adjustments, the final tuning values are given in table 3.2.

Table 3.2: The tuning parameters of the roll and pitch PID controllers.

Roll controller gains		**Pitch controller gains**	
Parameter	Value	Parameter	Value
k_{p_ϕ}	2.5	k_{p_θ}	-1
k_{i_ϕ}	2	k_{i_θ}	-0.1
k_{d_ϕ}	0.01	k_{d_θ}	-0.25

A complete overview of all parameters and tuning values is given in appendix A.

3.4 Guidance

The guidance control scheme is implemented with the airspeed controller and the longitudinal and lateral guidance laws described in section 2.4. The tuning values of the guidance scheme is given in table A.3.

Chapter 4

Simulation

In this chapter, the simulator model and icing model for the simulating the system is described. Additionally, the simulation cases for testing the controllers described in chapter 3 are presented.

4.1 Simulator model

To test the developed controllers, MATLAB/Simulink is used to simulate the system. The simulator is extended from the Simulink model developed by Gryte in [20] to include the effects of asymmetric icing and add the aerodynamic model by Winter [14]. Previously, a Python simulator [28] has also been developed by Kleiven in [6]. The simulator model is implemented based on the mathematical model described in section 2.1, with the configuration and aerodynamic data of the Skywalker X8 fixed wing aircraft. A complete overview of all parameters and tuning values is given in appendix A.

A block diagram of the simulator structure is shown in figure 4.1, with a description of the different components given below.

Actuators The actuator block is intended to simulate the physical actuators of the UAV with its static and dynamic limitations. That is, the limits of the physical positions the actuator can reach and how fast the actuator can reach the demanded position. The static limitation is simulated by saturating the demanded control input by a specified largest allowed actuator position. Whereas the dynamic limitation is simulated by feeding the control

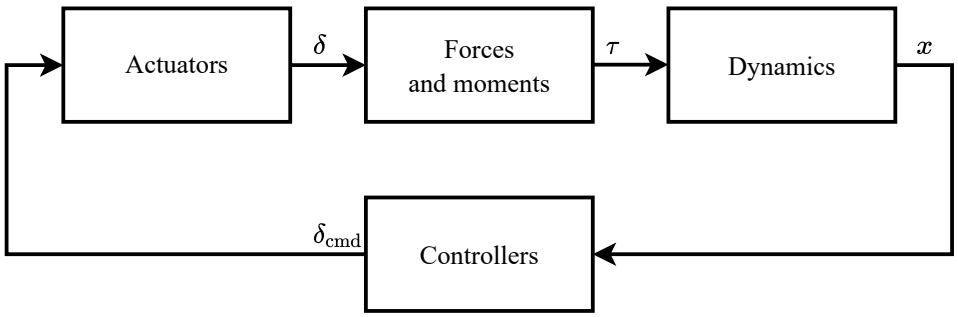

Figure 4.1: Block diagram of the MATLAB simulator structure for the UAV.

input through a second-order filter, given by

$$\frac{\delta_{\text{actual}}}{\delta_{\text{demanded}}} = \frac{\omega_0^2}{s^2 + 2\zeta\omega_0 s + \omega_0^2}.$$

Note that the demanded elevator and aileron inputs are mapped to the left and right elevon by the relation in 2.5 before the rate limiting and saturating of the inputs. The elevons are then mapped to elevator and aileron before leaving the actuator block.

Forces and moments The forces block calculates the forces and moments acting on the UAV described in section 2.2. That is, the aerodynamic, gravitational and propulsion forces and moments.

Dynamics The dynamics block calculates the dynamics of the UAV given the forces and moments calculated in the previously described forces block.

Controllers The controllers block consists of the controllers for the UAV. Given the current state, the controllers find a demanded control input which is fed to the actuator block, described earlier.

4.2 Icing model

The icing model implemented in the simulator is based on the extension to an asymmetric model by Kleiven [6] and the modelling work done by Winter [14], which provides the aerodynamic coefficients for the clean (no icing) case and the iced case. The icing data from Winter [14] is found for the mixed icing case, the most severe icing type of the three types, glaze, rime and mixed, with

respect to aerodynamic performance. The aerodynamic coefficient data from Winter is provided for a given angle of attack and sideslip, for the longitudinal and lateral coefficients, respectively. The coefficients are interpolated by the Simulink block `n-D Lookup Table` [29] for a given angle of attack or sideslip. Following the notation of Kleiven in [6], the variable $\zeta \in [0, 1]$ is used to describe the level of icing. For the clean case $\zeta = 0$ and for the iced case $\zeta = 1$. The final value for the aerodynamic coefficient is found by linear interpolation as

$$C_k(\zeta) = \zeta \, C_{k,\text{iced}} + (1 - \zeta) \, C_{k,\text{clean}}.$$

4.2.1 Reduced control surface effectiveness

As described in section 2.5.1, icing on the airfoil can result in a decrease of the control surface effectiveness. Through computational fluid dynamics (CFD) simulations, described in the appendix of the paper in appendix C, an estimate of the reduced control surface effectiveness due to icing on the airfoil is found.

The results of the analysis show that the value of the aerodynamic coefficients $C_{L_{\delta_e}}$ and $C_{l_{\delta_a}}$ are reduced by 27% from the clean to iced case, $C_{D_{\delta_e}}$ and $C_{n_{\delta_a}}$ are increased by 86%, and $C_{m_{\delta_e}}$ is reduced by 37%. The reduced control surface effectiveness is implemented in the simulator model by multiplying the aerodynamics coefficients for the iced case by the corresponding percentage-wise increase or decrease given above.

Additionally, the analysis in appendix C show that the stall limit is decreased by 11° from the clean to iced case, where the limit is given by $\alpha_{\text{stall}} = -0.1\delta + 15°$ for the clean airfoil and $\alpha_{\text{stall}} = -0.1\delta + 4°$ for the iced airfoil, where the stall limit depends on the control surface deflection, δ. It is noted that the CFD analysis is only used to determine the reduction in control effectiveness due to icing, while the rest of the model is the same as in Kleiven [6].

4.3 Wind conditions

For simulating wind gusts, the `Dryden Wind Turbulence Model` [26] Simulink block is used, where the theory behind the Dryden wind model is described in section 2.5.2. The Simulink block uses a random noise seed provided by the user to generate the turbulence signals. To ensure consistency across the simulations the same seed is used for each simulation.

The steady state component of the wind is simulated with the `Horizontal Wind Model` [30] Simulink block. The modelling of the steady wind component

is described in section 2.5.2.

4.4 Limitations of the simulator

As with any model, the simulator model will not accurately describe every aspect of the system. In this section, the main limitations and inaccuracies of the simulator model are mentioned.

Firstly, the model does not include stalling of the aircraft. As a consequence of this, every test run must be evaluated after running a simulation by verifying that the angle of attack is within the stall limit. For the simulation results in this thesis, $\alpha_{\text{stall}} \approx 10^\circ$ is used as a guideline.

Secondly, the simulator will interpolate past the aerodynamic coefficient data that is available. That is, the interpolation of the aerodynamic coefficients described in section 4.2 may not reflect the realistic behavior when the data is interpolated beyond the available data points. An example of this is seen in figure 4.2. Thus, to mitigate this limitation the angle of attack should be reviewed after every simulation, to ensure that the angle of attack is within the limits of realistic behavior with respect to the aerodynamic coefficients.

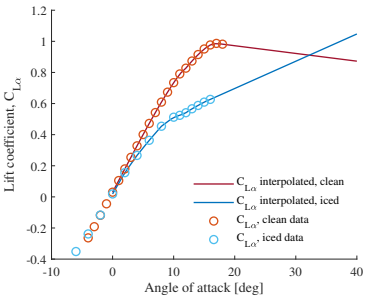

Figure 4.2: Lift coefficient data from the system identification and resulting interpolated data.

Lastly, the system identification work with mixed ice done by Winter in [14], is considered to be a worst-worst case of icing. As such, it reflects a less common scenario of icing than experienced in most icing conditions.

However, the simulator model is believed to give an adequate reflection of the dynamics of ice accretion and shedding for the purpose of investigating the effects of icing on the aircraft.

4.5 Excitation of the adaptive controllers

Prior to each test run, the adaptive controllers are excited by the sinusoidal signals given by

$$r_\varepsilon(t) = 25^\circ \sin(0.5t) + 20^\circ \sin(0.2t) + 10^\circ \sin(0.1t) + 5^\circ \sin(3t), \tag{4.1}$$

and

$$r_\varepsilon(t) = 10^\circ \sin(t) + 6^\circ \sin(0.6t) + 2^\circ \sin(0.1t) + 2^\circ \sin(3t), \tag{4.2}$$

for the roll and pitch controller, respectively, to ensure that its internal states and parameters have converged to a suitable tuning before the icing events. The excitation is run for 50 seconds with the icing level set to $\zeta = 0$.

4.6 Simulation cases

In this section, the simulation cases are presented. The focus of this thesis has been the development of inner loop control for the roll and pitch angle of the UAV during icing conditions. The choice of simulation cases has therefore been focused on choosing roll and pitch references, and pairing them with an icing level that explores the capabilities of the controllers.

4.6.1 Baseline, reduced airspeed and wind conditions

The simulation cases can be divided into four groups. The first group consists of three test runs with an initial baseline case, a case with reduced airspeed and a case simulated with wind gusts. Common to the simulations in this grouping is the roll and pitch reference shown in figure 4.3.

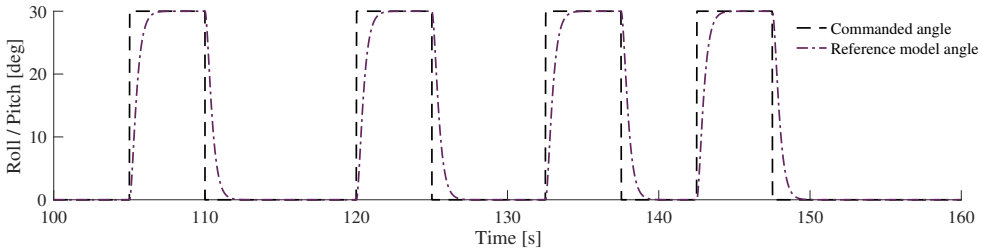

Figure 4.3: Roll and pitch reference for the first grouping of simulations.

The baseline case is chosen to represent a case where the reference values in roll and pitch are slightly aggressive, but still within the limits of what the controllers can handle under "normal" conditions. That is, when the airspeed is set to the speed the controllers were tuned with, and the UAV is not exposed to wind disturbances. Then the conditions are changed to include a reduced airspeed case and a simulation case with wind gusts, where the response is compared to the baseline case. The icing timeseries accompanying these cases is described in section 4.6.5.

4.6.2 Reduced control surface effectiveness

For the second group, reduced control surface effectiveness, described in section 4.2.1, is simulated. This test run is performed with a similar reference to the first group, however the angle reference is increased from 30° to 50° for the pitch case and from 30° to 40° for the roll case. The reference angle is increased such that the reduced control effectiveness case is simulated for a case that is closer to the limits of the controllers. Wherein this limit is determined by the maximum reference angle where the angle of attack is within the stall limit.

The simulation case is run with the reduction in control surface effectiveness given by the CFD simulation data described in section 4.2.1, labelled "Reduction 1" in the simulation results in section 6.4. Additionally, a simulation with an even further reduction in the control surface effectiveness is run, labelled "Reduction 2". The values for the simulations are given in table 4.1.

Table 4.1: Values for reduced control surface effectiveness simulation case

Coefficient	**Percent-wise change**	
	Reduction 1	Reduction 2
$C_{L_{\delta_e}}$	- 27%	- 50%
$C_{D_{\delta_e}}$	+ 86%	+ 150%
$C_{m_{\delta_e}}$	- 37%	- 50%
$C_{l_{\delta_a}}$	- 27%	- 50%
$C_{n_{\delta_a}}$	+ 86%	+ 150%

4.6.3 Guidance

The third grouping is a single path following simulation case simulated with wind gusts and a steady wind component with $V_w = 10\text{m/s}$ and $\psi_w = 90°$. The path consists of waypoints seen in figure 4.4, that form a square zig-zag pattern in the xy-plane, and also includes changes in the altitude as the UAV traverses the zig-zag path. The guidance case can be thought of as a case where the UAV is conducting a survey of the land at the foot of a mountain.

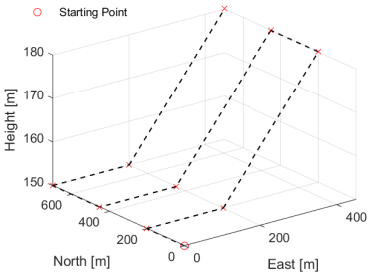

Figure 4.4: The path of the guidance case made up from ten waypoints.

4.6.4 Bias and integral terms

The final and fourth group of simulation cases explores the bias terms of the adaptive controller and the integral terms of the PID controller. This simulation case is intended to investigate whether the bias or integral terms of the controllers can capture the effects of icing in any meaningful sense. The icing timeseries for this case is described in section 4.6.5.

4.6.5 Icing timeseries

For the simulation cases in sections 4.6.1 and 4.6.4 the accompanying icing timeseries is described in this section. For the guidance case section 4.6.3, the icing timeseries is qualitatively the same, however the time scale of the icing is modified.

The icing timeseries can be described as having five phases, as seen in figure 4.5. Firstly, there is no icing on either wing, followed by a ramp up to an icing level of $\zeta_{\text{left}} = 1$ for the left wing and $\zeta_{\text{right}} = 0.7$ for the right wing. The icing level is then constant at these slightly asymmetric icing levels, until de-icing of the right wing is performed. The following phase after de-icing consists of a 100% asymmetry in the icing levels of the wings, until, finally, the left wing is also de-iced.

The most severe phase with respect to tracking performance is expected to be the phase from de-icing of the first wing until de-icing of the second wing. The de-icing will cause a sudden change in the dynamics and the time in between de-icing will consist of significant asymmetry of the wings' characteristics.

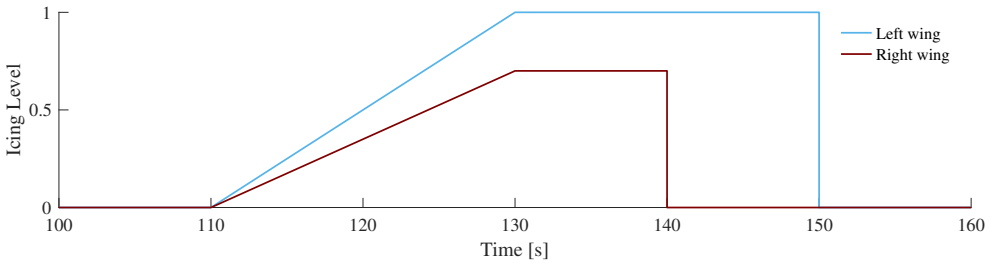

Figure 4.5: Icing timeseries.

It should be noted that the ice accretion in the icing timeseries in figure 4.5 is much faster than what is realistic. [31] suggests that the duration of ice accretion on the wings to form icing with a horn shaped structure, as is the case with mixed ice, is in the range of 20-40 minutes. However, this choice is taken to keep the simulations short for the purpose of easier presentation and evaluation of the resulting plots of the response. This raises a valid concern for

how the choice of a faster ice accretion sequence will influence the evaluation of the adaptive control scheme, as the controllers will have a shorter time to adapt to the change in icing levels. However, the faster ice accretion is not expected to unfairly penalize the adaptive controller, as it is tuned quite fast to be able to respond to the sudden de-icing of the wings.

Chapter 5

Performance Metric

In order to assess the quality of the performance in a more quantitative measure, in contrast to the qualitative measure of studying the resulting graphs, a performance metric is used.

The integral of the absolute value of the error (IAE) gives a measure of the cumulative tracking error and is defined as

$$\text{IAE} = \int |e(\tau)| \, d\tau,$$

where the error, $e(t)$, is the tracking error with respect to the reference model angle. Which gives $e(t) = \phi - \phi_{\text{ref}}$ and $e(t) = \theta - \theta_{\text{ref}}$ for the roll and pitch angle errors, respectively.

The value of the IAE metric will vary significantly depending on the duration and the simulated scenario of a given time series. Therefore, the point of interest is the relative value of the metric across similar scenarios.

Part III

Results, Discussion and Conclusion

Chapter 6

Simulation results

This section presents the simulation results for the simulation cases presented in section 4.6. The performance metric described in chapter 5 is used to give a quantitative measure of the tracking performance of the controllers, while plots provide a qualitative description of the response.

As mentioned in section 4.6.1, the roll and pitch references, in addition to the icing timeseries and the duration of the simulations, are kept the same across the first group of simulation cases for easier comparison.

6.1 Baseline

Figures 6.1 and 6.2 show the response of the baseline simulations case described in section 4.6. The simulation case is referred to as a baseline case as it sets a baseline for the following two simulations where the airspeed is decreased and where wind gusts are added to the simulations.

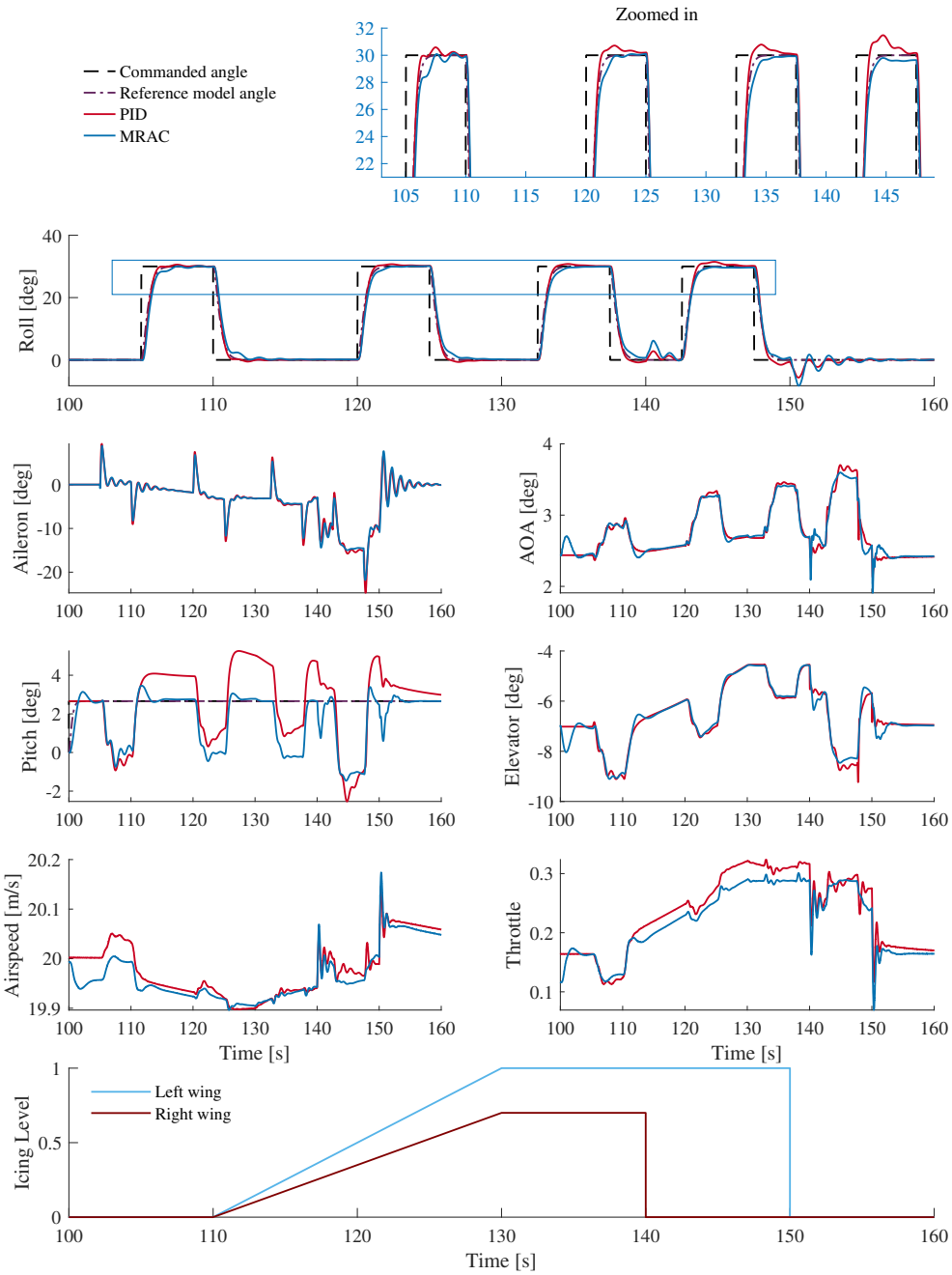

Figure 6.1: Baseline simulation case with square reference signal in roll. The response with the adaptive controller and the PID controller is shown.

The first baseline simulation case in figure 6.1, is run with a square 30° reference signal in roll and a constant angle in pitch at the pitch trim angle, $\theta_{\text{trim}} = 2.66°$. The figure shows the response with the adaptive MRAC control scheme and the PID controller. Figure 6.1 shows an increase in throttle for both controllers as icing levels increase, which is consistent with increased drag due to icing as

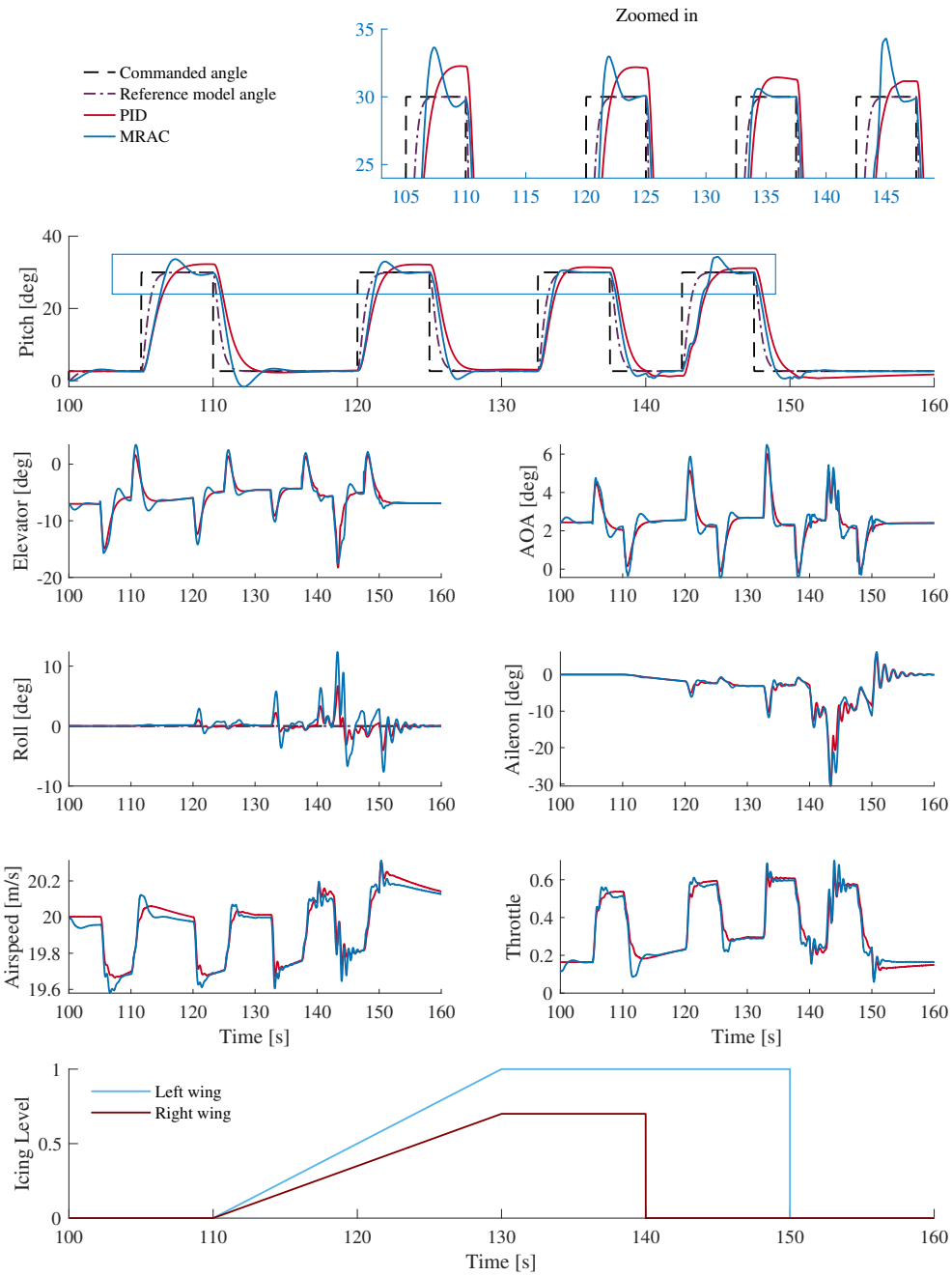

Figure 6.2: Baseline simulation case with square reference signal in pitch. The response with the adaptive controller and the PID controller is shown.

described in section 2.5.1.

The maximum angle of attack during the simulation with the adaptive controller is $\alpha = 3.6°$, and $\alpha = 3.7°$ with the PID controller, both at $t \approx 145$s.

The second baseline simulation case in figure 6.2, is run with a square 30° reference signal in pitch and a constant angle in roll at the roll trim angle, $\phi_{\text{trim}} = 0°$.

The maximum angle of attack during the simulation with the adaptive controller is $\alpha = 6.5°$, and $\alpha = 6.0°$ with the PID controller, both at $t \approx 133$s. With both controllers, the angle of attack goes slightly below zero degrees. The minimum angle of attack with the adaptive controller is at $t \approx 125$s, with $\alpha = -0.4°$. With the PID controller, the minimum angle of attack occurs at $t \approx 138$s with $\alpha = -0.2°$. Additionally, the angle of attack increases in both figures 6.1 and 6.2 with increased icing levels.

As the icing levels increase, and in the 100% asymmetric icing level phase from $t = 140$s to $t = 150$s, the roll angle tracking performance with both controllers is worsened. The roll angle reaches a maximum deviation from its zero-degree reference at $t \approx 143$s of $e_\phi = 12.4°$ with the adaptive controller. With the PID controller the maximum deviation is $e_\phi = 6.7°$ at $t \approx 143$s.

Figure 6.2, also shows how the airspeed and pitch dynamics are closely connected, as the deviations from the 20m/s reference in airspeed coincide with the pitch angle deflections.

6.2 Reduced airspeed

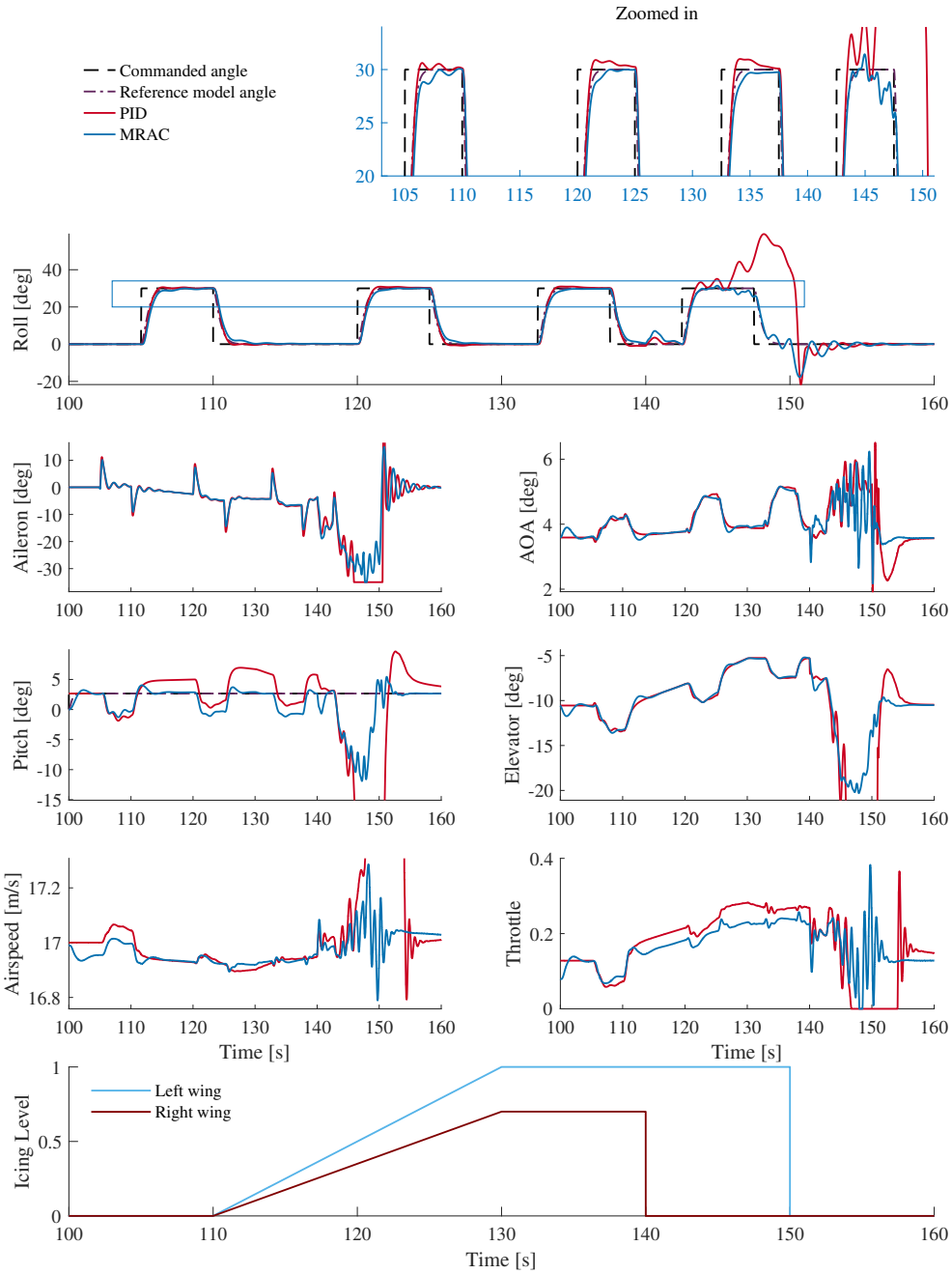

Figure 6.3: Reduced airspeed, $V_a = 17$m/s, simulation case with square reference signal in roll. The response with the adaptive controller and the PID controller is shown.

Figure 6.3 shows the response with the adaptive controller and the PID con-

troller for the baseline case in figure 6.1 with the airspeed decreased from 20 m/s to 17 m/s. For the most severe icing phase from $t = 140$s to $t = 150$s when the icing is 100% asymmetrical, the PID controller is not able to follow the roll reference. The roll angle reaches a maximum of 59° at $t \approx 148$s. The maximum deviations from the pitch reference and the airspeed reference are not seen in figure 6.3. The pitch angle goes down to $-51°$ at $t \approx 149$s, and a maximum airspeed of $V_a = 24.4$m/s is reached. Both the aileron and elevator saturate.

Figure 6.3 shows that the adaptive controller is also affected by the reduced airspeed during the most severe icing phase of 100% asymmetric icing from $t = 140$s to $t = 150$s. However, the degradation in the tracking performance is not as severe as with the PID controller. The response of the adaptive controller for an increased roll reference from $\phi_{\text{cmd}} = 30°$ to $\phi_{\text{cmd}} = 40°$ is shown in figure B.1, where the response with the adaptive controller is closer to that of the PID controller in figure 6.3.

Figure 6.4 shows the time evolution of the IAE performance metric (see chapter 5) for the adaptive controller and the PID controller. The figure shows the IAE metric for the baseline simulation case in figure 6.1 with airspeed $V_a = 20$m/s and for the reduced airspeed case in figure 6.3 with $V_a = 17$m/s. Figure 6.4 shows that the tracking performance with the PID controller is superior than the adaptive controller in roll up until the degradation in the tracking performance at $t \approx 145$s. For the tracking performance in pitch, the opposite is true. The adaptive controller has a better tracking performance than the PID controller. Common to both is that the tracking performance is worse with the reduction in airspeed.

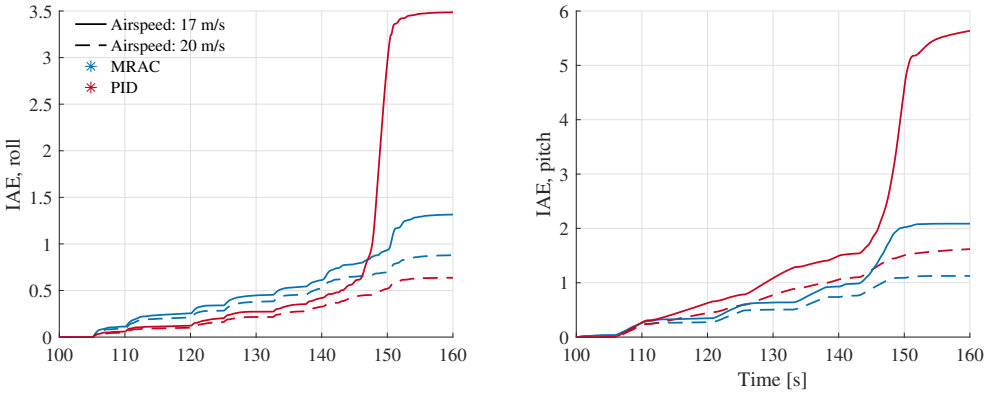

Figure 6.4: Time evolution of the integral of the absolute value of the tracking error (IAE) for the response shown in figure 6.3. The IAE metric is shown for both controllers, indicated by the two separate colors.

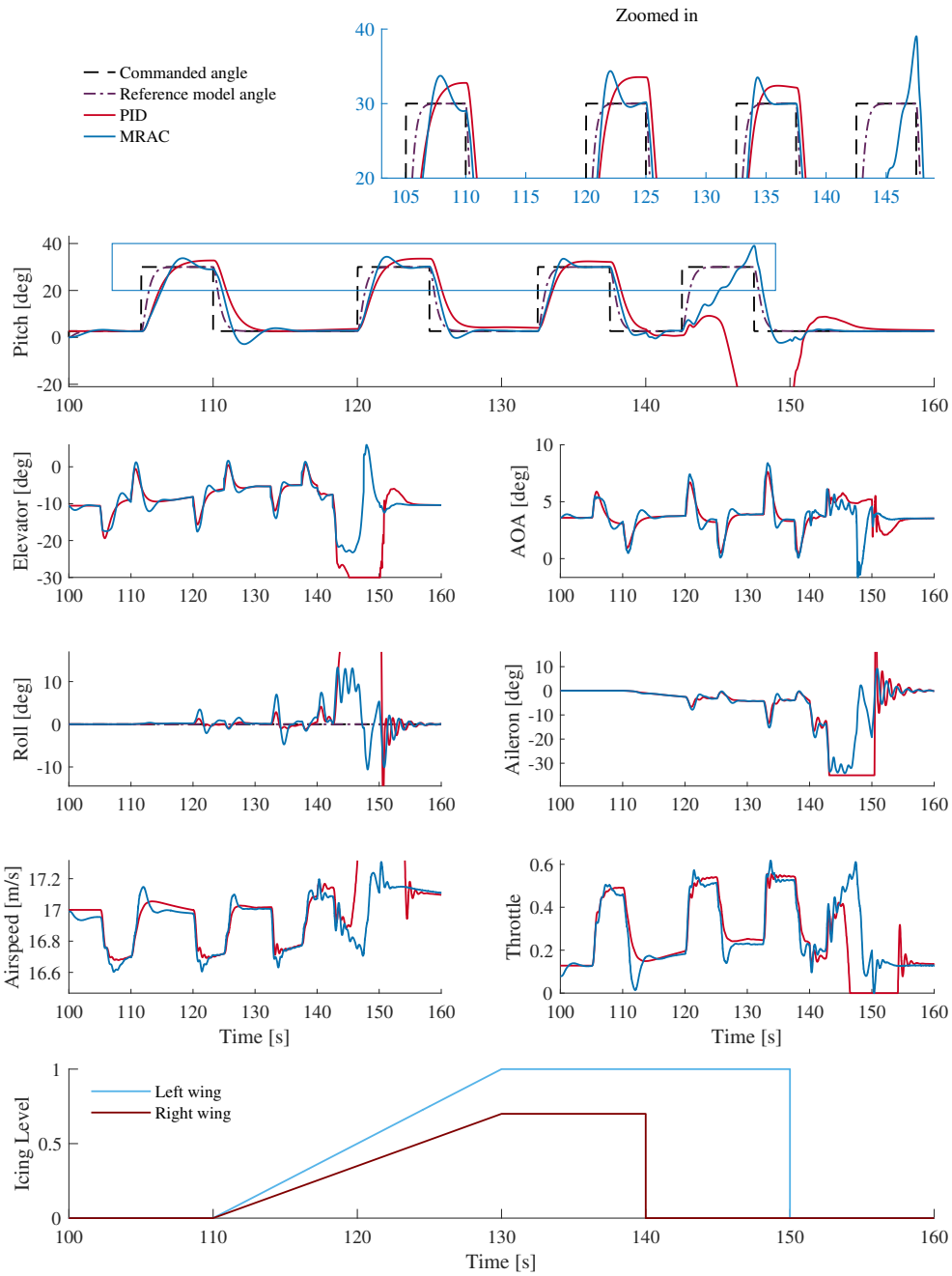

Figure 6.5: Reduced airspeed, $V_a = 17$m/s, simulation case with square reference signal in pitch. The response of the adaptive controller and the PID controller is shown.

Figure 6.5 shows the response of the adaptive controller and the PID controller for the baseline case in figure 6.2 with the airspeed decreased from 20 m/s to 17 m/s. Note that this simulation case differs from the previous in that the square reference signal is now in the pitch angle, not the roll angle. During the most

severe icing phase with 100% asymmetric icing from $t = 140$s to $t = 150$s, the tracking performance with both the adaptive controller and the PID controller is significantly reduced. The tracking performance with the PID controller has the largest decline. The values of the response not shown in figure 6.5 is a maximum airspeed of $V_a = 25.3$m/s, maximum roll angle of $\phi = 79.3°$ and a pitch angle down to $\theta = -62.7°$, at $t \in (147, 150)$s. Additionally, the elevator and aileron saturate at $t \approx 145$s.

The adaptive controller has a maximum deviation from the reference in roll of $e_\phi = 13.3°$ at $t \approx 143$s. Additionally, the pitch angle overshoots the final 30° pitch reference by 9° at $t \approx 143$s. The angle of attack drops down below 0° to $-1.7°$ with the adaptive controller. The maximum angle of attack with the adaptive controller is $\alpha = 8.4°$, and $\alpha = 7.6°$ with the PID controller - both at $t \approx 133$s.

The response of the adaptive controller for a slightly increased roll reference from $\theta_{\text{cmd}} = 30°$ to $\theta_{\text{cmd}} = 33°$ is shown in figure B.2, where the response with the adaptive controller is closer to that of the PID controller in figure 6.5.

Similarly to figure 6.4, the IAE performance metric in figure 6.6 shows that up until $t \approx 145$s the PID controller has a superior tracking performance in roll, while the adaptive controller is superior in pitch.

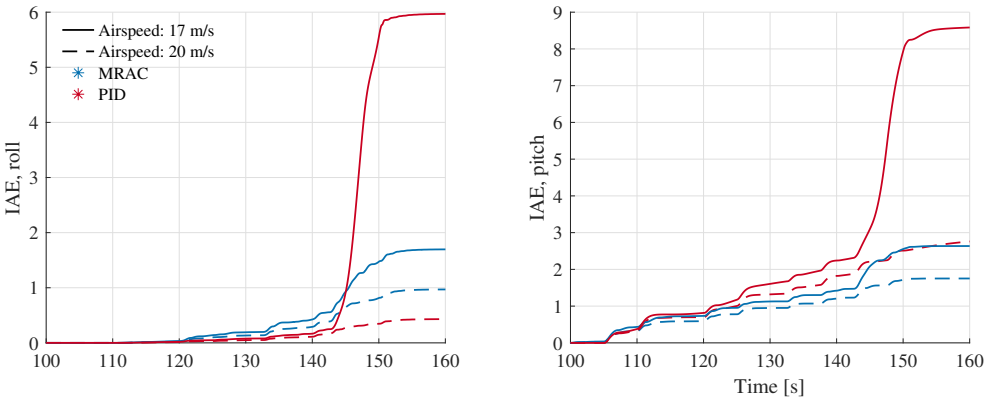

Figure 6.6: Time evolution of the integral of the absolute value of the tracking error (IAE) for the response shown in figure 6.5. The IAE metric is shown for both controllers, indicated by the two separate colors.

6.3 Wind conditions

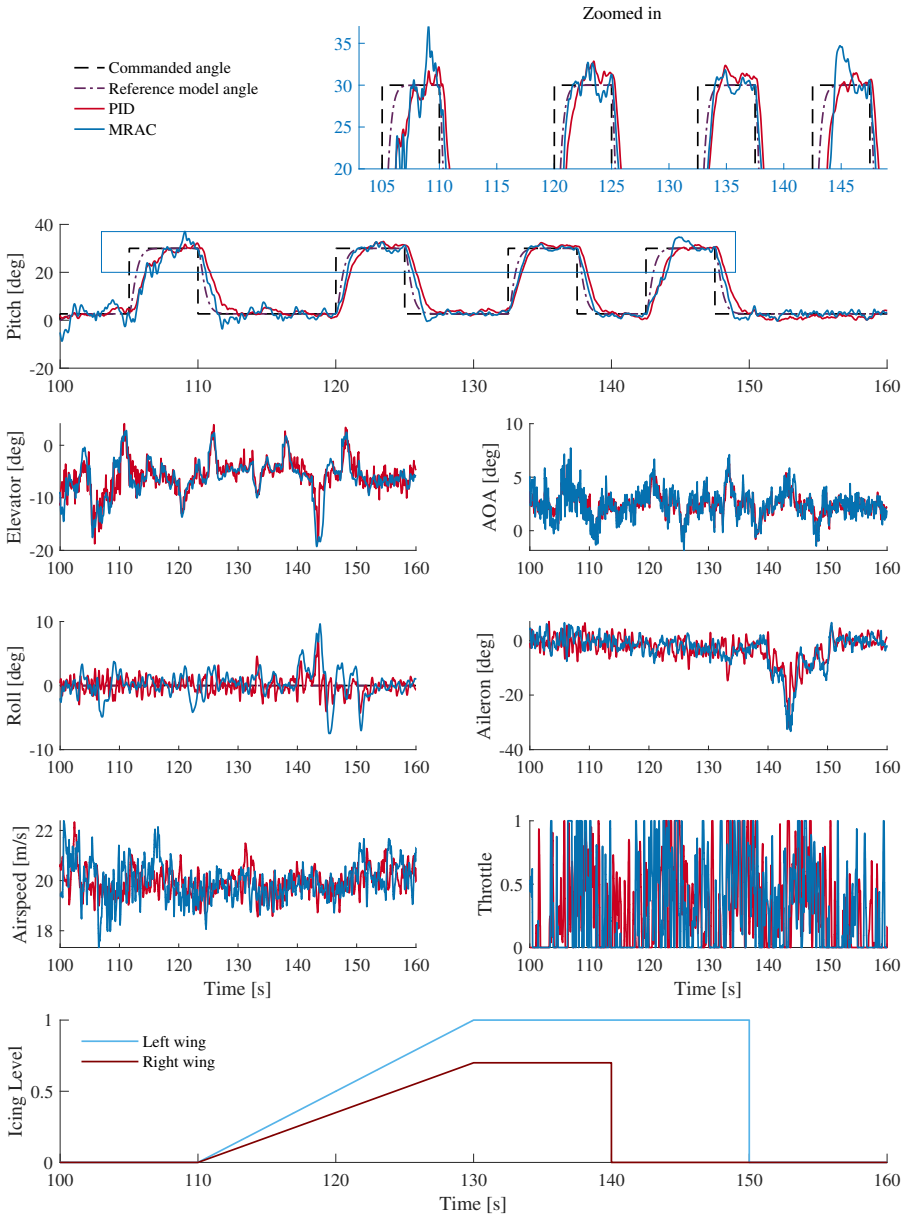

Figure 6.7: Severe wind gusts simulation case with square reference signal in pitch. The response with the adaptive controller and the PID controller is shown.

Figure 6.7 shows the response with the adaptive controller and the PID controller for the baseline pitch case in figure 6.2 with severe wind gusts. For the response in figure 6.7, the airspeed is set back to $V_a = 20\text{m/s}$ from the previous

simulation case. Not surprisingly, with the addition of wind gusts the response overall is "noiser" and visibly affected by the wind gusts.

Although the tracking performance is worse than for the baseline simulation case in figure 6.2, figure 6.7 shows that both the adaptive controller and the PID controller maintain control in the presence of wind gust disturbances. During the 100% asymmetric icing phase at $t = 140$s to $t = 150$s, the maximum roll angle deviation from the zero-degree reference is 9.6° for the adaptive controller and 7° for the PID controller.

The adaptive controller reaches a maximum angle of attack $\alpha = 7.7°$ at $t \approx 107$s, and a minimum $\alpha = -1.8°$ at $t \approx 126$s. For the PID controller the respective values are $\alpha = 6.2°$ at $t \approx 133$s and $\alpha = -1.1°$ at $t \approx 126$s.

Figure 6.8 shows the IAE performance metric for the response shown in figure 6.7. In addition to the simulation in figure 6.7 with severe wind gusts, a simulation with moderate wind gusts was run. Figure 6.8 shows the IAE for all three cases: no wind gusts, moderate and severe. The trend from the previous simulations still holds, with a better tracking performance in roll with the PID controller, and a better tracking performance in pitch with the adaptive controller. Further, the performance in pitch with the PID controller looks to be less affected by the addition of wind gusts, with the IAE curves being closer together than with the adaptive controller.

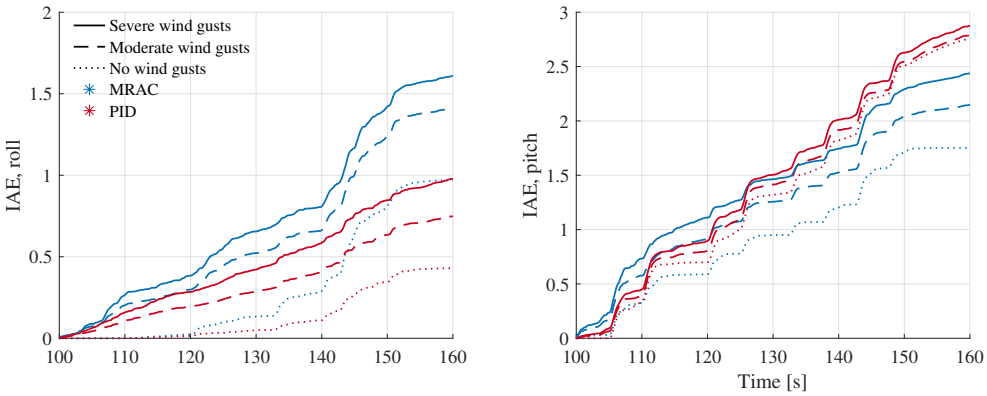

Figure 6.8: Time evolution of the integral of the absolute value of the tracking error (IAE) during severe, moderate and no wind gusts. The IAE metric is shown for both controllers, indicated by the two separate colors.

6.4 Reduced control surface effectiveness

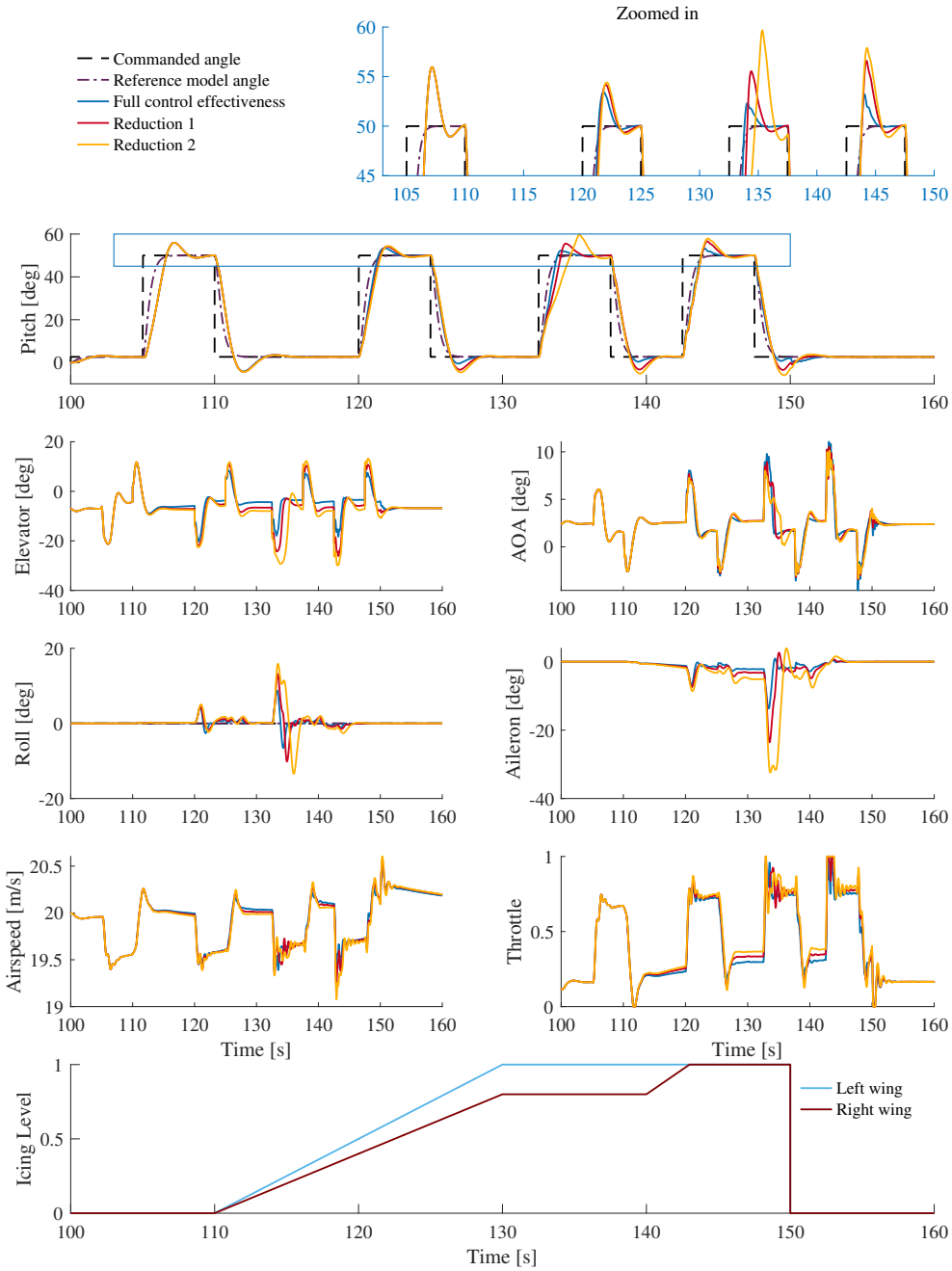

Figure 6.9: Reduced control surface effectiveness simulation case with square reference signal in pitch. The response with the adaptive controller with full control surface effectiveness, reduced control surface effectiveness according to the data of CFD simulations, and a case with a further reduction in control surface effectiveness is shown.

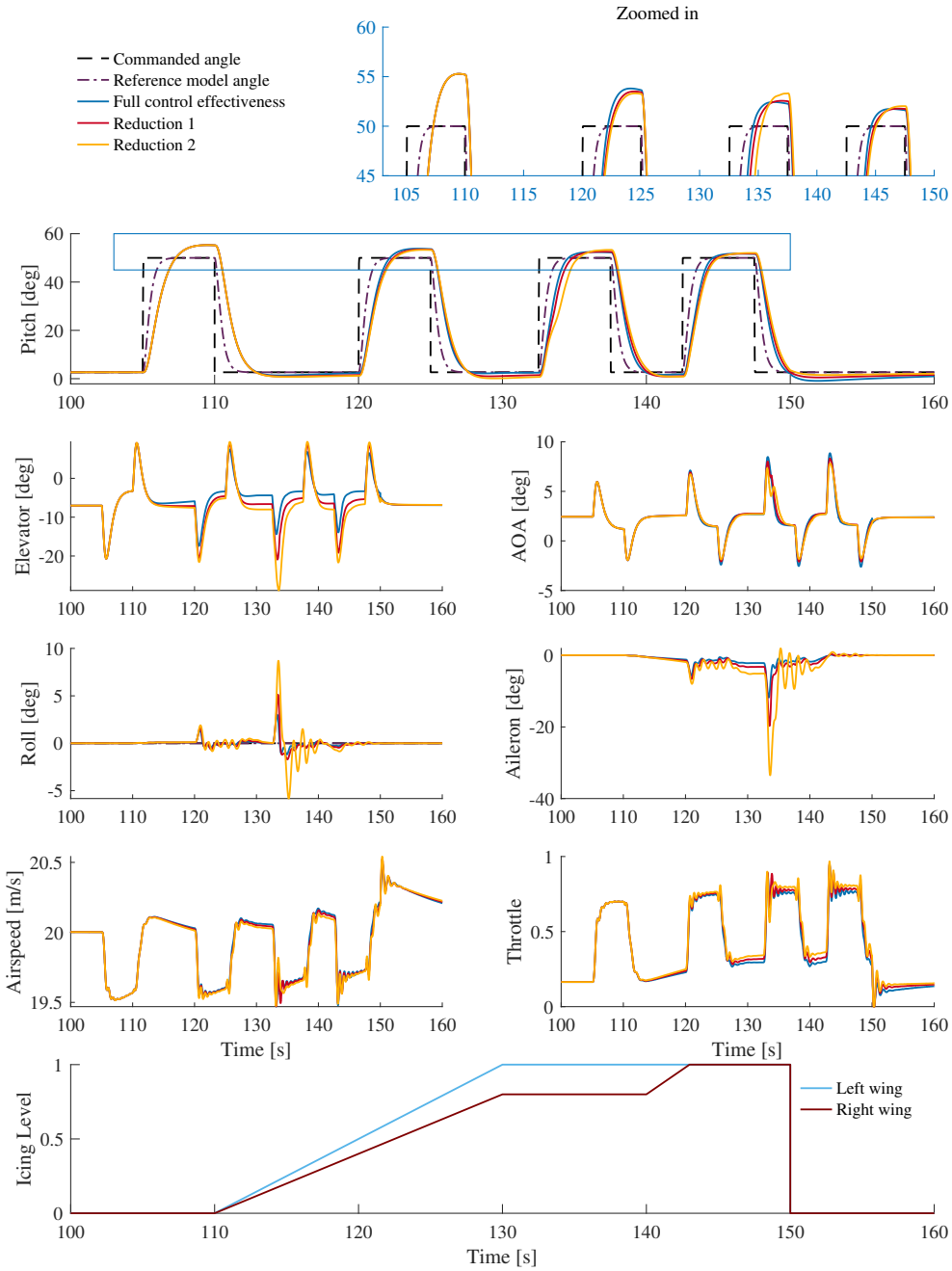

Figure 6.10: Reduced control surface effectiveness simulation case with square reference signal in pitch. The response with the PID controller with full control surface effectiveness, reduced control surface effectiveness according to the data of CFD simulations, and a case with a further reduction in control surface effectiveness is shown.

Figures 6.9 and 6.10 show the simulation case with reduced control surface effectiveness described in section 4.6.2 with a square angle reference in pitch.

Note that the reference value in this simulation case differs from the previous simulation cases, see section 4.6.2. As the limits of the controllers is reached for much lower roll and pitch deflections during the severe 100% asymmetric icing, the icing timeseries for this case is also modified. In the modified icing timeseries, the 100% asymmetric levels from $t = 140$s to $t = 150$s in the previous simulation cases is replaced with a slope up to $\zeta_{\text{right}} = 1$ for the right wing, followed by symmetric icing with $\zeta = 1$ for both wings.

Given that the reduced control surface efficiency is only reduced for the iced aerodynamic coefficient, naturally, the response only starts to deviate between the three levels of control surface effectiveness as the icing level increases. That is, for the first square signal in pitch at $t \in (105, 110)$s the response is equal for all three levels, in both figures 6.9 and 6.10.

Further, as the icing level increases, the response with the PID controller in figure 6.10 only differs slightly between the three levels of control surface effectiveness. Indicating that the control effectiveness does not have any significant effect on the performance with the PID controller within this simulator framework. The adaptive controller experiences some increased overshoots in pitch and increased roll deviations with the reduction in control surface effectiveness.

Note how any significant deviation from the roll reference only occurs from $t = 120$s to $t = 140$s, which coincides with asymmetric icing levels. When the icing level is symmetric with $\zeta = 0$ or $\zeta = 1$, the roll angle is much closer to its zero-degree reference. A likely cause of this, is that with asymmetric icing on the wings an additional roll moment is induced, throwing the UAV's balance off. And as the icing level becomes symmetric again from $t = 143$s, the roll deviations diminish. This is also seen in figure 6.11 with a large jump in the IAE metric from $t \approx 133$s to $t \approx 143$s, and then the curves settle.

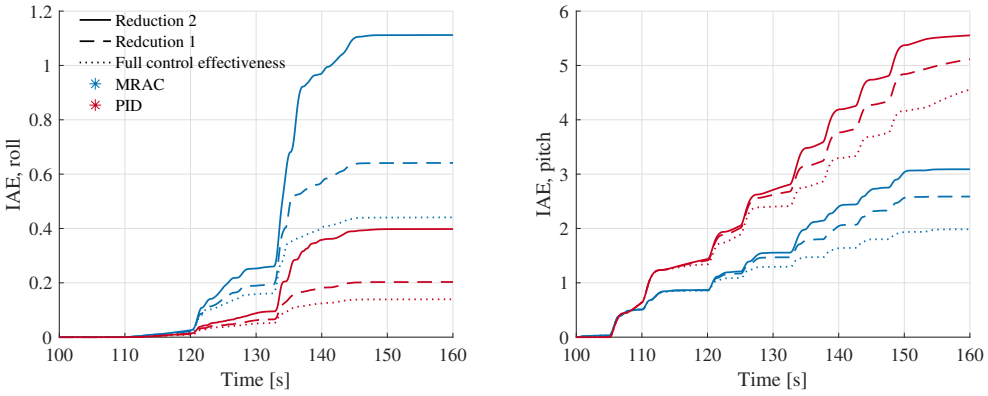

Figure 6.11: Time evolution of the integral of the absolute value of the tracking error (IAE) during full and reduced control surface effectiveness in figures 6.9 and 6.10. The IAE metric is shown for both controllers, indicated by the two separate colors.

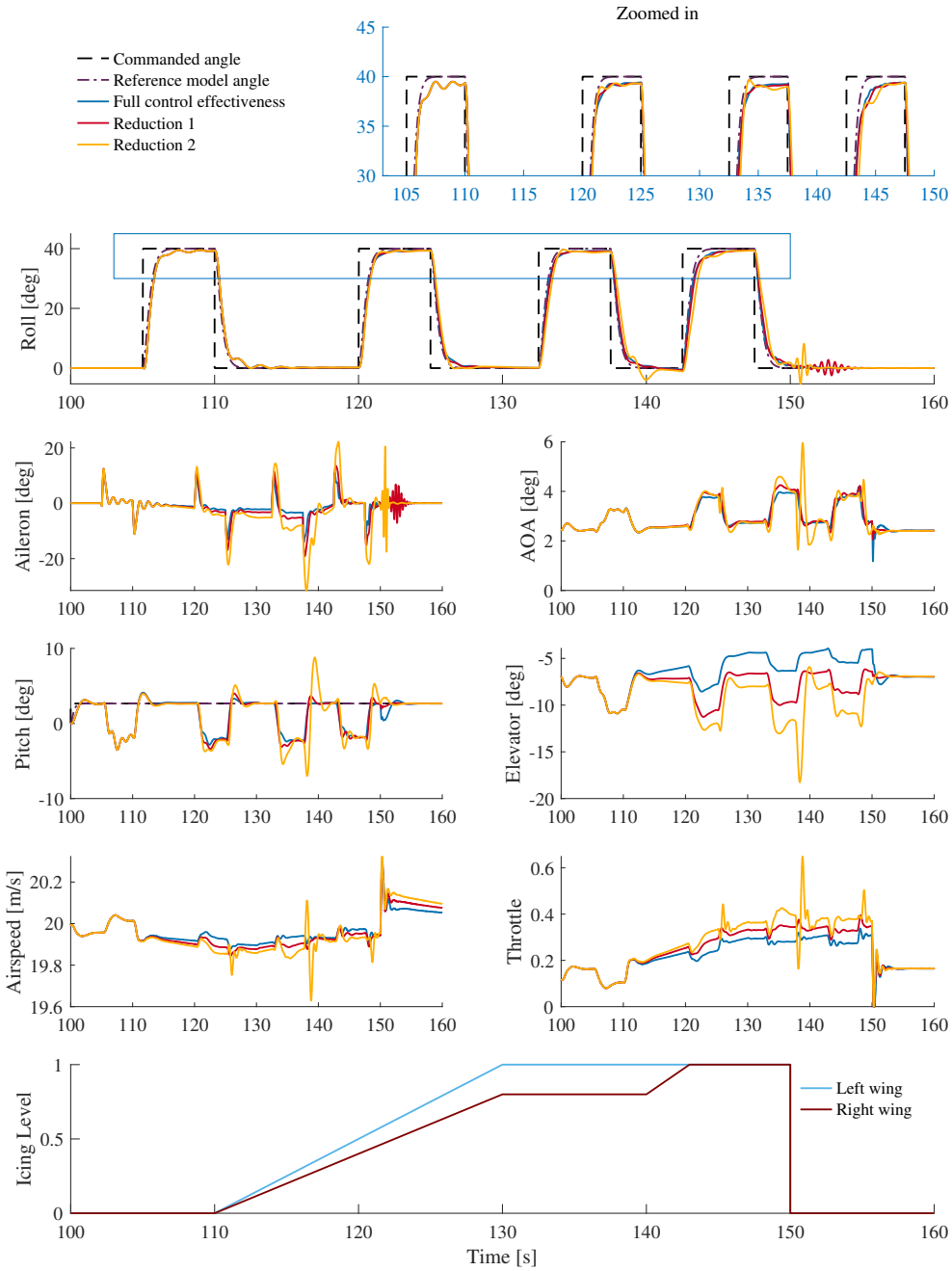

Figure 6.12: Reduced control surface effectiveness simulation case with square reference signal in roll. The response with the adaptive controller with full control surface effectiveness, reduced control surface effectiveness according to the data of CFD simulations, and a case with a further reduction in control surface effectiveness is shown.

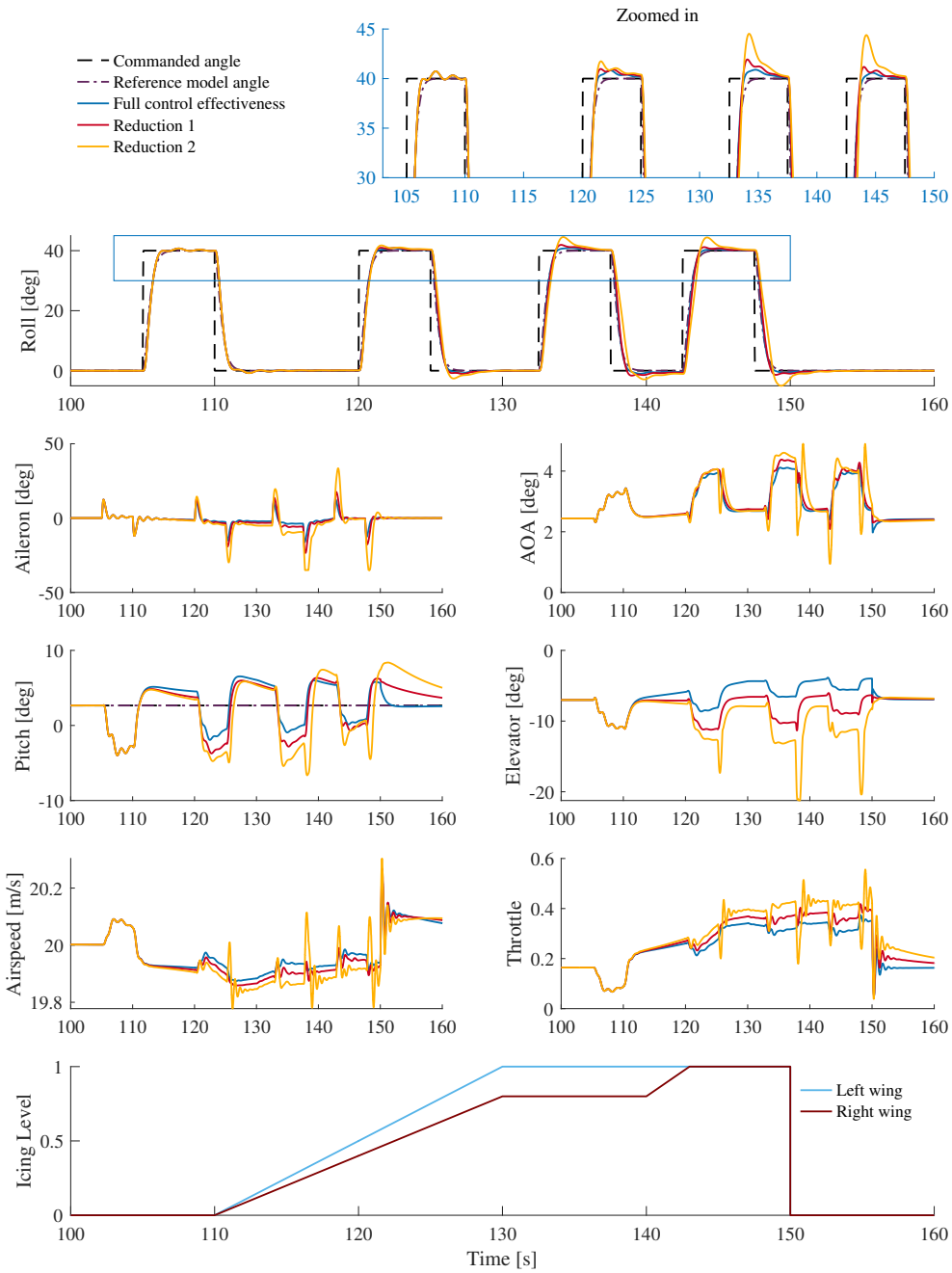

Figure 6.13: Reduced control surface effectiveness simulation case with square reference signal in roll. The response with the PID controller with full control surface effectiveness, reduced control surface effectiveness according to the data of CFD simulations, and a case with a further reduction in control surface effectiveness is shown.

Figures 6.12 and 6.13 show the simulation case with reduced control effectiveness described in section 4.6.2 with a square reference angle in roll. The icing

timeseries is described earlier in this section. Figure 6.13 shows that the MRAC controller is less influenced by the reduction in control surface effectiveness as the icing levels increase, than the PID controller. That is, the opposite finding from the previous reduced control effectiveness case with a square reference angle in pitch in figures 6.9 and 6.10.

From $t = 150$s some oscillations are seen in the roll and aileron response with the adaptive controller in figure 6.12 for both cases with reduction in control surface effectiveness. Reviewing the adaptive parameters of the roll MRAC controller given in figure 6.14 shows that the oscillations are present in the bias term, indicating that the adaptive rate of the bias gain in roll may be somewhat high.

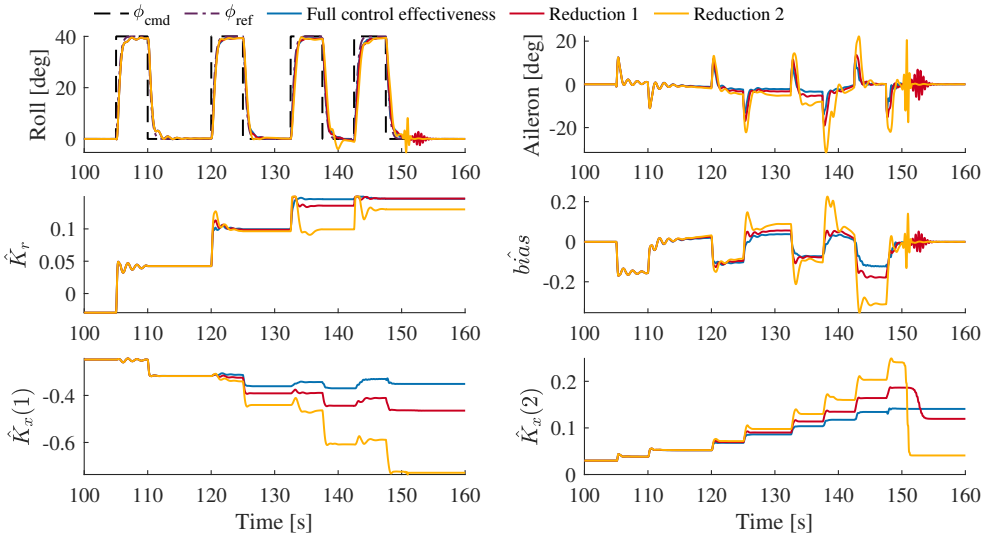

Figure 6.14: The adaptive parameters of the MRAC controller.

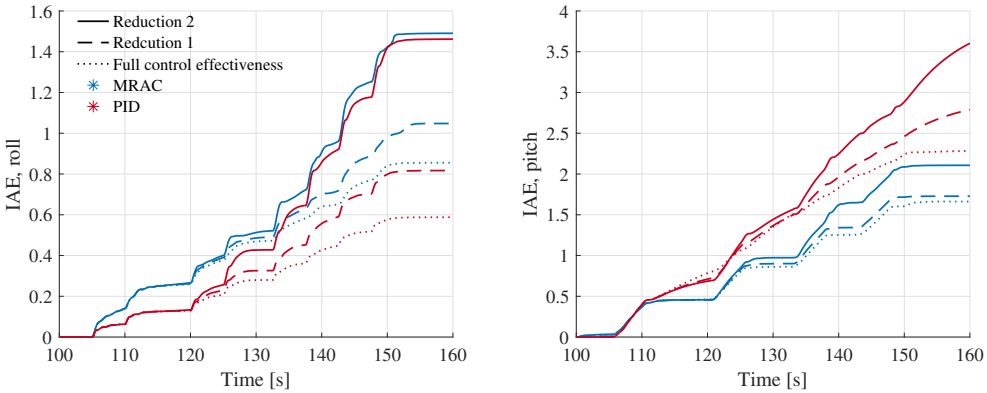

Figure 6.15: Time evolution of the integral of the absolute value of the tracking error (IAE) during full and reduced control surface effectiveness in figures 6.12 and 6.13.

6.5 Guidance

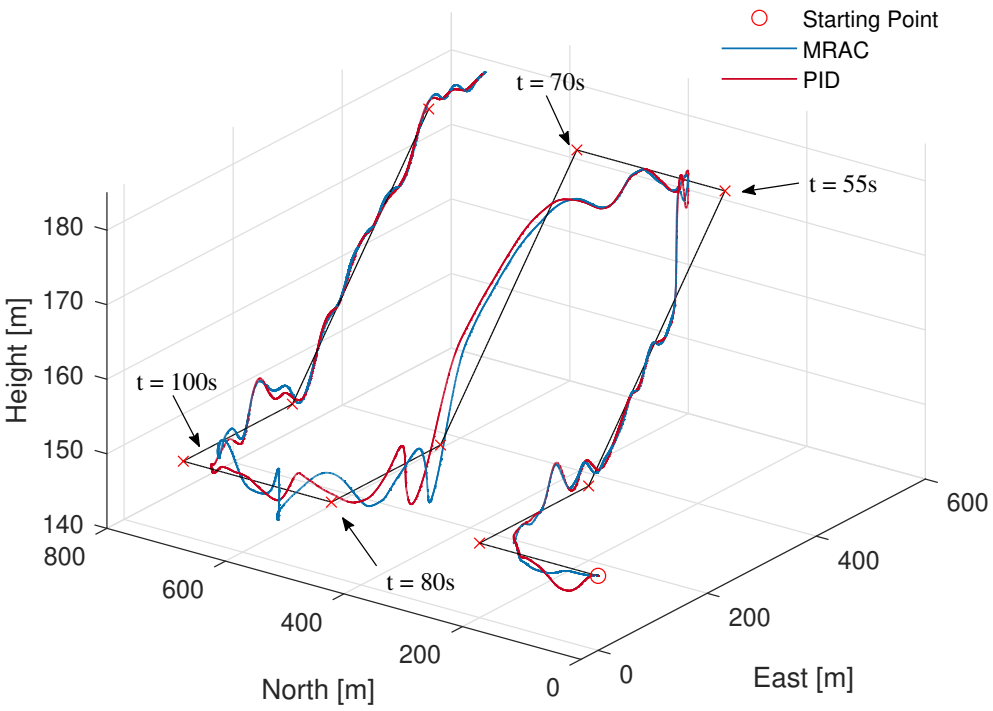

Figure 6.16: The position of the UAV during path following simulation case. The position with the adaptive controller and the PID controller is shown.

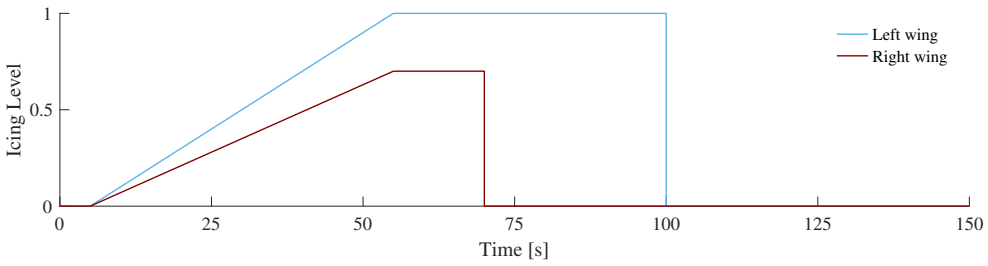

Figure 6.17: Icing timeseries for the path following case.

Figure 6.16 shows the path following simulation case described in section 4.6.3 with the adaptive controller and the PID controller. Figure 6.18 shows the simulation case seen from above (left) and seen from the eastern direction (right). The simulation case is performed with an asymmetric icing timeseries shown in figure 6.17. Additionally, there is a steady horizontal wind component from east of 10m/s with corresponding wind gusts.

Figure 6.18 shows that both controllers struggle more with the third, fourth and fifth turn than the two first. The UAV crosses the 400m mark on the North axis at $t \approx 65$s, and the 700m mark at $t \approx 105$s. The icing levels are 100%

asymmetric from $t = 70$s to $t = 100$s, indicating that the poor performance in the third through fifth turn might be due to the severe asymmetric icing conditions.

The response of the system is shown in figures B.3 and B.4 in appendix B.

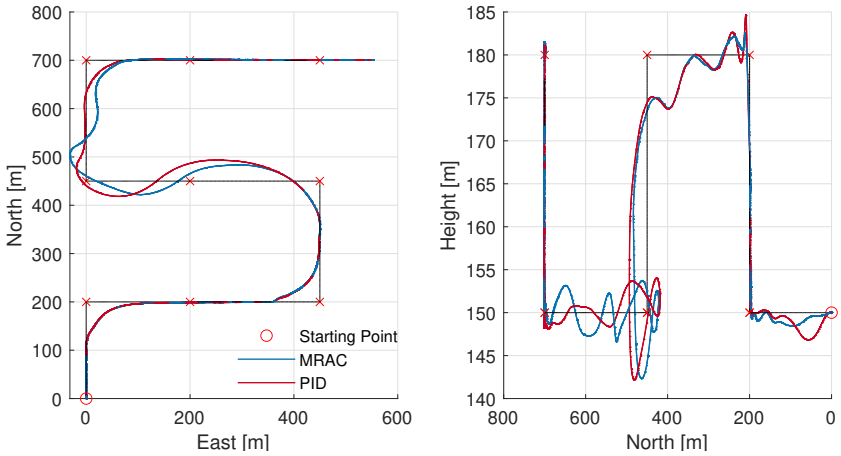

Figure 6.18: Left: The North-East position of the UAV during the path following simulation case. **Right**: The Height-East position of the UAV during the path following case.

6.6 Bias and integral term

Figures 6.19 and 6.20 show the simulation case intended to investigate the bias terms of the adaptive controller and the integral terms of the PID controller. The motivation behind this simulation case is to investigate whether the bias terms and the integral term of the controllers can detect icing. The figures show the roll and pitch response, the sideslip angle and angle of attack, the differential icing level and the sum of the icing levels, and finally the bias or integral term of the roll and pitch controllers.

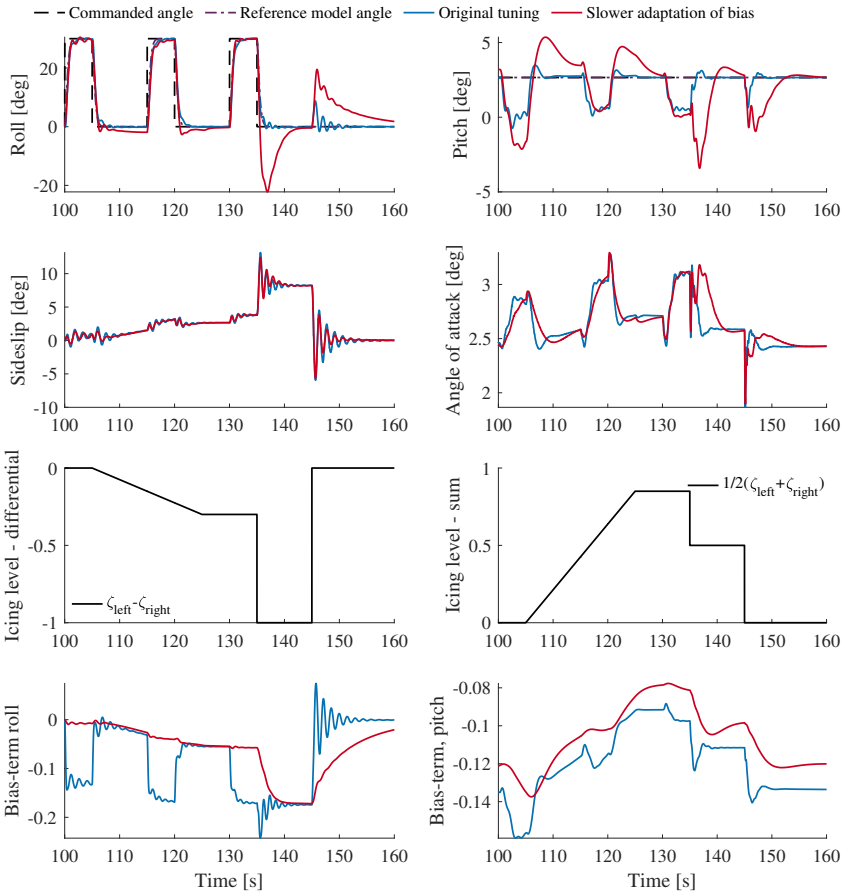

Figure 6.19: Slower tuning of the adaptive rate for the bias in roll and pitch for the adaptive controller.

The first simulation in figure 6.19 (in blue) shows the response with the so-called "Original tuning", which corresponds to the tuning values of the adaptive controller given in table 3.1. For the simulation labelled "Slower adaptation of

bias" (in red) the adaptive rates of the bias terms have been lowered from $\Gamma_\Theta = 15$ to $\Gamma_\Theta = 1$ for the roll controller, and from $\Gamma_\Theta = 10$ to $\Gamma_\Theta = 1$ for the pitch controller. With the slower adaptive rate for the bias term, it is seen from figure 6.19 that the bias term, especially in roll, looks to follow the differential icing level. With the faster rate (in blue), the bias looks to be more influenced from the sideslip angle and angle of attack.

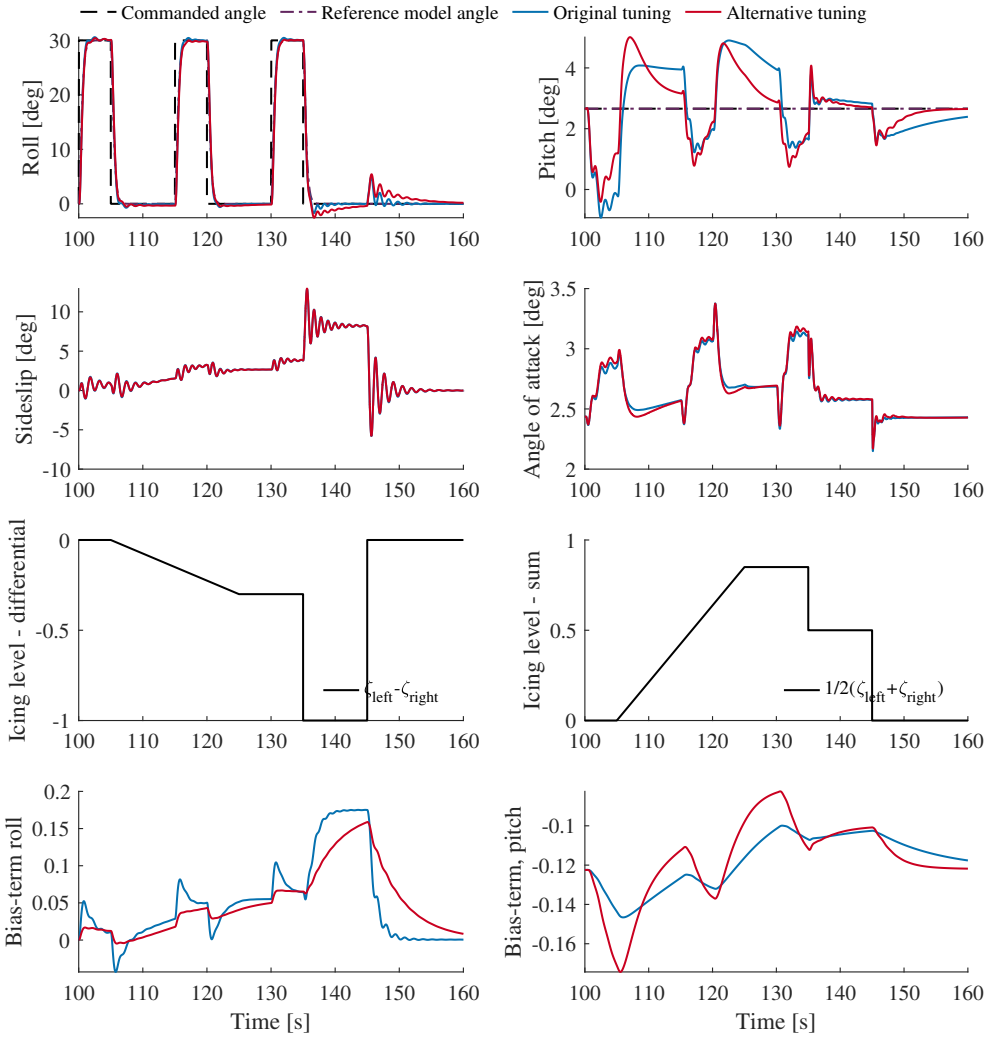

Figure 6.20: Integral term of PID

Similarly, the simulation labelled "Original tuning" (in blue) in figure 6.20 is run with the tuning values of the PID controller given in table 3.2. For the simulation labelled "Alternative tuning" (red), the integral terms are changed from $k_{i_\phi} = 2$ to $k_{i_\phi} = 0.5$, and $k_{i_\theta} = -0.1$ to $k_{i_\theta} = -0.3$. The tuning values of the "Alternative tuning" case were found by attempting to tune the integral terms to closer match the differential and sum of the icing level. The integral

term in roll was lowered, resulting in less peaks from $t = 100$s to $t = 135$s. However, that also resulted in a slower response in the integral term during the largest peak in the differential icing level at $t \in (135, 145)$s. The integral term in pitch in figure 6.20 is increased slightly from its "original" tuning as the integral term looked to be a bit slow with respect to capturing the sum of the icing levels. However, neither increasing nor decreasing k_{i_θ} resulted in an increased similarity to the sum of the icing levels.

A simulation with the icing timeseries for the left and right wings switched (not shown) such that the sign of the differential icing level flips, showed that the sign of the bias term and integral term in roll also flip.

Chapter 7

Discussion

In this chapter, the simulation results from chapter 6, as well as future work and improvements, are discussed.

7.1 Stalling

As stated in section 4.4, the simulator used in this thesis does not take into account stalling of the aircraft. Therefore, the validity of each test run must be evaluated afterward by verifying that the angle of attack is within the stall limit. However, a specific limit to use for validation of a simulation is not easily determined. The stall angle is different depending on whether the wing is iced or clean, and throughout a simulation the icing levels can be set to be in a range of values between the clean and iced case. Additionally, the stall limit for the iced and clean case also depends on the control surface deflection, as stated in section 4.2.1.

For the simulations in this thesis, the modelling by Winter [14] and the extension to an asymmetric aerodynamic model by Kleiven [6] has been assumed to be valid. Winter [14] suggests a stall limit in the fully iced case of $\alpha_{\text{stall}} \approx 10°$. However, the CFD analysis in section 4.2.1, suggests that the stall limit is closer to $\alpha_{\text{stall}} \approx 4°$ in the fully iced case. The reason for this discrepancy, as described in the paper in appendix C, could stem from the differences in the configurations in the CFD simulations from the configuration used in Winter [14], such as variations in chord length and hinge location, and the fact that the airfoil of the Skywalker X8 is unknown and that the two approximations may reflect different behaviour.

As mentioned in section 4.2.1, the CFD analysis is only used to find an estimate

of the reduction in control surface effectiveness from the clean case to the fully iced case. Nevertheless, due to the uncertainty in the stall limit for the iced case, the values of the angle of attack and stalling of the UAV have not been the focus in this thesis. More work must be done to determine accurate ranges for the stall limit in icing.

7.2 Effects of icing

Some overall observations of the simulation cases in chapter 6 show that with increased icing levels, the throttle usage increases and the angle of attack increases. The increase in throttle is expected as the drag increases with the icing level.

Further, the results in chapter 6 show that the 100% asymmetric icing case, i.e. when the left wing is fully iced and the right wing is clean, is the most severe icing case with respect to the performance of the controllers. The greater the asymmetry, the greater the coupling of the roll and pitch dynamics is. An example of the increase in coupling between the two states with increased asymmetry, is observed as the deviations from the zero-degree reference in roll during pitch deflections is larger for increased asymmetry. This can be seen in figures 6.2, 6.5, 6.7 and 6.9. In particular, figure 6.9 shows a good example of this where the deviation in the roll angle is significantly reduced as the icing level goes from asymmetric to symmetric fully iced. That is, the simulation shows that the asymmetry is the deciding factor, and not just the increased icing level in itself. This is consistent with the theory and how the simulator is implemented, as the asymmetric icing level induces an additional roll moment throwing the UAV off balance.

The reduced control surface effectiveness simulation case with a pitch angle reference in section 6.4, shows that the pitch response with MRAC controller is more affected by the changes in control surface effectiveness than the PID controller. With the square roll angle reference in figure 6.12, the opposite is true, where the roll response with the PID controller is more affected by the changes in control surface effectiveness than the MRAC controller.

7.3 Comparison of performance

The tracking performance of the controllers in this thesis is mainly assessed quantitatively by the IAE performance metric. The comparisons of the IAE metric between the adaptive controller and the PID controller, show that the PID controller generally has a better tracking performance in roll, while the

adaptive controller has a better tracking performance in pitch. The previous observation is valid up to the point in time of when the tracking performance degrades with the PID controller in the reduced airspeed case in section 6.2.

For the simulation case with severe, moderate and no wind gusts in section 6.3, the tracking performance decreases as the intensity of the wind gusts increase, as expected. However, a noteworthy observation is that the tracking performance in pitch with the PID controller is very similar for all three cases. Indicating that the pitch angle tracking with the PID controller is not as affected by disturbances as the adaptive controller.

The tuning of the controllers plays a significant role in the first grouping of results. The difficult aspect of tuning is finding a tuning that results in good tracking performance under several conditions and references. For instance, tuning the PID controller to be less aggressive will delay the degradation of the tracking performance to a larger reference angle in the reduced airspeed case in section 6.2. However, the less aggressive tuning also results in worse tracking performance in the wind condition case in section 6.3. Similarly, the adaptive control scheme also has trade-offs with respect to tuning. Increasing the adaptive rates generally increases the tracking performance, however increased rates also come with increased oscillations in the response.

7.4 Bias and integral terms

From the examination of the bias terms in section 6.6, there is an indication that a bias term might be able to detect the icing levels of the airfoils. However, for faster adaptive rates of the bias terms, they seem to also capture the effects of the sideslip angle and the angle of attack, and perhaps additional unmodelled effects. As such, an estimate of the icing level comes at the cost of worsened tracking performance with the slower adaptive rate of the bias terms with the adaptive controller in its current state.

Some further work on this might be able to produce an estimate of the icing levels, which would be very beneficial for the development of ice protection systems. Some paths forward could be modifying the MRAC model equations in an attempt to separate the icing effects from other unmodelled effects. During the design of the regressor, $\boldsymbol{\Phi}(\boldsymbol{x})$, one could choose to include compensating linear terms in the sideslip and angle of attack, and thereby infer the effect of these through their respective adaptive parameters. That is, setting $f(\boldsymbol{x})$ in equation (2.12) to $[\theta_{\text{bias,roll}} \quad \theta_\beta][1 \quad \beta]^\top$ in the roll model equations, and to $[\theta_{\text{bias,pitch}} \quad \theta_\alpha][1 \quad \alpha]^\top$ in the pitch model equations. This would be especially pertinent seeing how these terms appear in the full equations of motion of an aircraft in [17]. In this thesis, sideslip angle and angle of attack were deliber-

ately not included in the regessor since these quantities are difficult to measure accurately for a UAV [32]. Nonetheless, a significant challenge in continuing down this path will be to produce a *reliable* estimate of the icing level across several atmospheric conditions and flight scenarios.

The roll integral term of the PID controller also seems to capture the effects of icing to some degree. In light of section 3.1.1 where the both the bias and integral term are shown to perform a steady state compensation, it is not unexpected that the bias and integral term exhibit a similar behavior.

7.5 Future work

A crucial step in improving the validity of the results in this thesis, is improving the aerodynamic model of the Skywalker X8. Additionally, developing aerodynamic models for a less severe icing condition than the mixed ice in the model of this thesis, will also provide a better reflection of the expected icing conditions during real life flight. Improving the model with aerodynamic data for some of the intermediate levels of icing, between the iced and the clean case, will also mitigate some of the uncertainty related to the behavior of the UAV for these intermediate levels. The clear benefit of an improved model of the Skywalker X8 is shortening the bridge from the controllers developed in the simulator to using them in real life flight. Related to this is also improving the simulator by taking into account the effect of stalling.

An interesting path forward from the adaptive controller, is to investigate whether an adaptive control scheme or a separate system identification scheme can detect the icing level on the airfoils. It would be interesting to see if this is possible, and how reliable the estimates of the icing levels could be. Having an estimate of the icing level will be very beneficial for the development of ice protection systems.

Furthermore, comparing the adaptive MRAC scheme developed in this thesis with the controllers used in most UAV flights today will increase the validity of the results. For instance, comparing the adaptive control scheme with the controllers developed in ArduPilot[1] would give a better measure of the performance of the MRAC than provided in this thesis.

Moreover, some modifications and improvements of the adaptive control scheme can be investigated further. In this thesis, to increase robustness of the controller, projection of the adaptive parameters was implemented. Additionally, projection in the control input, described in Lavretsky and Wise [9], to ensure less aggressive control inputs could also be tested.

[1] ArduPilot is an open-source autopilot software.

Chapter 8

Concluding remarks

This thesis has investigated inner loop adaptive control of the fixed-wing Skywalker X8 UAV in icing conditions. An MRAC control scheme has been implemented and its performance compared with a PID controller. The MRAC model was chosen as a linear model with a bias term to capture additional unmodelled effects. The simulator framework and aerodynamic model used in this thesis has its shortcomings and limitations, that have been described and discussed in this thesis. Among them is that stalling is not taken into account in the simulator model. However, the simulator framework is believed to capture the effects of icing on the UAV, which is the point of interest in this thesis.

To assess the tracking performance of the controllers the integral of the absolute error was used as a metric. Through several simulation cases it was found that the performance of the MRAC and PID were quite similar. However, the MRAC performs better in the case of reduced airspeed for asymmetric icing levels. With the selected tuning of the controller, the PID controller shows better tracking performance in the roll angle, whereas the MRAC control scheme has a better tracking performance in the pitch angle. A path following simulation case representing a more realistic application of the control schemes, also showed the PID and MRAC controllers to have similar performance. Both the inner loop simulation cases and the outer loop path following case showed that both control schemes struggle the most in the presence of 100% asymmetric icing.

Computational fluid dynamics analysis allowed for a realistic simulation of the reduced control surface effectiveness due to icing. The results show that the MRAC controller is less affected by the reduction in control surface efficiency than the PID control scheme with a square reference angle in roll, while the opposite is true with a square reference angle in pitch.

By modifying the tuning, the bias terms of the MRAC control scheme, and to some degree the integral terms of the PID controller, are able to capture the icing levels on the airfoils of the UAV. Further work into this observation towards developing reliable estimates of the icing levels will be beneficial for the development of ice protection systems.

As a concluding remark, it is noted that the MRAC control scheme is more complex and introduces more tuning parameters than the PID control scheme - while they prove similar performance, with the MRAC performing better under certain conditions as discussed in this thesis. Additionally, with the increased complexity and the system identification aspect of the MRAC scheme comes the possibility of exploring icing level estimation.

Bibliography

[1] M. Bragg, A. Broeren and L. Blumenthal, 'Iced-airfoil aerodynamics,' *Progress in Aerospace Sciences*, vol. 41, no. 5, pp. 323–362, 2005, ISSN: 0376-0421. DOI: https://doi.org/10.1016/j.paerosci.2005.07.001.

[2] F. T. Lynch and A. Khodadoust, 'Effects of ice accretions on aircraft aerodynamics,' en, *Progress in Aerospace Sciences*, vol. 37, no. 8, pp. 669–767, Nov. 2001, ISSN: 0376-0421. DOI: 10.1016/S0376-0421(01)00018-5.

[3] R. Hann and T. A. Johansen, 'UAV icing: The influence of airspeed and chord length on performance degradation,' *Aircraft Engineering and Aerospace Technology*, vol. 93, 5 Aug. 2021, ISSN: 1748-8842. DOI: 10.1108/AEAT-06-2020-0127.

[4] R. Hann, A. Enache, M. C. Nielsen, B. N. Stovner, J. van Beeck, T. A. Johansen and K. T. Borup, 'Experimental heat loads for electrothermal anti-icing and de-icing on UAVs,' *Aerospace*, vol. 8, 3 Mar. 2021, ISSN: 22264310. DOI: 10.3390/aerospace8030083.

[5] R. Hann, 'Atmospheric ice accretions, aerodynamic icing penalties, and ice protection systems on unmanned aerial vehicles.,' Ph.D. dissertation, Norwegian University of Science and Technology, 2020.

[6] R. Kleiven, 'Robust and gain scheduled flight control of fixed-wing UAVs in wind and icing conditions,' M.S. thesis, Norwegian University of Science and Technology, 2021.

[7] P. A. Ioannou and J. Sun, *Robust adaptive control*. Mineola, New York: Dover Publications, Inc, 2012, ISBN: 9780486498171.

[8] K. J. Åström and B. Wittenmark, *Adaptive control*, 2nd ed., Dover ed, ser. Dover books on engineering. Mineola, N.Y: Dover Publications, 2008, OCLC: ocn196313137, ISBN: 9780486462783.

[9] E. Lavretsky and K. A. Wise, *Robust and adaptive control: with aerospace applications*, ser. Advanced textbooks in control and signal processing. London ; New York: Springer, 2013, OCLC: ocn837660452, ISBN: 9781447143956.

[10] H. P. Whitaker, J. Yamron and A. Kezer, *Design of model-reference adaptive control systems for aircraft*. Massachusetts Institute of Technology, Instrumentation Laboratory, 1958.

[11] B. Shachcloth and R. Butchart, 'Synthesis of model reference adaptive control systems by lyapunov's second methods,' *IFAC Aymposium, Jeddinglon*, 1965.

[12] P. Parks, 'Liapunov redesign of model reference adaptive control systems,' *IEEE Transactions on Automatic Control*, vol. 11, no. 3, pp. 362–367, 1966.

[13] G. Chowdhary, E. N. Johnson, R. Chandramohan, M. S. Kimbrell and A. Calise, 'Guidance and control of airplanes under actuator failures and severe structural damage,' *Journal of Guidance, Control, and Dynamics*, vol. 36, no. 4, pp. 1093–1104, 2013. DOI: 10.2514/1.58028.

[14] A. Winter, 'Systems identification, flight performance, and control of a fixed-wing UAV in icing conditions,' M.S. thesis, Norwegian University of Science and Technology, 2019.

[15] Y. Liu, L. Li, W. Chen, W. Tian and H. Hu, 'An experimental study on the aerodynamic performance degradation of a uas propeller model induced by ice accretion process,' *Experimental Thermal and Fluid Science*, vol. 102, pp. 101–112, 2019, ISSN: 0894-1777. DOI: https://doi.org/10.1016/j.expthermflusci.2018.11.008.

[16] R. F. Stengel, *Flight Dynamics*, English. Princeton, NJ: Princeton University Press, Oct. 2004, ISBN: 9780691114071.

[17] R. W. Beard and T. W. McLain, *Small Unmanned Aircraft: Theory and Practice*. USA: Princeton University Press, 2012, ISBN: 0691149216.

[18] S. Högnadottir, *Inner loop adaptive control of fixed-wing unmanned aerial vehicles in icing conditions*, unpublished, 2021.

[19] L. L. Trimmer and E. L. Clark, 'Transformation of Axes System by Matrix Methods and Application to Wind Tunnel Data Reduction,' en, Arnold Engineering Development Center Arnold AFB TN, Tech. Rep., Oct. 1963.

[20] K. Gryte, 'High angle of attack landing of an Unmanned Aerial Vehicle,' M.S. thesis, 2015.

[21] T. I. Fossen, *Handbook of marine craft hydrodynamics and motion control =: Vademecum de navium motu contra aquas et de motu gubernando*, Second edition. Hoboken, NJ: Wiley, 2021, ISBN: 9781119575054.

[22] D. I. You, Y. D. Jung, S. W. Cho, H. M. Shin, S. H. Lee and D. H. Shim, 'A Guidance and Control Law Design for Precision Automatic Take-off and Landing of Fixed-Wing UAVs,' en, in *AIAA Guidance, Navigation, and Control Conference*, Minneapolis, Minnesota: American Institute of Aeronautics and Astronautics, Aug. 2012, ISBN: 9781600869389. DOI: 10.2514/6.2012-4674.

[23] S. O. Nevstad, 'Autonomous landing of fixed-wing uav in net suspended by multirotor UAVs,' M.S. thesis, 2016.

[24] O. Harkegard and S. Torkel Glad, 'A backstepping design for flight path angle control,' in *Proceedings of the 39th IEEE Conference on Decision and Control (Cat. No.00CH37187)*, ISSN: 0191-2216, vol. 4, Dec. 2000, 3570–3575 vol.4. DOI: 10.1109/CDC.2000.912259.

[25] R. Hann, A. Wenz, K. Gryte and T. A. Johansen, 'Impact of atmospheric icing on UAV aerodynamic performance,' in *2017 Workshop on Research, Education and Development of Unmanned Aerial Systems (RED-UAS)*, Linkoping: IEEE, Oct. 2017, pp. 66–71, ISBN: 9781538609392. DOI: 10.1109/RED-UAS.2017.8101645.

[26] *Dryden wind turbulence model (continuous)*, https://se.mathworks.com/help/aeroblks/drydenwindturbulencemodelcontinuous.html.

[27] *MIL-F-8785C, military specification: Flying qualities of piloted airplanes*, 1980.

[28] R. Kleiven, *Flight control analysis toolbox (FCAT)*, https://github.com/rukleiven/fcat, 2021.

[29] *N-D Lookup Table*, https://se.mathworks.com/help/simulink/slref/ndlookuptable.html.

[30] *Horizontal Wind Model*, https://se.mathworks.com/help/aeroblks/horizontalwindmodel.html.

[31] N. Fajt, R. Hann and T. Lutz, 'The Influence of Meteorological Conditions on the Icing Performance Penalties on a UAV Airfoil,' 15 pages, 2019. DOI: 10.13009/EUCASS2019-240.

[32] A. Wenz and T. A. Johansen, 'Moving horizon estimation of air data parameters for uavs,' *IEEE Transactions on Aerospace and Electronic Systems*, vol. 56, no. 3, pp. 2101–2121, 2020. DOI: 10.1109/TAES.2019.2946677.

Appendix A

Parameters

A.1 Tuning parameters

Table A.1: The adaptive rates of the MRAC scheme.

Roll adaptive rates		**Pitch adaptive rates**	
Parameter	Value	Parameter	Value
$\boldsymbol{Q}$	$\begin{bmatrix} 3 & 0 \\ 0 & 1 \end{bmatrix}$	$\boldsymbol{Q}$	$\begin{bmatrix} 4 & 0 \\ 0 & 0.4 \end{bmatrix}$
$\boldsymbol{\Gamma}_x$	$\begin{bmatrix} 12 & 0 \\ 0 & 4 \end{bmatrix}$	$\boldsymbol{\Gamma}_x$	$\begin{bmatrix} 6 & 0 \\ 0 & 0.01 \end{bmatrix}$
$\boldsymbol{\Gamma}_r$	10	$\boldsymbol{\Gamma}_r$	5
$\boldsymbol{\Gamma}_\Theta$	15	$\boldsymbol{\Gamma}_\Theta$	10

Table A.2: The tuning parameters of the roll and pitch PID controllers.

Roll controller gains		**Pitch controller gains**	
Parameter	Value	Parameter	Value
k_{p_ϕ}	2.5	k_{p_θ}	-1
k_{i_ϕ}	2	k_{i_θ}	-0.1
k_{d_ϕ}	0.01	k_{d_θ}	-0.25

Table A.3: The tuning parameters of the guidance controller.

Parameter	Value
Δ_{lat}	33
k_{p_χ}	2
k_{i_χ}	0.1
k_{ph}	0.8
k_{ih}	0.1
$R_{\max}$	20°
c_1	0.001
k_{p_V}	0.6
k_{i_V}	0.01
$k_{p_{z_e}}$	0.1
δ^*	0.44

A.2 Skywalker X8 parameters

Table A.4: Skywalker X8 physical parameters

Parameter	Symbol	Value	
Mass	m	3.364	kg
Wing span	b	2.1	m
Mean chord	c	0.3571	m
Wing area	S	0.75	m^2
Area swept by the propeller	S_{prop}	0.1018	m
Propeller constant	C_{prop}	40	
Motor constant	k_{motor}	1	
	I_x	0.335	kgm^2
	I_y	0.140	kgm^2
	I_z	0.400	kgm^2
	I_xz	-0.029	kgm^2

Appendix B

Additional Simulation Figures

This appendix includes additional simulations figures to the simulations given in chapter 6.

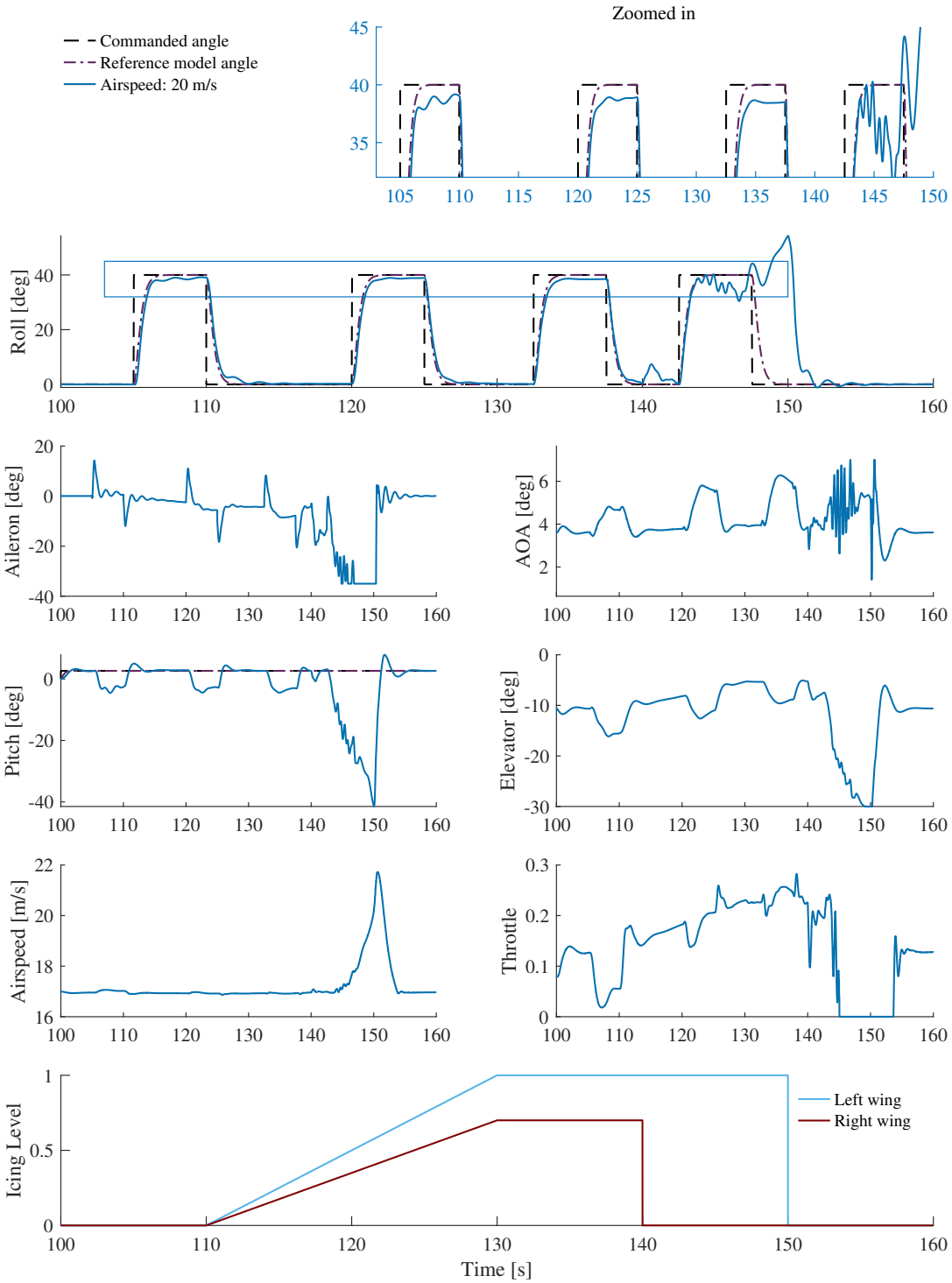

Figure B.1: The response of the adaptive controller for an increased roll reference from $\phi_{\text{cmd}} = 30°$ to $\phi_{\text{cmd}} = 40°$ and the airspeed set to $V_a = 17\text{m/s}$. See the results in section 6.2.

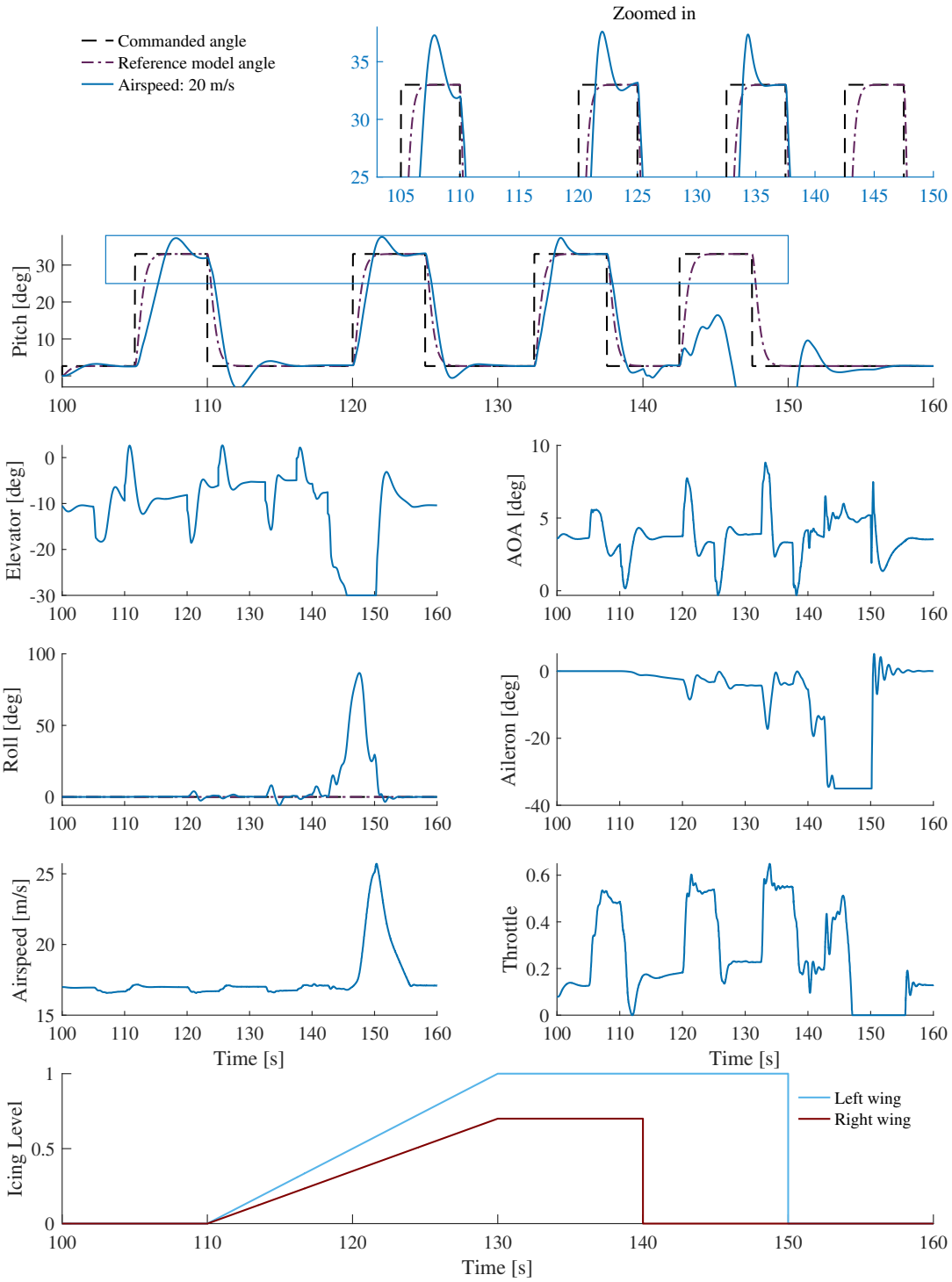

Figure B.2: The response of the adaptive controller for an increased pitch reference from $\theta_{\text{cmd}} = 30°$ to $\theta_{\text{cmd}} = 33°$ and the airspeed set to $V_a = 17\text{m/s}$. See the results in section 6.2.

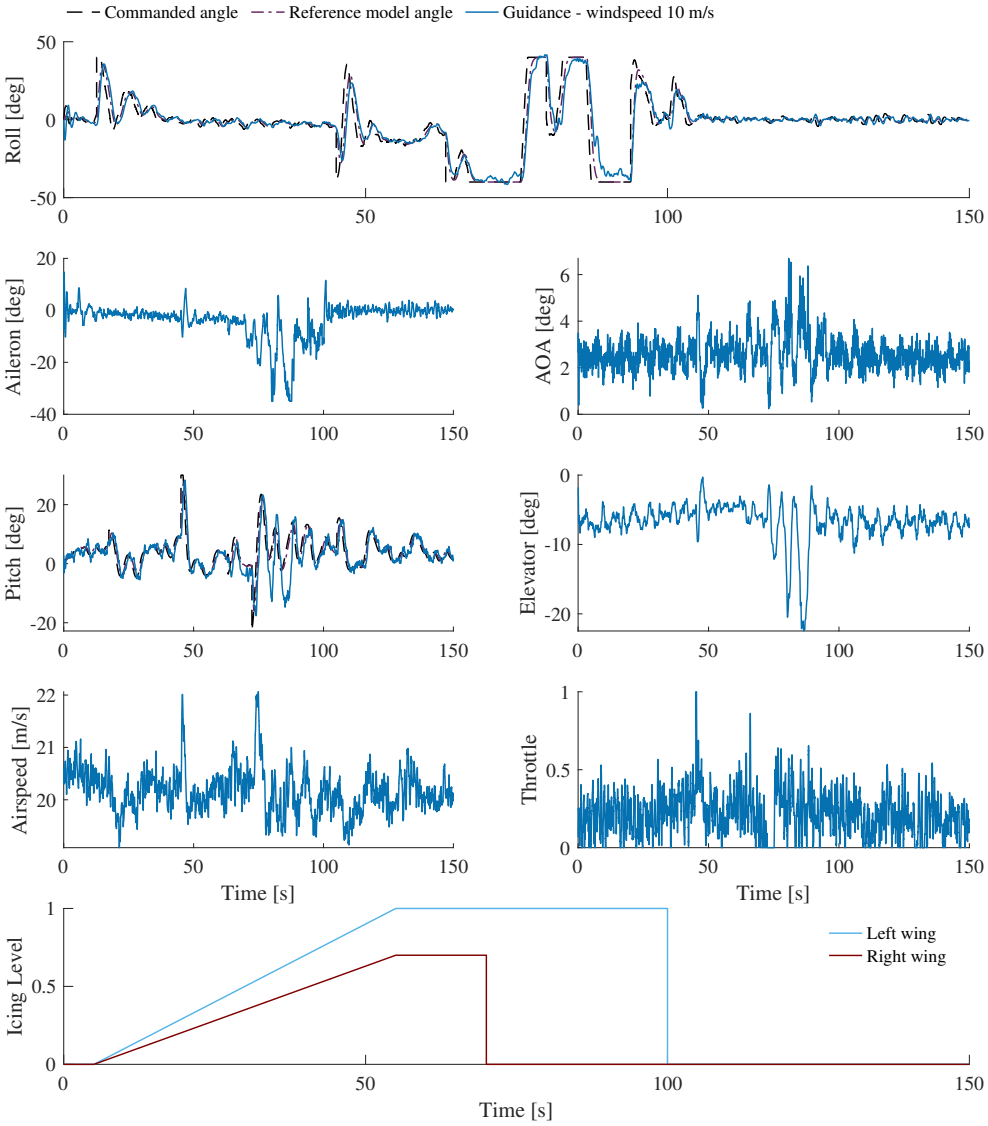

Figure B.3: The response of the UAV with the adaptive controller during the path following simulation case. See the results in section 6.5.

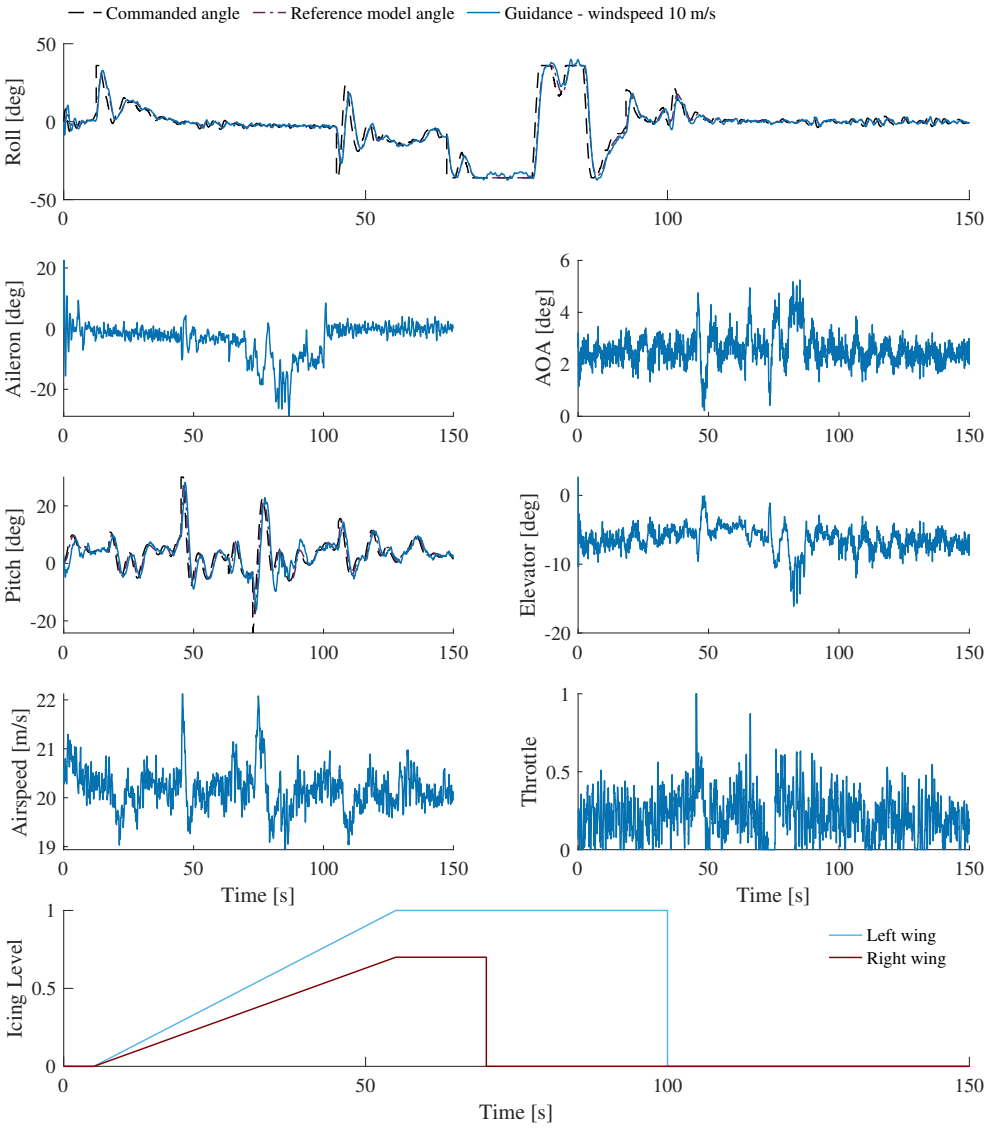

Figure B.4: The response of the UAV with the PID controller during the path following simulation case. See the results in section 6.5.

Appendix C

Submitted paper

This appendix includes the paper written based on the findings in this thesis,

- S. Högnadottir, K. Gryte, R. Hann, and T. A. Johansen, "Inner-Loop Control of Fixed-Wing Unmanned Aerial Vehicles in Icing Conditions", *AIAA SciTech*, 2022, Submitted

Inner-Loop Control of Fixed-Wing Unmanned Aerial Vehicles in Icing Conditions

Sif Högnadottir*, Kristoffer Gryte†, Richard Hann‡ and Tor Arne Johansen§
Department of Engineering Cybernetics,
Center for Autonomous Marine Operations and Systems,
Norwegian University of Science and Technology,
Trondheim, Norway

This paper compares a model reference adaptive control (MRAC) scheme with PID controllers. Both are developed for the Skywalker X8 fixed-wing unmanned aerial vehicle operating in icing conditions, encompassing asymmetric icing on the wings and reduced control effectiveness. The MRAC scheme is given by a linear model with a bias term to capture unmodeled effects, and modified with the projection operator to increase robustness. The findings in this paper show that the MRAC control scheme and the PID controller demonstrate similar qualities in tracking performance with the MRAC performing better under certain conditions. Overall, both controllers exhibit the most difficulty when the icing level is severely asymmetric. Examining the bias and integral terms of the adaptive controller and PID controller, respectively, shows that the bias terms when the adaptive rate is lowered, and to some degree the roll integral term, are able to detect icing.

I. Nomenclature

ρ	=	Air density
V_a	=	Airspeed
b	=	Wing span
c	=	Chord length
α	=	Angle of attack
β	=	Sideslip angle
ϕ	=	Roll angle
θ	=	Pitch angle
p	=	Roll rate
q	=	Pitch rate
r	=	Yaw rate
δ_a	=	Aileron deflection
δ_e	=	Elevator deflection
δ_r	=	Rudder deflection
δ_t	=	Throttle input
l	=	Roll moment
m	=	Pitch moment
n	=	Yaw moment
C_D	=	Aerodynamic drag coefficient
C_S	=	Aerodynamic side force coefficient
C_L	=	Aerodynamic lift coefficient
C_l	=	Aerodynamic roll moment coefficient
C_m	=	Aerodynamic pitch moment coefficient
C_n	=	Aerodynamic yaw moment coefficient
ζ	=	Icing level
$\boldsymbol{l}_k$	=	Point of attack on the left wing
$\boldsymbol{r}_k$	=	Point of attack on the right wing
$\boldsymbol{x}$	=	MRAC system state
$\boldsymbol{u}$	=	MRAC control input
$\boldsymbol{A}$	=	MRAC system matrix
$\boldsymbol{B}$	=	MRAC control matrix
$\boldsymbol{\Phi}(\boldsymbol{x})$	=	MRAC regressor vector
$\boldsymbol{P}$	=	Solution to the Lyapunov equation
$\boldsymbol{\Gamma}_*$	=	Adaptive rate
k_{p_*}	=	PID proportional gain
k_{i_*}	=	PID integral gain
k_{d_*}	=	PID derivative gain

*MSc. student, Department of Engineering Cybernetics, Norwegian University of Science and Technology (NTNU), Trondheim, Norway
†Researcher, Department of Engineering Cybernetics, Norwegian University of Science and Technology (NTNU), Trondheim, Norway
‡Researcher, Department of Engineering Cybernetics, Norwegian University of Science and Technology (NTNU), Trondheim, Norway
§Professor, Department of Engineering Cybernetics, Norwegian University of Science and Technology (NTNU), Trondheim, Norway

II. Introduction

To widen the scope of admissible operations for the UAV, research is going into how the UAVs can handle different meteorological conditions. One of these conditions is flight in atmospheric icing conditions, which is the topic for this paper.

Icing is a debilitating factor to a UAV as it the increases drag, reduces the lift, and increases the risk of stalling [1]. These factors elicit the need for increased control efforts to maintain flight. Additionally, ice accretion or run-back icing on the wing surface ahead of control surfaces results in reduced control surface effectiveness [2]. Smaller aircraft, such as UAVs, are more sensitive to icing conditions compared to larger manned aircraft [3]. One way to handle icing conditions is using ice protection systems [4], that consist of *anti-icing* to prevent ice accretion, or *de-icing* to remove already formed ice. These systems necessitate an increase in power consumption and preferably knowledge of the icing level to optimize the ice removal and its energy consumption. The problem of automatic icing detection is still a research question. This is of more concern for UAVs than larger manned aircraft as UAVs must rely entirely on onboard sensors and instruments to detect icing, whereas larger manned aircraft have a pilot onboard that can identify icing conditions [5].

One approach is to combine the use of de-icing systems and controllers that can cope with the adverse effects of icing, thereby increasing the de-icing intervals and potentially reducing the associated energy consumption. Previous work has been done by Kleiven *et al.* [6] with the development of robust controllers in icing conditions for the fixed-wing Skywalker X8 UAV. In this paper, an adaptive control approach is explored for the Skywalker X8.

Adaptive control is a control scheme where the control law changes as an adaptive law attempts to estimate the parameters that characterize the system [7]. In this paper, an inner loop model reference adaptive control (MRAC) scheme is developed for attitude control. Model reference adaptive control is based on finding a feedback controller, such that the system output tracks a commanded reference, in the presence of unknown plant parameters. Similar research has been performed to test MRAC schemes on UAVs [8, 9].

Chowdhary presents in [8] an MRAC scheme for a fixed-wing UAV that has been subject to asymmetric structural damage. This motivates the development of an MRAC controller for operation in asymmetric icing conditions.

The controllers in this paper are tested in a simulation model in MATLAB/Simulink, wherein the model is based on the model data from the work of Winter *et al.* [10], with the extension to an asymmetric model from Kleiven *et al.* [6]. The aerodynamic coefficient data from [10] are given for iced and clean (no icing) airfoils. The icing data in [10] is found for the mixed icing case, being the most severe icing type of the three types – glaze, rime, and mixed – concerning aerodynamic performance. Since the aerodynamic coefficients are based on symmetric icing levels, there are some uncertainties in the model when extending it to an asymmetric icing model. However, it is assumed to give an adequate reflection of the UAV's behavior with respect to the control aspect and the dynamics of ice accretion and shedding [6]. As such, the model is assumed to be valid for this paper. Ice accretion on the propellers can have significant consequences on thrust generation [11]. However, ice accretion on the propellers is not considered in this paper.

This paper aims to answer the question of whether an adaptive solution is better suited to tackle the problem of controlling UAVs in icing conditions than a more conventional PID controller. Additionally, the paper aims to explore if one could infer any valuable knowledge about the icing conditions.

III. Aerodynamic Model

The aerodynamic model in this paper is described by a quasi-linear approximation of the aerodynamic coefficients,

$$\begin{bmatrix} F_{\text{drag}} \\ F_{\text{side}} \\ F_{\text{lift}} \end{bmatrix} = \bar{q}S \begin{bmatrix} C_D(\alpha) + C_{D_q}(\alpha)\frac{c}{2V_a}q + C_{D_{\delta_e}}\delta_e \\ C_S(\beta) + C_{S_p}(\beta)\frac{b}{2V_a}p + C_{S_r}(\beta)\frac{b}{2V_a}r + C_{S_{\delta_a}}\delta_a + C_{S_{\delta_r}}\delta_r \\ C_L(\alpha) + C_{L_q}(\alpha)\frac{c}{2V_a}q + C_{L_{\delta_e}}\delta_e \end{bmatrix}, \tag{1}$$

$$\begin{bmatrix} l \\ m \\ n \end{bmatrix} = \bar{q}S \begin{bmatrix} b\big(C_l(\beta) + C_{l_p}(\beta)\frac{b}{2V_a}p + C_{l_r}(\beta)\frac{b}{2V_a}r + C_{l_{\delta_a}}\delta_a + C_{l_{\delta_r}}\delta_r\big) \\ c\big(C_m(\alpha) + C_{m_q}(\alpha)\frac{c}{2V_a}q + C_{L_{\delta_e}}\delta_e\big) \\ b\big(C_n(\beta) + C_{n_p}(\beta)\frac{b}{2V_a}p + C_{n_r}(\beta)\frac{b}{2V_a}r + C_{n_{\delta_a}}\delta_a + C_{n_{\delta_r}}\delta_r\big) \end{bmatrix}, \tag{2}$$

where $\bar{q} = \frac{\rho V_a^2}{2}$. The nonlinear aerodynamic coefficients in eqs. (1) and (2) are interpolated values for a given angle of attack or sideslip based on aerodynamic data for the Skywalker X8 fixed-wing UAV found by Winter *et al.* [10]. Following the notation of Kleiven *et al.* in [6], the variable $\zeta \in [0, 1]$ is used to describe the level of icing. For the clean case $\zeta = 0$ and for the fully iced case $\zeta = 1$. The aerodynamic coefficients, C_k, are then found with linear interpolation

as

$$C_k(\zeta) = \zeta\ C_{k,\text{iced}} + (1-\zeta)\ C_{k,\text{clean}}. \tag{3}$$

A. Extension to an Asymmetric Model

In [6], Kleiven *et al.* extended the symmetric model of the aircraft to an asymmetric model for the purpose of simulating asymmetric icing on the wings. The asymmetric model divides the aircraft into two parts, a left side and a right side. The asymmetry enters through the aerodynamic forces and moments. The total force acting through the center of mass of the aircraft is given by

$$\boldsymbol{F}_k = \boldsymbol{F}_{k,r} + \boldsymbol{F}_{k,l}, \tag{4}$$

where k is D, L or S, denoting the drag force, lift force and side force, respectively. The subscripts r and l denote the right and left side of the aircraft, respectively.

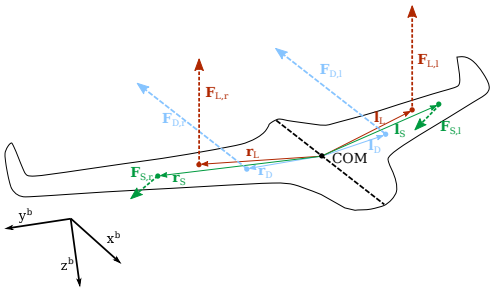

Figure 1 The forces of the asymmetric icing model. Courtesy of Kleiven [6].

The asymmetric aerodynamic moment is given in [6] by

$$\boldsymbol{m}_{a,\text{asym}} = \boldsymbol{m}_{a,0} + \sum_k (\boldsymbol{r}_k \times \boldsymbol{F}_{k,r} + \boldsymbol{l}_k \times \boldsymbol{F}_{l,r}) \quad \text{for } \boldsymbol{F}_{k,r}, \boldsymbol{F}_{k,l} \notin \boldsymbol{m}_{a,0}, \tag{5}$$

where $\boldsymbol{m}_{a,0}$ is a vector containing the symmetric moments l, m and n from eq. (2). The second term in eq. (5) is due to asymmetry in the corresponding aerodynamic forces on the left and right wing. The asymmetric forces are depicted in Fig. 1. The following assumptions are made by Kleiven *et al.* [6] with respect to the point of attack of the aerodynamic forces

- All points of attack are assumed to lie on the $\pm y$-axis.
- The icing level does not affect the points of attacks' y-coordinate.

IV. Icing

Atmospheric ice accretion on an aircraft can have a critical impact on the aerodynamics, causing a decrease in lift, an increase in drag, and reduced stall limit [2]. The stall limit is lowered as the ice formed on the airfoil causes the airflow to separate from the airfoil at a lower angle of attack. Moreover, the changes in lift and drag, imply that a greater thrust force is needed to compensate for the effects of icing. Hann *et al.* [3] shows that the smaller fixed-wing UAVs, compared to the larger and faster manned aircraft, are more affected by the ice accretion.

The three main types of icing conditions are glaze, rime, and mixed ice, wherein mixed icing lies in between the glaze and rime categorizations. Glaze ice occurs at temperatures from 0°C to −3°C, and they tend to have a rough surface and double horns, while rime ice occurs at temperatures below −10°C and tend to have a single horn and a relatively smooth surface [2]. By the findings of Hann in [12] mixed icing is considered the most severe type of icing condition concerning the degradation in aerodynamic effectiveness. [12] also shows that for the mixed icing the curve for the aerodynamic lift coefficient is shifted to the left. As a consequence, either the velocity of the UAV or the angle of attack must be increased to maintain its position in the flight envelope [12].

There are two main methods of icing protection to cope with ice accretion on the leading edge of the airfoil, namely de-icing and anti-icing methods. Anti-icing consists of continuously applying heat to the airfoils to prevent any icing from forming, whereas de-icing consists of periodically applying heat to remove already formed ice. Both require an increase in power consumption, although [4] suggests that anti-icing demands higher energy usage than de-icing in many conditions.

Further, ice accretion on the airfoils ahead of control surfaces such as ailerons, elevators, and rudders also results in a reduced control surface effectiveness [2]. The severity of the loss in control effectiveness is governed by three fluid dynamic properties described in [2]. In [6, 10], the icing is assumed to be on the leading edge only, and that the control surface on the trailing edge were unaffected by icing.

Through computational fluid dynamics (CFD) simulations, an estimate of the reduced control surface effectiveness due to icing on the airfoil is found for the longitudinal aerodynamics. The simulations are done with the ANSYS FENSAP-ICE simulation software and the method is described in the Appendix of this paper.

The analysis shows that the value of the aerodynamic coefficient $C_{L_{\delta_e}}$ is reduced by 27% from the clean to iced case, $C_{D_{\delta_e}}$ is increased by 86% and $C_{m_{\delta_e}}$ is reduced by 37%. Assuming that roll is only a function of the lift differential between the wings, and that yaw is only a function of the drag difference, the effects of reduced control surface effectiveness are incorporated into the lateral dynamics. Accordingly, the aerodynamic coefficient $C_{l_{\delta_a}}$ is reduced by 27% from the clean to iced case and $C_{n_{\delta_a}}$ is increased by 86%. It is noted that the CFD analysis is only used to determine the reduction in control effectiveness due to icing, while the rest of the model is the same as in Kleiven et al. [6].

V. Controller Design

A. Inner Loop Model Reference Adaptive Control

Based on Lavretsky and Wise [9], a model reference adaptive control scheme is developed for the UAV. Consider the nonlinear system

$$\dot{\boldsymbol{x}} = \boldsymbol{A}\boldsymbol{x} + \boldsymbol{B}\boldsymbol{\Lambda}(\boldsymbol{u} + f(\boldsymbol{x})), \tag{6}$$

where $\boldsymbol{x} \in \mathbb{R}^n$ is the state vector, $\boldsymbol{u} \in \mathbb{R}^m$ is the control input, $\boldsymbol{B} \in \mathbb{R}^{n\times m}$ is the known control matrix, $\boldsymbol{\Lambda} \in \mathbb{R}^{m\times m}$ is the unknown control effectiveness matrix and $\boldsymbol{A} \in \mathbb{R}^{n\times n}$ is the unknown state matrix. It is assumed that $f(\boldsymbol{x})$ can be written as

$$f(\boldsymbol{x}) = \boldsymbol{\Theta}^\top \Phi(\boldsymbol{x}), \tag{7}$$

where $\boldsymbol{\Theta} \in \mathbb{R}^{N\times m}$ is constant and unknown, and $\boldsymbol{\Phi}(\boldsymbol{x}) \in \mathbb{R}^N$ is the known regressor vector consisting of N locally Lipschitz-continuous basis functions [9]. The matrices $\boldsymbol{A}$ and $\boldsymbol{\Lambda}$ are assumed constant, and $\boldsymbol{\Lambda}$ is assumed to be diagonal with its elements $\lambda_i > 0$. Additionally, it is assumed that the pair $(\boldsymbol{A}, \boldsymbol{B\Lambda})$ is controllable.

The control objective of the model reference adaptive controller is to have the system state in eq. (6) track the reference model

$$\dot{\boldsymbol{x}}_{\text{ref}} = \boldsymbol{A}_{\text{ref}}\boldsymbol{x}_{\text{ref}} + \boldsymbol{B}_{\text{ref}}\boldsymbol{r}(t), \tag{8}$$

driven by the commanded reference, $\boldsymbol{r}(t)$. The matrix is $\boldsymbol{A}_{\text{ref}} \in \mathbb{R}^{n\times n}$ is Hurwitz and $\boldsymbol{B}_{\text{ref}} \in \mathbb{R}^{n\times m}$ is the input matrix.

Tracking of the reference model is achieved with the control law

$$\boldsymbol{u} = \hat{\boldsymbol{K}}_{\boldsymbol{x}}{}^\top \boldsymbol{x} + \hat{\boldsymbol{K}}_{\boldsymbol{r}}{}^\top \boldsymbol{r} - \hat{\boldsymbol{\Theta}}^\top \boldsymbol{\Phi}(\boldsymbol{x}), \tag{9}$$

where $\hat{\boldsymbol{K}}_{\boldsymbol{x}} \in \mathbb{R}^{n\times m}$, $\hat{\boldsymbol{K}}_{\boldsymbol{r}} \in \mathbb{R}^{m\times m}$ and $\hat{\boldsymbol{\Theta}} \in \mathbb{R}^{N\times m}$ are controller gain matrices that will ensure tracking of the reference model dynamics and render the closed-loop error dynamics uniformly stable. The adaptive law for the controller gains are found through Lyapunov analysis in [9] and are given as,

$$\begin{aligned}
\dot{\hat{\boldsymbol{K}}}_x &= \text{Proj}(\hat{\boldsymbol{K}}_x,\ -\boldsymbol{\Gamma}_{\boldsymbol{x}}\boldsymbol{x}\boldsymbol{e}^\top\boldsymbol{P}\boldsymbol{B}),\\
\dot{\hat{\boldsymbol{K}}}_r &= \text{Proj}(\hat{\boldsymbol{K}}_r,\ -\boldsymbol{\Gamma}_{\boldsymbol{r}}\boldsymbol{r}\boldsymbol{e}^\top\boldsymbol{P}\boldsymbol{B}),\\
\dot{\hat{\boldsymbol{\Theta}}} &= \text{Proj}(\hat{\boldsymbol{\Theta}},\ \boldsymbol{\Gamma}_{\boldsymbol{\Theta}}\boldsymbol{\Phi}\boldsymbol{e}^\top\boldsymbol{P}\boldsymbol{B}),
\end{aligned} \tag{10}$$

where $\boldsymbol{\Gamma}_x = \boldsymbol{\Gamma}_x^\top > 0$, $\boldsymbol{\Gamma}_r = \boldsymbol{\Gamma}_r^\top > 0$ and $\boldsymbol{\Gamma}_\Theta = \boldsymbol{\Gamma}_\Theta^\top > 0$ are the adaptation rates, $\boldsymbol{e} = \boldsymbol{x} - \boldsymbol{x}_{\text{ref}}$, and where Proj$(\cdot)$ is the projection operator as defined in [9]. The matrix $\boldsymbol{P} = \boldsymbol{P}^\top > 0$ satisfies the algebraic Lyapunov equation

$$\boldsymbol{P}\boldsymbol{A}_{\text{ref}} + \boldsymbol{A}_{\text{ref}}^\top\boldsymbol{P} = -\boldsymbol{Q}, \tag{11}$$

for $\boldsymbol{Q} = \boldsymbol{Q}^\top > 0$.

1. Model equations

The model in the MRAC control scheme is chosen as a linear model with the addition of a bias term to capture nonlinear and unmodelled effects. From Beard & McLain [13], a linearization of the roll dynamics is given as

$$\begin{aligned}
\dot{\phi} &= p + d_{\phi_1},\\
\ddot{\phi} &= -a_{\phi_1}\dot{\phi} + a_{\phi_2}\delta_a + d_{\phi_2},
\end{aligned} \tag{12}$$

where d_{ϕ_1} and d_{ϕ_2} consists of the unmodeled and nonlinear terms of the dynamics and are, for the linear model, considered as disturbances on the system. A model of the roll dynamics using eq. (12) is then given by

$$\begin{aligned} \dot{\boldsymbol{x}} &= \boldsymbol{A}\boldsymbol{x} + \boldsymbol{B}\boldsymbol{\Lambda}(\boldsymbol{u} + \boldsymbol{\Theta}^\top \boldsymbol{\Phi}(\boldsymbol{x})), \\ \begin{bmatrix} \dot{\phi} \\ \dot{p} \end{bmatrix} &= \begin{bmatrix} 0 & 1 \\ 0 & a_1 \end{bmatrix} \begin{bmatrix} \phi \\ p \end{bmatrix} + \begin{bmatrix} 0 \\ 1 \end{bmatrix} \lambda_1 \Big(\delta_a + \begin{bmatrix} \theta_{\text{bias, roll}} \end{bmatrix} \begin{bmatrix} 1 \end{bmatrix} \Big), \end{aligned} \tag{13}$$

where $a_1 = -a_{\phi_1}$, $\lambda_1 = a_{\phi_2}$, $\theta_{\text{bias, roll}} = d_{\phi_2}$, and the pair $(\boldsymbol{A}, \boldsymbol{B}\boldsymbol{\Lambda})$ is controllable since the matrix $[\boldsymbol{B}\boldsymbol{\Lambda} \;\; \boldsymbol{A}\boldsymbol{B}\boldsymbol{\Lambda}]$ is of full rank for all $a_{\phi_2} \neq 0$.

Similarly, a linearization of the pitch dynamics is given by Beard & McLain [13] as

$$\dot{\theta} = q + d_{\theta_1}, \tag{14}$$

$$\ddot{\theta} = -a_{\theta_1}\dot{\theta} - a_{\theta_2}\theta + a_{\theta_3}\delta_e + d_{\theta_2}, \tag{15}$$

which gives the pitch model of the same form

$$\begin{aligned} \dot{\boldsymbol{x}} &= \boldsymbol{A}\boldsymbol{x} + \boldsymbol{B}\boldsymbol{\Lambda}(\boldsymbol{u} + \boldsymbol{\Theta}^\top \boldsymbol{\Phi}(\boldsymbol{x})), \\ \begin{bmatrix} \dot{\theta} \\ \dot{q} \end{bmatrix} &= \begin{bmatrix} 0 & 1 \\ a_2 & a_3 \end{bmatrix} \begin{bmatrix} \theta \\ q \end{bmatrix} + \begin{bmatrix} 0 \\ 1 \end{bmatrix} \lambda_2 \Big(\delta_e + \begin{bmatrix} \theta_{\text{bias, pitch}} \end{bmatrix} \begin{bmatrix} 1 \end{bmatrix} \Big), \end{aligned} \tag{16}$$

where $a_2 = -a_{\theta_2}$, $a_3 = -a_{\theta_1}$, $\lambda_2 = a_{\theta_3}$ and $\theta_{\text{bias, pitch}} = d_{\theta_2}$, and the pair $(\boldsymbol{A}, \boldsymbol{B}\boldsymbol{\Lambda})$ is controllable since the matrix $[\boldsymbol{B}\boldsymbol{\Lambda} \;\; \boldsymbol{A}\boldsymbol{B}\boldsymbol{\Lambda}]$ is of full rank for all $a_{\theta_3} \neq 0$.

The bias terms in the model in eqs. (13) and (16) act as a steady state compensation, similar to an integral term in a PID controller.

B. Inner Loop PID Controllers

The PID controller for roll is given by

$$\delta_a = k_{p_\phi}(\phi^c - \phi) + \frac{k_{i_\phi}}{s}(\phi^c - \phi) - k_{d_\phi} p,$$

where ϕ^c is the commanded roll angle and k_{p_ϕ}, k_{i_ϕ} and k_{d_ϕ} are the control gains.

Similarly, the PID controller for pitch is given by

$$\delta_e = k_{p_\theta}(\theta^c - \theta) + \frac{k_{i_\theta}}{s}(\theta^c - \theta) - k_{d_\theta} q, \tag{17}$$

where θ^c is the commanded pitch angle and k_{p_θ}, k_{i_θ}, and k_{d_θ} are the control gains. This deviates from the pitch controller presented in [13], where the inner control loop in pitch does not include an integral term. This design choice of Beard & McLain [13] is to avoid limiting the bandwidth of the inner loop, based on the assumption that outer loop controllers will compensate for the steady state offset in pitch. In this paper, a key aspect is comparing the inner loop controllers of the MRAC and PID controllers without outer loop. As such, an integral term in the pitch control loop is added to compensate for a steady state offset in pitch.

The controller gains are given in table 2 in the Appendix.

C. Airspeed controller

The PI controller for airspeed control using throttle is given by [13]

$$\delta_t = \delta_t^* + k_{p_V}(V_a^c - V_a) + \frac{k_{i_V}}{s}(V_a^c - V_a), \tag{18}$$

where δ_t^* is the throttle trim value, and k_{p_V}, k_{i_V} are the control gains. The airspeed controller is used in both the PID and MRAC control schemes.

VI. Simulation Results

In this section, the simulation results are presented. The main limitations of the simulator are uncertainties related to the interpolation of the aerodynamic coefficients, and uncertainties concerning the extension to an asymmetric model. Additionally, stalling behavior is not implemented in the simulator. Consequently, every test run must be evaluated after running a simulation to assess if the angle of attack is within realistic values.

The icing level timeseries chosen for the simulations in Figs. 3, 4, and 7 is chosen to explore the response of the system under different icing configurations. The timeseries simulates the asymmetric build-up of icing, followed by de-icing of the right wing, a period of severe asymmetric icing, and finally de-icing of the left wing. Severe asymmetric icing refers to one wing being fully iced, while the other is clean.

The first 100 seconds of the simulations (not shown) the MRAC is excited by a signal consisting of a sum of sinusoids, to ensure that its internal states and parameters have converged to a suitable tuning before the icing events.

A. Tuning of MRAC

The solution, $\boldsymbol{P}$, to the Lyapunov equation in eq. (11) is included in each of the adaptive laws in eq. (10). Since the solution is given by

$$\boldsymbol{P} = \begin{bmatrix} \frac{q_2\omega_n^2+q_1+4q_1\zeta^2}{4\omega_n\zeta} & \frac{q_1}{2\omega_n^2} \\ \frac{q_1}{2\omega_n^2} & \frac{q_2\omega_n^2+q_1}{(q_2\omega_n^2+q_1)/(4\omega_n^3\zeta)} \end{bmatrix}, \tag{19}$$

where $\boldsymbol{Q}$ is chosen as

$$\boldsymbol{Q} = \begin{bmatrix} q_1 & 0 \\ 0 & q_2 \end{bmatrix},$$

and $\boldsymbol{A}_{\text{ref}}$ is chosen as

$$\boldsymbol{A}_{\text{ref}} = \begin{bmatrix} 0 & 1 \\ -\omega_n^2 & -2\zeta\omega_n \end{bmatrix},$$

the reference model and the choice of $\boldsymbol{Q}$ will affect all adaptations, $\hat{\boldsymbol{K}}_x$, $\hat{\boldsymbol{K}}_r$ and $\hat{\boldsymbol{\Theta}}$.

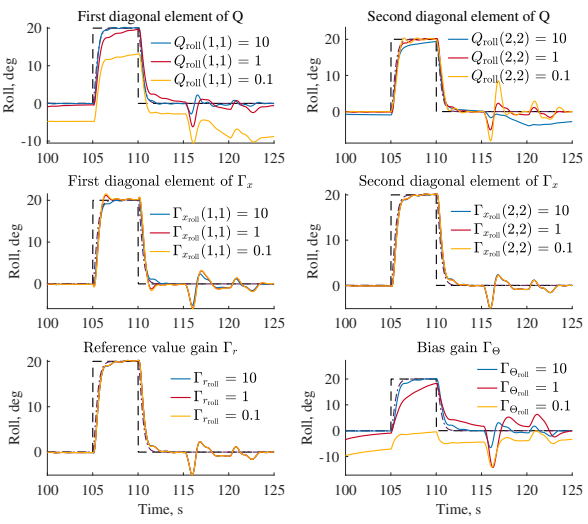

(a) The roll controller. From $t = 115$s to $t = 120$s the pitch reference (not shown) is set to $20°$.

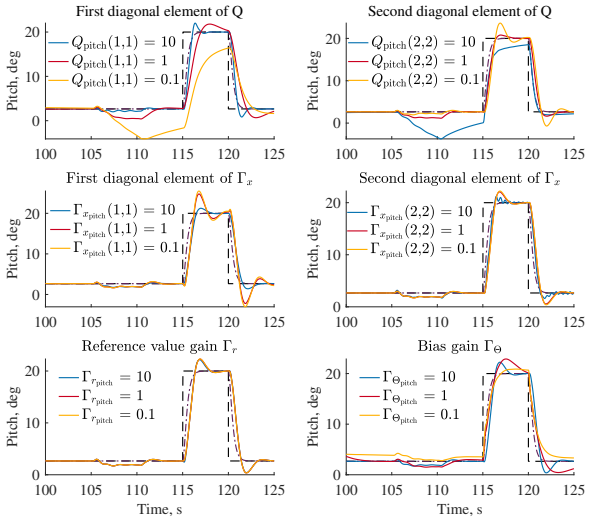

(b) The pitch controller. From $t = 105$s to $t = 110$s the roll reference (not shown) is set to $20°$.

Figure 2 The effect of each of the adaptive rates. The icing level is set to $(\zeta_{\text{left}}, \zeta_{\text{right}}) = (0.8,\ 0.3)$.

Figures 2a and 2b illustrate how each adaptive rate affects the response of the systems. In each sub-figure a simulation is run with one adaptive rate set to the values $\{10, 1, 0.1\}$, while the other rates are constant. The adaptive rate in question for each sub-figure is given by the legend and title.

The value of the first diagonal element of the $\boldsymbol{Q}$-matrix, q_1, is seen in the upper left plot of Figs. 2a and 2b to have a significant impact on the tracking performance for both the roll and pitch controllers. This is expected as q_1 is present in every element of $\boldsymbol{P}$ given in eq. (19), wherein $\boldsymbol{P}$ is present in each of the adaptive laws in eq. (10).

Secondly, the adaptive rates $\boldsymbol{\Gamma}_x$ and $\boldsymbol{\Gamma}_r$ have considerably less impact on the response for both the roll and pitch controller. The central right plot in Fig. 2b shows, however, that an increase in the second diagonal element of $\boldsymbol{\Gamma}_x$ of the pitch controller leads to oscillations. With more aggressive pitch references and with increased asymmetry of the icing levels, these oscillations become more pronounced. As such, this gain value was chosen to be quite low.

Finally, Fig. 2a shows that the adaptive rate of the bias term in roll has a significant impact on the tracking performance. As mentioned in section V.A.1, the bias term acts as a steady state compensation. Likely. the term compensates for the additional roll moment produced by asymmetric icing levels, and thus plays a critical role in the tracking performance.

Overall, to avoid oscillations in the system states, the adaptive rates were chosen as small as possible while still ensuring adequate performance. The adaptive rates are given in table 1 in the Appendix.

B. Baseline Case

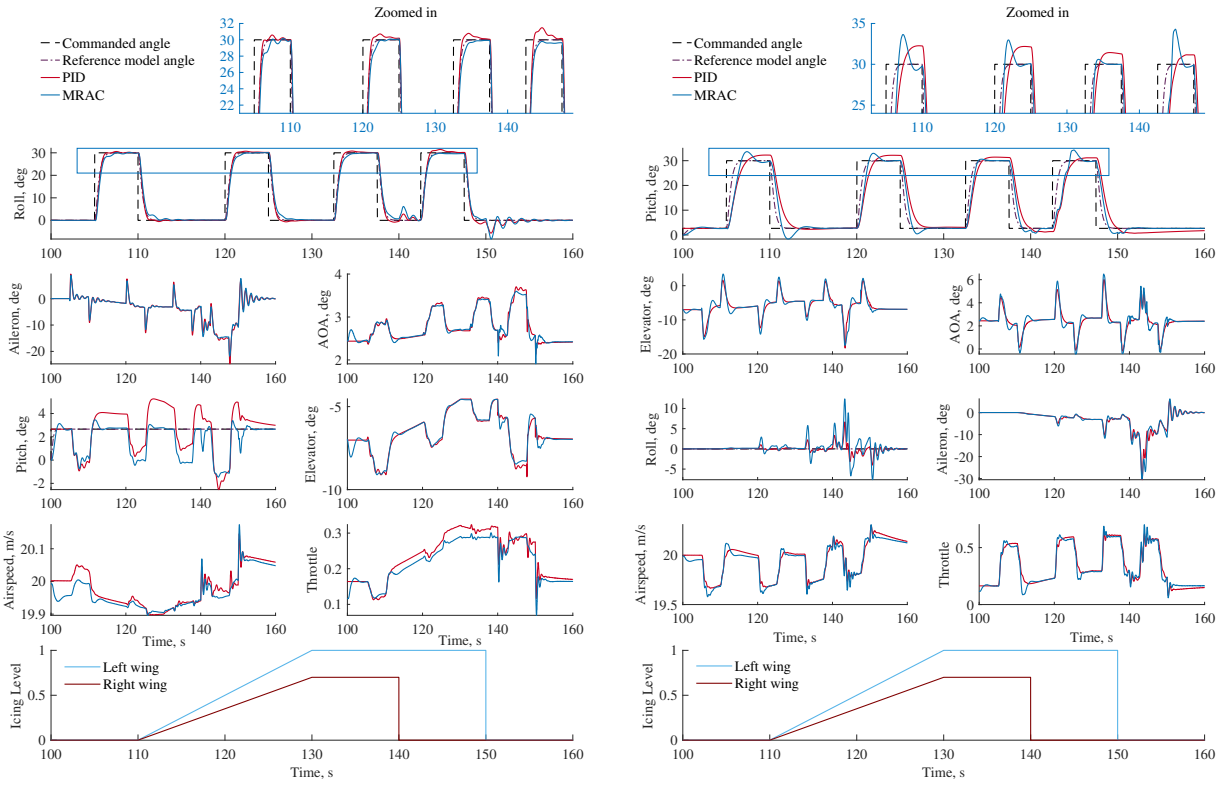

(a) Baseline simulation case with square reference signal in roll.

(b) Baseline simulation case with square reference signal in pitch.

Figure 3 The response of the baseline case with the adaptive controller and the PID controller is shown.

The baseline simulation case in Figs. 3a and 3b shows the response of the system with the MRAC and PID controllers run with a square reference in roll and pitch, respectively. The results show that both controllers perform well under different icing conditions with relatively aggressive reference angles in roll and pitch. Figure 3a shows an increase in throttle usage as the icing level increases, due to increased drag from the icing. The roll response in Fig. 3b shows an increase in the deviation from the zero degree roll reference as the simulation progresses.

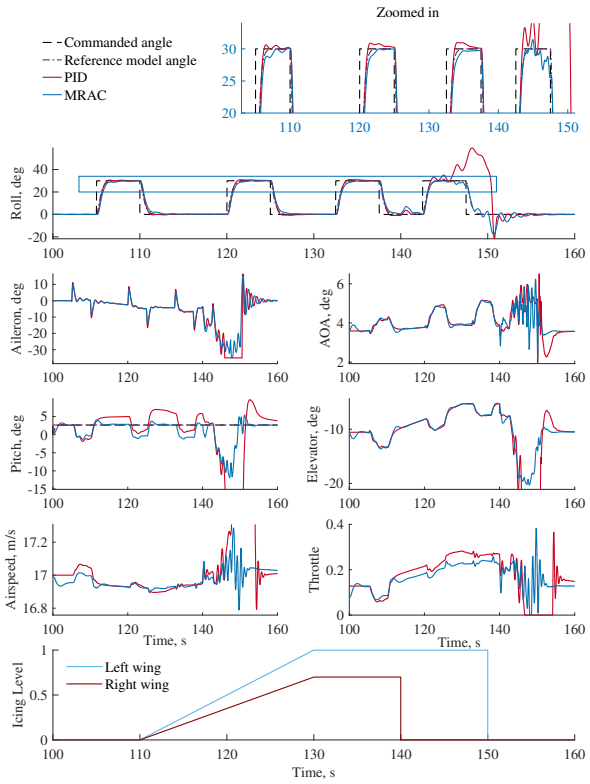

Figure 4 The response of the reduced airspeed case with $V_a = 17$m/s for the adaptive controller and the PID controller is shown.

C. Reduced airspeed

Figure 4 shows the response with the adaptive controller and the PID controller for the baseline case in Fig. 4 with the airspeed reduced from 20m/s to 17m/s. It can be seen that for the most severe icing phase from $t = 140$s to $t = 150$s where the icing is 100% asymmetric, the PID controller is not able to follow the roll reference. The roll angle reaches a maximum of 59° at $t \approx 148$s.

A simulation with the roll reference angle increased from $\phi_{\text{cmd}} = 30°$ to $\phi_{\text{cmd}} = 40°$ results in similar behavior for the adaptive controller as the PID controller in Fig. 4.

D. Reduced Control Surface Effectiveness

In Fig. 5 the system is simulated with a square reference signal in pitch using the reduced control surface efficiency found in the CFD analysis described in section IV. The results from applying this data is labeled "Reduction 1".

Additionally, a simulation with an even further reduction in the control surface effectiveness is run to test robustness, labeled "Reduction 2". The values for this simulation is given as follows: $C_{L_{\delta_e}}$ and $C_{l_{\delta_a}}$ are reduced by 50% from the clean to iced case, $C_{D_{\delta_e}}$ and $C_{n_{\delta_a}}$ are increased by 150% and $C_{m_{\delta_e}}$ is reduced by 50%.

Figure 5b shows that as the icing level increases, the response with the PID controller differs only slightly between the three levels of control surface effectiveness, indicating that the control effectiveness does not have any significant effect on the performance of the PID controller within this simulator framework. The adaptive controller in Fig. 5a experiences some increased overshoots in pitch and increased roll deviations with the reduction in control surface effectiveness.

Note how any significant deviation from the roll reference only occurs at $t \in (120, 140)$s, which coincides with asymmetric icing levels. When the icing level is symmetric with $\zeta = 0$ or $\zeta = 1$, the roll angle is much closer to its zero degree reference. A likely cause of this is that with asymmetric icing on the wings an additional roll moment is induced, throwing the UAV's balance off. As the icing level becomes symmetric again from $t = 143$s, the roll deviations diminish.

In Fig. 6 the system is simulated under the same conditions with reduced control surface effectiveness as described

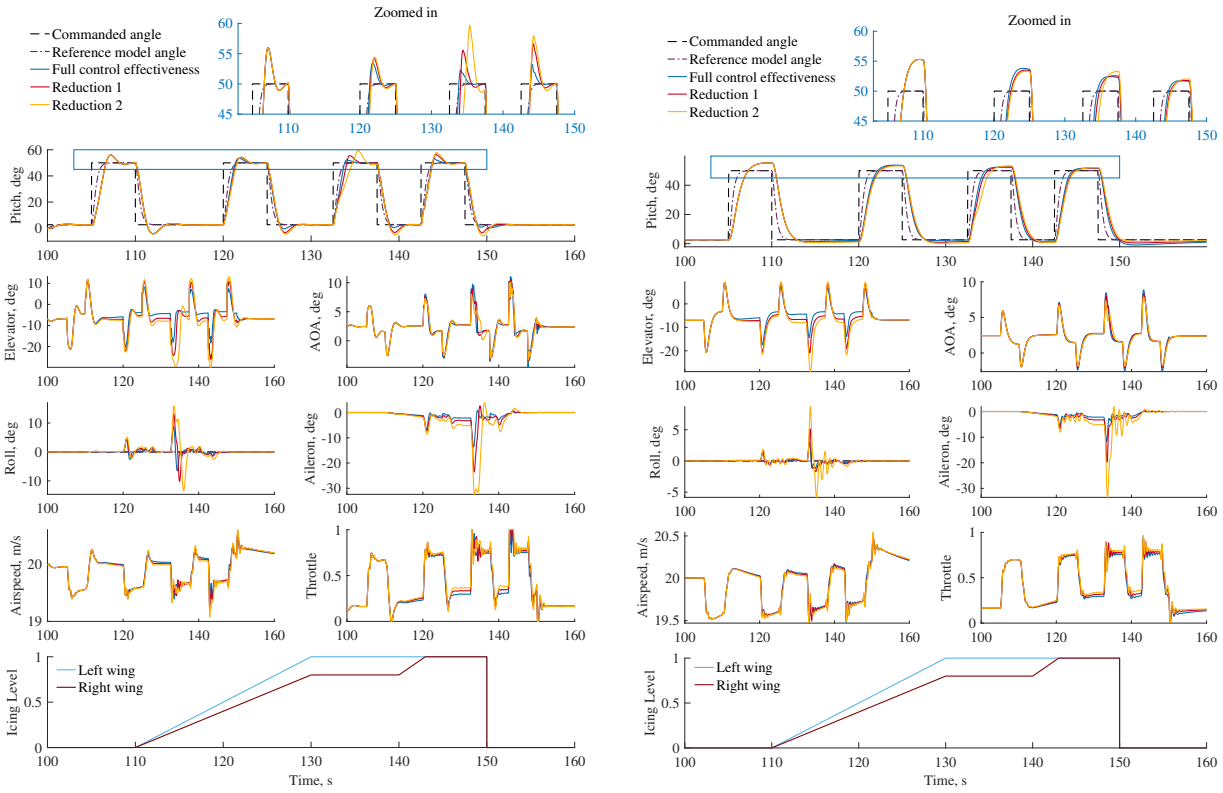

(a) Response with the MRAC controller. **(b) Response with the PID controller.**

Figure 5 Reduced control surface effectiveness simulation case with a 50° square reference signal in pitch. The response with with full control surface effectiveness, reduced control surface effectiveness according to the data of CFD simulations, and a case with a further reduction in control surface effectiveness is shown.

earlier in this section, with a square reference in roll instead of pitch.

The PID controller experiences increased deviations from the roll reference as the icing levels increase, whereas the MRAC controller appears less affected by the reduced control surface effectiveness.

E. Bias and Integral Terms

Figures 7a and 7b show a simulation case intended to investigate the bias terms of the adaptive controller and the integral terms of the PID controller. The motivation behind this simulation case is to examine whether the bias terms or the integral terms can detect the effects of the icing.

The first simulation in Fig. 7a (in blue) shows the response with the so-called "Original tuning", which corresponds to the tuning values of the adaptive controller given in table 1 in the Appendix. For the simulation labeled "Slower adaptation of bias" (in red) the adaptive rates of the bias terms have been lowered from $\Gamma_\Theta = 15$ to $\Gamma_\Theta = 1$ for the roll controller, and from $\Gamma_\Theta = 10$ to $\Gamma_\Theta = 1$ for the pitch controller. With the slower adaptive rate for the bias term, it is seen from Fig. 7a that the bias term, especially in roll, appears to follow the differential icing level. With the faster rate (in blue), the bias appears to be more influenced by the sideslip angle and angle of attack.

Similarly, the simulation labeled "Original tuning" (in blue) in Fig. 7b is run with the tuning values of the PID controller given in table 2 in the Appendix. For the simulation labeled "Alternative tuning" (red), the integral terms are changed from $k_{i_\phi} = 2$ to $k_{i_\phi} = 0.5$, and $k_{i_\theta} = -0.1$ to $k_{i_\theta} = -0.3$. The tuning values of the "Alternative tuning" case were found by attempting to tune the integral terms to closer match the differential and sum of the icing level. The integral term in roll was lowered, resulting in less peaks from $t = 100$s to $t = 135$s. However, that also resulted in a slower response in the integral term during the largest peak in the differential icing level at $t \in (135, 145)$s. The integral term in pitch in Fig. 7b is increased slightly from its "original" tuning as the integral term looked to be too slow to

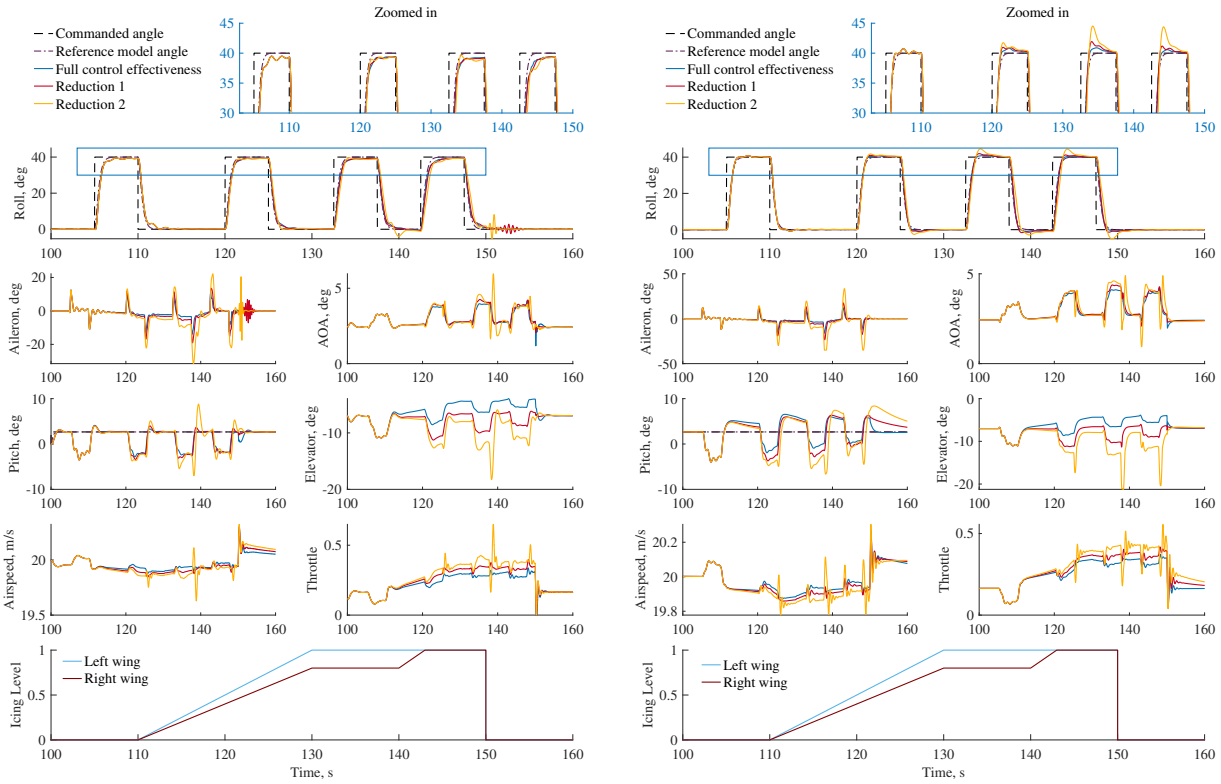

(a) Response with the MRAC controller. **(b) Response with the PID controller.**

Figure 6 Reduced control surface effectiveness simulation case with a 40° square reference signal in roll. The response with with full control surface effectiveness, reduced control surface effectiveness according to the data of CFD simulations, and a case with a further reduction in control surface effectiveness is shown.

capture the sum of the icing levels. However, neither increasing nor decreasing k_{i_θ} resulted in significantly increased similarity to the sum of the icing levels.

VII. Discussion

A. Stalling

For the simulations in this paper, the modelling by Winter *et al.* [10] and the extension to an asymmetric aerodynamic model by Kleiven *et al.* [6] has been assumed to be valid. Winter *et al.* [10] suggests a stall limit in the fully iced case of $\alpha_{\text{stall}} \approx 10°$. However, the CFD analysis in section VIII.A, suggests that the stall limit is closer to $\alpha_{\text{stall}} \approx 4°$ in the fully iced case. The reason for this discrepancy could stem from the differences in the configurations in the CFD simulations from the configuration used in Winter et al., such as variations in chord length and hinge location, and the fact that the airfoil of the Skywalker X8 is unknown and that the two approximations may reflect different behaviour.

As mentioned in section IV, the CFD analysis is only used to find an estimate of the reduction in control surface effectiveness from the clean case to the fully iced case. Nevertheless, due to the great uncertainty in the stall limit for the iced case, the values of the angle of attack and stalling of the UAV have not been the focus in this paper. More work must be done to determine accurate ranges for the stall limit in icing.

B. Effects of icing

The results in section VI show that the 100% asymmetric icing case, i.e. when the left wing is fully iced and the right wing is clean, is the most severe icing case with respect to the performance of the controllers. The greater the asymmetry, the greater the coupling of the roll and pitch dynamics is. An example of the increase in coupling between

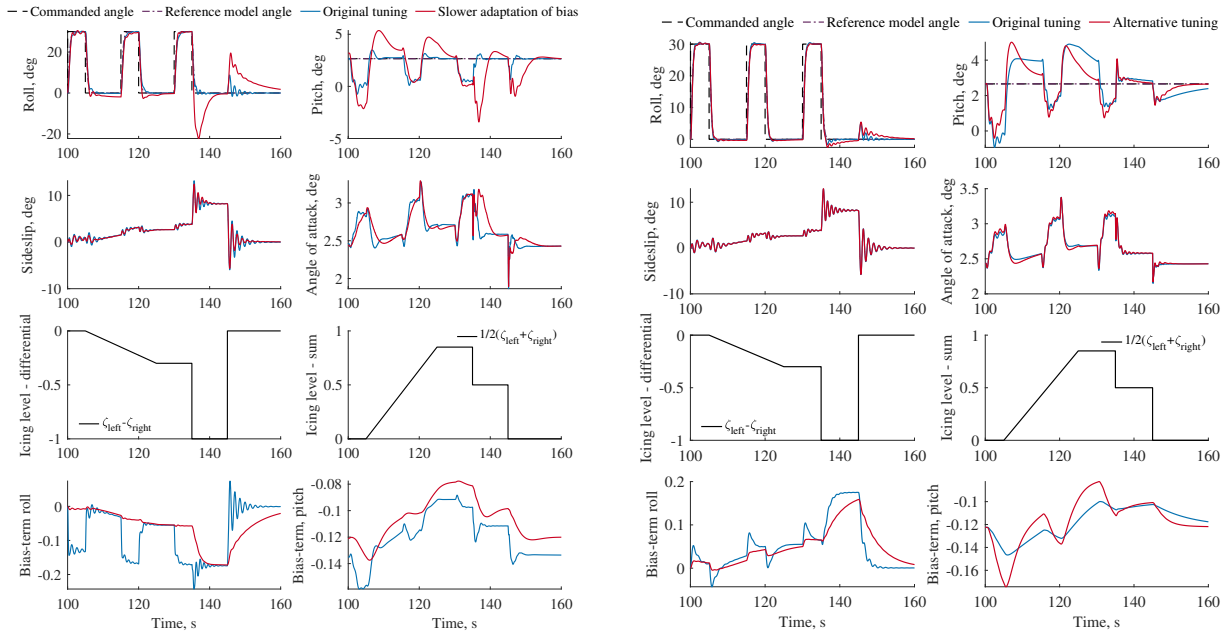

(a) MRAC controller. **(b) PID controller.**

Figure 7 The bias terms of the MRAC controller, and the integral terms of the PID controller.

the two states with increased asymmetry is observed as the deviations from the zero degree reference in roll during pitch deflections are larger for increased asymmetry, observed in Figs. 5b and 3b.

The reduced control surface effectiveness simulation case with a pitch angle reference in Fig. 5, shows that the pitch response with MRAC controller is more affected by the changes in control surface effectiveness than the PID controller. With the square roll angle reference in Fig. 6, the opposite is true, where the roll response with the PID controller is more affected by the changes in control surface effectiveness than the MRAC controller.

C. Bias and integral terms

From the examination of the bias terms in section VI.E, there is an indication that a bias term might be able to detect the icing levels of the airfoils. However, for faster adaptive rates the bias terms seem to also capture the effects of the sideslip angle and the angle of attack, and perhaps additional unmodelled effects.

Some further work on this might be able to produce an estimate of the icing levels, which would be very beneficial for the development of ice protection systems. Some paths forward with this could be modifying the MRAC model equations in an attempt to separate the icing effects from other unmodelled effects. During the design of the regressor, $\boldsymbol{\Phi}(\boldsymbol{x})$, one could choose to include compensating linear terms in the sideslip and angle of attack, and thereby infer the effect of these through their respective adaptive parameters. That is, setting $f(\boldsymbol{x})$ in eq. (7) to $[\theta_{\text{bias,roll}} \;\; \theta_\beta][1 \;\; \beta]^\top$ in the the roll model equations, and to $[\theta_{\text{bias,pitch}} \;\; \theta_\alpha][1 \;\; \alpha]^\top$ in the the pitch model equations. This would be especially pertinent seeing how these terms appear in the full equations of motion of an aircraft in [13]. In this paper, sideslip angle and angle of attack were deliberately not included in the regessor since these quantities are difficult to measure accurately for a UAV [14]. Nonetheless, a significant challenge in continuing down this path will be to produce a *reliable* estimate of the icing level across several atmospheric conditions and flight scenarios.

VIII. Conclusion

This paper has investigated inner loop adaptive control of the Skywalker X8 fixed-wing UAV in icing conditions. An MRAC control scheme has been implemented and its performance compared with a PID controller. The MRAC model was chosen as a linear model with a bias term to capture additional unmodelled effects. Through several simulation cases, it was found that the performance of the MRAC and PID were quite similar. However, the MRAC performs better

in the case of reduced airspeed for asymmetric icing levels. By modifying the tuning, the bias terms of the MRAC control scheme, and to some degree the integral terms of the PID controller, are able to capture the icing levels on the airfoils of the UAV.

Computational fluid dynamics analysis allowed for a realistic simulation of the reduced control surface effectiveness due to icing. The results show that the MRAC controller is less affected by the reduction in control surface efficiency than the PID control scheme with a square reference angle in roll, while the opposite is true with a square reference angle in pitch. There is uncertainty in the stall limit of the UAV in icing conditions, and consequently more work must be done to determine accurate ranges for the stall limit in icing.

As a concluding remark, it is noted that the MRAC control scheme is more complex and introduces more tuning parameters than the PID control scheme - while they prove similar performance, with the MRAC performing better under certain conditions as discussed in this paper. Additionally, with the increased complexity and the system identification aspect of the MRAC scheme comes the possibility of exploring icing level estimation.

Appendix

A. Control surface CFD icing simulations

The effect of ice accretions on control surface effectiveness was estimated using icing CFD methods. A series of simulations were performed with ANSYS FENSAP-ICE (version 2021 R1) in 2D on a reconstructed airfoil of the X8. The airfoil chord was set to 45cm with a flap hinge at 80% of the chord length and deflection angles of 0°, 10° and 20°.

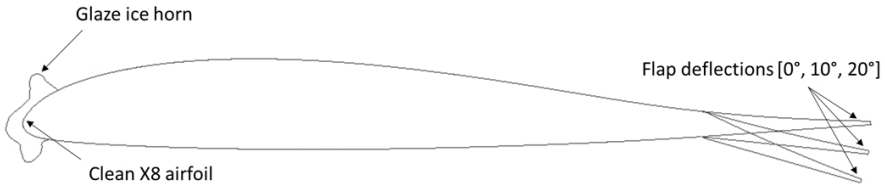

Figure 8 Cross section of the ice shape.

These geometries were generated for a clean (uniced) airfoil as baseline and an iced airfoil – resulting in a total of six geometries, see Fig. 8. The ice shape used for this case is based on an earlier work and represent a severe icing case with a very distinct horn [5]. While the ice shape was obtained using legacy methods, it can still be considered as a realistic case. It represents a severe glaze horn with a complex geometry, that is not unlike geometries that have been generated with more modern methods [3]. The ice shape can conditions can be interpreted as typical worst case scenario. For each of the six geometries, lift, drag, and moments were simulated over a range of angles of attack. The FENSAP-ICE simulations were conducted with a Spalart-Allmaras turbulence model with upwind artificial viscosity. More details about the numerical simulation parameters and meshing settings are described in previous work and were identical in this study [3].

The results for lift, drag, and moments over angle of attack are shown in Fig. 9. The results on the clean airfoils show the typical aerodynamic behavior of flaps. An increase of the flap deflection angle leads to an increase in lift, increase in drag, and reduction in stall angle. Since a flap deflection leads to additional lift generated near the trailing-edge of the airfoil, it generates additional nose-down moment. In principle, the same behavior occours for the iced airfoils. The largest difference is an substantially earlier onset of stall of the iced airfoils compared to the clean cases. The offset seems constant (i.e. independent from flap deflection angle) with a angle of attack difference of $-11°$. This behavior can be explained by the large leading-edge separation bubble that is induced by the ice horn, see Fig. 10. This separation bubble increases the turbulence in the downstream flow and substantially decreases its resistance against stall at even moderate angles of attack.

In addition to this earlier stall, the results in Fig. 9a also show that the iced airfoils generate less lift than the clean airfoil and also less additional lift per degree of flap deflection. Figure 9b shows that the iced airfoils generate substantially more drag compared to the clean airfoils. Also, the additional drag generated from the flaps is larger compared to clean airfoil flaps. In average, the flaps on the iced airfoil generate −27% less lift and +86% more drag

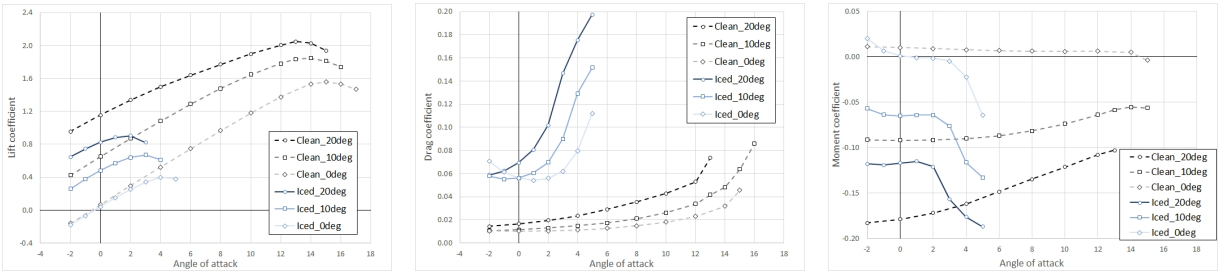

(a) Results for lift. **(b) Results for drag.** **(c) Results for moments.**

Figure 9 The results for lift, drag, and moments over angle of attack.

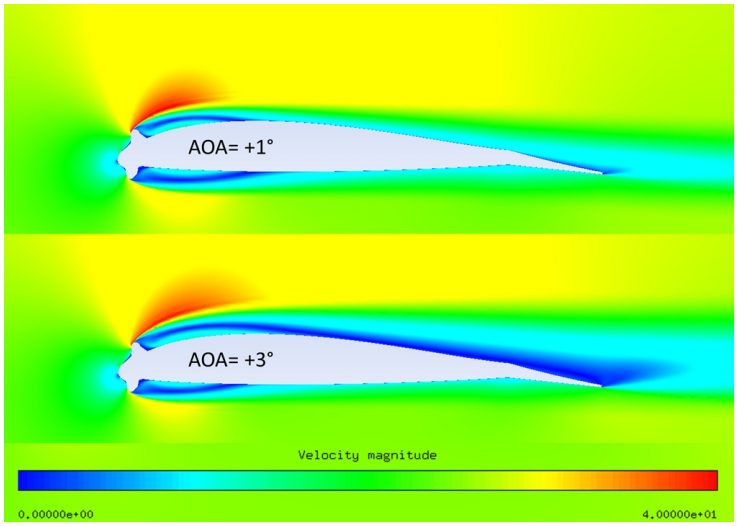

Figure 10 Flow separation on the leading edge.

per angle of deflection compared to the clean airfoil. The effect of ice on the moment behavior is shown in Fig. 9c. The effects here are less consistent compared to drag and lift. Without any flap deflection, the iced airfoil generates slightly less moment, resulting almost in a neutral airfoil. In the cases with flap deflection, the iced airfoils generate more positive moments. In average, the iced airfoils generates −37% less moment compared to the clean case.

In summary, the analysis show show that icing has several critical effects on the airfoil. Ice accretions decrease the effectiveness of the control surface by lowering the additional lift and increasing the additional drag per degree of flap deflection. While icing also leads to a substantial reduction of the stall angles, the CFD analysis is only used to find an estimate of the reduction in control surface effectiveness from the clean case to the fully iced case in this paper. Furthermore, the ice shape is leading to substantial changes in the moment behavior, which can affect the overall aircraft stability.

B. Controller parameters

Acknowledgments

The work is partly sponsored by the Research Council of Norway through the Centre of Excellence funding scheme, project number 223254, AMOS, and projects number 316425, and 296228.

The numerical simulations were performed on resources provided by the National Infrastructure for High Performance Computing and Data Storage in Norway (UNINETT Sigma2) on the Fram supercomputer, under project code NN9613K Notur/NorStore"

Table 1 The adaptive rates of the MRAC scheme.

Roll adaptive rates		**Pitch adaptive rates**	
Parameter	Value	Parameter	Value
$\boldsymbol{Q}$	$\begin{bmatrix} 3 & 0 \\ 0 & 1 \end{bmatrix}$	$\boldsymbol{Q}$	$\begin{bmatrix} 4 & 0 \\ 0 & 0.4 \end{bmatrix}$
$\boldsymbol{\Gamma}_x$	$\begin{bmatrix} 12 & 0 \\ 0 & 4 \end{bmatrix}$	$\boldsymbol{\Gamma}_x$	$\begin{bmatrix} 6 & 0 \\ 0 & 0.01 \end{bmatrix}$
$\boldsymbol{\Gamma}_r$	10	$\boldsymbol{\Gamma}_r$	5
$\boldsymbol{\Gamma}_\Theta$	15	$\boldsymbol{\Gamma}_\Theta$	10

Table 2 The tuning parameters of the roll and pitch PID controllers.

Roll controller gains		**Pitch controller gains**	
Parameter	Value	Parameter	Value
k_{p_ϕ}	2.5	k_{p_θ}	-1
k_{i_ϕ}	2	k_{i_θ}	-0.1
k_{d_ϕ}	0.01	k_{d_θ}	-0.25

References

[1] Bragg, M., Broeren, A., and Blumenthal, L., "Iced-airfoil aerodynamics," *Progress in Aerospace Sciences*, Vol. 41, No. 5, 2005, pp. 323–362. https://doi.org/https://doi.org/10.1016/j.paerosci.2005.07.001.

[2] Lynch, F. T., and Khodadoust, A., "Effects of ice accretions on aircraft aerodynamics," *Progress in Aerospace Sciences*, Vol. 37, No. 8, 2001, pp. 669–767. https://doi.org/10.1016/S0376-0421(01)00018-5.

[3] Hann, R., and Johansen, T. A., "UAV icing: the influence of airspeed and chord length on performance degradation," *Aircraft Engineering and Aerospace Technology*, Vol. 93, 2021. https://doi.org/10.1108/AEAT-06-2020-0127.

[4] Hann, R., Enache, A., Nielsen, M. C., Stovner, B. N., van Beeck, J., Johansen, T. A., and Borup, K. T., "Experimental heat loads for electrothermal anti-icing and de-icing on UAVs," *Aerospace*, Vol. 8, 2021. https://doi.org/10.3390/aerospace8030083.

[5] Hann, R., "Atmospheric Ice Accretions, Aerodynamic Icing Penalties, and Ice Protection Systems on Unmanned Aerial Vehicles." Ph.D. thesis, Norwegian University of Science and Technology, 2020.

[6] Kleiven, R., Gryte, K., and Johansen, T. A., "Robust and Gain-Scheduled Flight Control of Fixed-Wing UAVs in Wind and Icing Conditions," *IEEE Aerospace Conference*, 2021.

[7] Ioannou, P. A., and Sun, J., *Robust adaptive control*, Dover Publications, Inc, Mineola, New York, 2012.

[8] Chowdhary, G., Johnson, E. N., Chandramohan, R., Kimbrell, M. S., and Calise, A., "Guidance and Control of Airplanes Under Actuator Failures and Severe Structural Damage," *Journal of Guidance, Control, and Dynamics*, Vol. 36, No. 4, 2013, pp. 1093–1104. https://doi.org/10.2514/1.58028.

[9] Lavretsky, E., and Wise, K. A., *Robust and adaptive control: with aerospace applications*, Advanced textbooks in control and signal processing, Springer, London ; New York, 2013. OCLC: ocn837660452.

[10] Winter, A., Hann, R., Wenz, A., Gryte, K., and Johansen, T. A., "Stability of a Flying Wing UAV in Icing Conditions," *8th European Conference for Aeronautics and Space Sciences (EUCASS)*, 2019.

[11] Liu, Y., Li, L., Chen, W., Tian, W., and Hu, H., "An experimental study on the aerodynamic performance degradation of a UAS propeller model induced by ice accretion process," *Experimental Thermal and Fluid Science*, Vol. 102, 2019, pp. 101–112. https://doi.org/https://doi.org/10.1016/j.expthermflusci.2018.11.008.

[12] Hann, R., Wenz, A., Gryte, K., and Johansen, T. A., "Impact of atmospheric icing on UAV aerodynamic performance," *2017 Workshop on Research, Education and Development of Unmanned Aerial Systems (RED-UAS)*, IEEE, Linkoping, 2017, pp. 66–71. https://doi.org/10.1109/RED-UAS.2017.8101645.

[13] Beard, R. W., and McLain, T. W., *Small Unmanned Aircraft: Theory and Practice*, Princeton University Press, USA, 2012.

[14] Wenz, A., and Johansen, T. A., "Moving Horizon Estimation of Air Data Parameters for UAVs," *IEEE Transactions on Aerospace and Electronic Systems*, Vol. 56, No. 3, 2020, pp. 2101–2121. https://doi.org/10.1109/TAES.2019.2946677.

Sif Högnadóttir

Inner-Loop Adaptive Control of Fixed-Wing Unmanned Aerial Vehicles in Icing Conditions

NTNU
Norwegian University of
Science and Technology